CEBAF INJECTOR FOR K_L BEAM CONDITIONS

by

Sunil Pokharel
M.S. May 2020, Old Dominion University
M.S. September 2006, Tribhuvan University, Nepal
B.S. May 2004, Tribhuvan University, Nepal

A Dissertation Submitted to the Faculty of
Old Dominion University in Partial Fulfillment of the
Requirements for the Degree of

DOCTOR OF PHILOSOPHY

PHYSICS

OLD DOMINION UNIVERSITY
May 2024

Approved by:

Geoffrey A. Krafft (Director)

Jean R. Delayen (Member)

Todd Satogata (Member)

Moskov Amaryan (Member)

Mohammad Zubair (Member)

ABSTRACT

CEBAF INJECTOR FOR K_L BEAM CONDITIONS

Sunil Pokharel
Old Dominion University, 2024
Director: Dr. Geoffrey A. Krafft

The Continuous Electron Beam Accelerator Facility (CEBAF) at Jefferson Lab concurrently operates four experimental Halls with distinct bunch charge specifications and repetition rates. Numerous critical beam parameters within CEBAF are configured in the injector, some remaining unchanged throughout the accelerator. Consequently, the injector plays a crucial role in determining final beam characteristics, including bunch structure, beam sizes, bunch lengths, energy spread, and beam transmission. The Jefferson Lab K_L experiment is scheduled to take place at CEBAF in Hall D, featuring a much lower bunch repetition rate of 7.80 MHz or 15.59 MHz, below the nominal values of 249.5 MHz or 499 MHz. Although the proposed average current of 5 µA or 10 µA is low compared to the maximum CEBAF current of approximately 180 µA, the corresponding bunch charge is unusually high for CEBAF injector operation. This study focuses on the behavior of low-repetition-rate, high-bunch-charge (0.32 to 0.64 pC) beams in the CEBAF injector. We investigated the evolution and transmission of low-charge beams to space-charge dominated high-charge beams in the front end of the CEBAF injector for two configurations: the pre-existing CEBAF Phase 1 injector upgrade, operated at 130 kV, and the existing CEBAF Phase 2 injector upgrade, operated at 140 kV, 180 kV, and to be operated at 200 kV. The electron beam through the CEBAF injector is characterized with beam dynamics simulations and comparisons with the available measurements performed at 130 kV. Multi-objective genetic optimizations of the CEBAF injector were performed to determine the operating magnetic elements and RF settings for the evolution and transmission of low, moderate, and high charge beams in the CEBAF injector at 180 kV and 200 kV DC gun voltages. Subsequently, simulations at the same voltages were conducted to obtain the beam characteristics at the front end of the CEBAF injector. The laser spot size and laser pulse length at the cathode were varied to observe their effects on beam transmission in the injector at different voltages (130 kV, 180 kV, and 200 kV). Experimental studies at 130 kV, 140 kV, 180 kV validate the simulations. Beam study measurements are carried out using EPICS tools, while optimizations and simulations are facilitated by General Particle Tracer. Based on the findings, optimal parameters for the upcoming Jefferson Lab K_L experiment are proposed, utilizing a lower repetition rate and higher bunch charge.

To my parents, Lila Kumari Pokharel and the late Purnananda Pokharel, and to my beloved wife, Pushpa Pandey, and our children, Sunehra and Sashreek. Also, to my three sisters, Sharada Pokharel, Durga Pokharel, and the late Saraswati Pokharel.

ACKNOWLEDGMENTS

I would like to express my gratitude to all the individuals who have supported and assisted me throughout my PhD journey. First and foremost, I am immensely thankful to my research supervisor, Dr. Geoffrey A. Krafft, for entrusting me with this project and believing in my capabilities. Dr. Krafft, a distinguished physicist and professor, is passionate about both teaching and research. Our numerous discussions in his CEBAF office regarding the project's challenges have been invaluable, and I take pride in being his Ph.D. student.

I also extend my acknowledgment and thanks to Dr. Todd Satogata, a member of my thesis committee, for providing guidance, motivation, and support during my Ph.D. at Jefferson Lab. Dr. Satogata played a crucial role in my accelerator studies for about six months before initiating the Ph.D. thesis project, imparting various computational skills and fundamental accelerator terminology. I appreciate Dr. Moskov Amaryan for suggesting this project and offering valuable suggestions throughout my research. Additionally, I am grateful to Dr. Jean Delayen and Dr. Mohammad Zubair, who served on my thesis committee, for their constructive feedback and suggestions during annual reviews and thesis evaluation meetings.

Special thanks are due to Dr. Alicia Hofler for her insightful ideas and support in the project. Dr. Hofler provided physics concepts, simulation codes, and numerical tools for the research work, as well as contributed to planning and conducting injector beam studies at the Machine Control Center (MCC) at Jefferson Lab. I express gratitude to Dr. Joe Grames for his valuable comments, suggestions, and guidance regarding the injector studies for the K-Long project. I am thankful for Dr. Ryan Bodenstein, Dr. Josh Yoskowitz, Dr. Yves Roblin, Ken Surles-Law, Daniel Moser and Accelerator Operations division at Jefferson Lab, for their immense support on preparation and carrying out of the beam studies.

Furthermore, I extend my appreciation to the individuals at CASA and injector group at Jefferson Lab, where I spent nearly four years working on this project. Specifically, I thank Dr. Reza Kazimi, Dr. Shukui Zhang, and Dr. Max Bruker for their discussions, suggestions, and insights related to the K-Long experiment and the CEBAF injector. I also acknowledge Dr. Mathew Poelker and Dr. Yang Wang for their fruitful discussions on accelerator physics while working at UITF and the CEBAF and carrying out of the beam study.

I am deeply grateful to the Physics Department at Old Dominion University for supporting my graduate studies. Special thanks to individuals in the Physics Department, including the late Ms. Lisa Okun and Ms. Annette Guzman-Smith, for their continuous academic and personal support. I extend my gratitude to friends and classmates at ODU, whose friendship will be cherished in my heart forever. I am also grateful to Tribhuvan University for providing me with the opportunity to pursue my Ph.D. degree at ODU.

Finally, I extend my deepest gratitude to my parents, my wife Pushpa Pandey, my daughter Sunehra Pokharel, and my son Sashreek Pokharel. I also express my appreciation to my mother, Lila Kumari Pokharel, and my mother-in-law, Maya Devi Pandey, for their unwavering support, enabling me to pursue my dreams. Special thanks to my sisters, Sharada, Durga, and the late Saraswati, who provided motivation, financial assistance, and emotional support at every stage, from primary school to graduate school. I am thankful for the support of my brother Anil Pyasi Pokharel, sister Sharmila, brother-in-laws Dhruba Adhikari and the late Sitaram Wagle. Gratitude extends to all the members of my family and extended family, who have been my steadfast supporters. Their continuous encouragement has been invaluable and has played a significant role in my journey.

I would like to acknowledge the support of the U. S. Department of Energy, Office of Science, Office of Nuclear Physics under contract DE-AC05-06OR23177 for this work.

TABLE OF CONTENTS

Page

Chapter

LIST OF TABLES

LIST OF FIGURES

Figure Page

Figure Page

CHAPTER 1

INTRODUCTION

The capability of electron accelerators to efficiently generate unpolarized or polarized electron beams has paved the way for experiments with diverse applications in nuclear and high-energy physics. In Hall D at Jefferson Lab, the experiment involving a beam of long-lived neutral kaons, called K-Long ($\mathrm{K_L}$), will be conducted at the K-Long Facility (KLF) [1, 2]. This experiment will utilize the Continuous Electron Beam Accelerator Facility (CEBAF) in conjunction with the GlueX experimental setup for strange hadron spectroscopy. The exceptional quality of the CEBAF electron beam and average current will yield a flux on the order of 1×10^4 $\mathrm{K_L}$/s, surpassing the previously achieved flux at Stanford Linear Accelerator Center (SLAC) by three orders of magnitude. This advancement will enable a wide range of measurements and enhance the statistical accuracy of earlier data collected on a hydrogen target by a factor of three. Moreover, employing a deuteron target will mark the first-ever measurements with neutral kaons on neutrons.

The experiment described will measure the differential cross sections and self-analyzed polarizations of produced hyperons, including Λ, Σ, Ξ, and Ω, using the GlueX detector in Jefferson Lab Hall D. The measurements will cover a range of center of mass (CM) $\cos\theta$ from -0.95 to 0.95 and a range of the invariant mass of the final-state particles (W) from 1490 MeV to 2500 MeV [1]. The resulting data will allow for the partial wave analyses of strange hyperon resonances with reduced model-dependent uncertainties, as well as the establishment of orbitally excited multiplets in the spectra of Ξ and Ω hyperons. Comparisons with the corresponding multiplets in the spectra of charm and bottom hyperons will also provide insights into heavy flavor symmetry and the accuracy of QCD-based calculations. Furthermore, this experiment will provide a unique environment to study strange meson spectroscopy through $\mathrm{K}\pi$ interactions, allowing for the identification of pole positions in S$-$, P$-$ and D$-$waves. The results of the experiment will also provide additional support for the existence of the low-lying strange scalar meson $\kappa(800)$ and significantly improve the determination of its mass and width.

The $\mathrm{K_L}$ experiment requires time-of-flight measurements. To achieve this, substantially lower bunch repetition rates are needed in the Continuous Electron Beam Accelerator Facility

(CEBAF) than the nominal 249.5 MHz or 499 MHz. While the proposed average current of 2.5 - 5.0 µA is relatively low compared to the maximum CEBAF current of approximately 180 µA, the corresponding bunch charge is higher than typical for CEBAF injector operation. The momenta of K_L particles will be determined through time-of-flight measurements, which entail measurements of the time difference between the RF signal of the CEBAF accelerator and start counters surrounding the LH_2/LD_2 target. A schematic view of the beamline is presented in Fig. 1. At 12 GeV, an average current of 2.5 - 5.0 µA corresponds to 30 - 60 kW of beam power, which will be converted to photons by the compact photon source (CPS) illuminating the beryllium (Be) target.

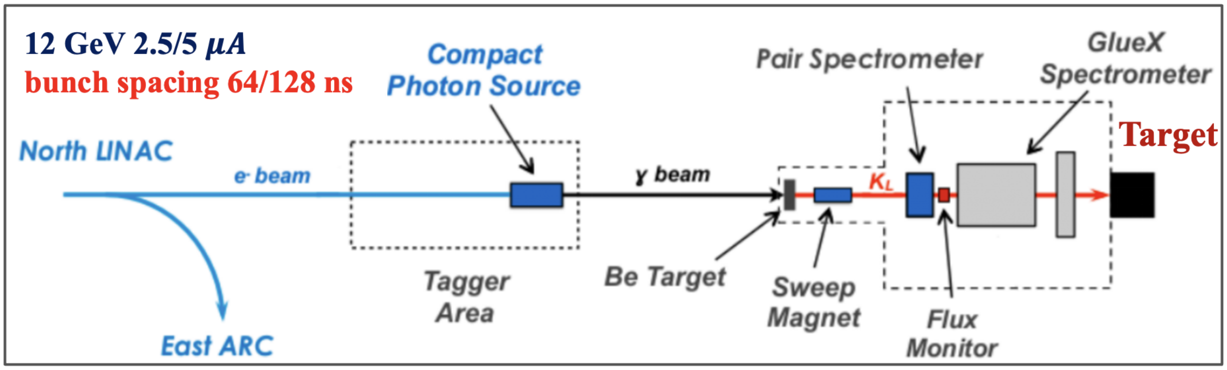

FIG. 1. Schematic view of Jefferson Lab Hall D beamline for $e \rightarrow \gamma \rightarrow K_L$. Electrons first hit the copper radiator inside the compact photon source. Then photons illuminate the Be target where the K_L particles are produced. Finally, neutral kaons hit the LH_2/LD_2 cryogenic target. Beam goes from left to right [1].

1.1 RESEARCH GOALS AND OBJECTIVES

For linear accelerators (linacs), the injector is where the particles to be accelerated originate, and therefore it sets the beam performance characteristics of the machine. This makes the beam parameters at the injector a critical aspect of the final beam characteristics of the machine. In CEBAF, many of the critical beam parameters are set in the injector and some remain unchanged throughout the accelerator. Therefore, the injector plays a significant role in setting the final beam qualities, such as bunch structure, energy spread, current stability, etc. The CEBAF polarized electron source creates a spin-polarized electron beam using a DC high voltage photogun. The electron beam originates within the photogun and then passes through the beamline. The electron beam itself is composed of four interleaved electron beams created with four lasers, allowing four experimental halls to simultaneously receive electron beams [3]. However, designing an injector and delivering the electron beam into the experimental halls for different charge per bunch, from low to high, for CEBAF operation represents a significant challenge.

The initial focus of this research was to generate, characterize, and simulate a bunched electron beam from a DC gun with a high bunch charge and low repetition rate, in accordance with the beam requirements for the K_L experiment to achieve its goal. Table 1 summarizes the individual bunch charges corresponding to these beam requirements for the K_L experiment.

TABLE 1. CEBAF injector bunch currents and repetition rates for the K_L experiment [1].

Current (µA)	Repetition Rate (MHz)	Subharmonic of 499 MHz	Bunch Charge (pC)	Equivalent 499 MHz Current (µA)	Equivalent 249.5 MHz Current (µA)
2.5	15.59	32^{nd}	0.16	80	40
2.5	7.80	64^{th}	0.32	160	80
5.0	15.59	32^{nd}	0.32	160	80
5.0	7.80	64^{th}	0.64	320	160

In order to achieve the goals of generating, characterizing, and simulating a bunched electron beam with high bunch charge and low repetition rate, the research objectives were set as follows:

- Use the optimized variables (magnetic elements and RF settings) of the pre-existing Phase 1 CEBAF injector upgrade at 130 kV DC high-voltage photogun to generate electron beams and investigate the evolution and transmission of low-rep-rate, high bunch charge (0.32 to 0.64 pC) beams through the CEBAF injector.

- Describe the designed beam size, the initial electron beam distribution, and analyze the beam characteristics, and characterize the transmission as a function of the photocathode laser spot size and pulse length for two injector laser drive frequency modes: one with 249.5 MHz and another with 499 MHz.

- Report on the findings of these simulations, predict optimum parameters for operating the experiment, and describe upcoming experimental studies to validate these simulations.

- Simulate the CEBAF injector to investigate the evolution in bunch length of beams through the beamline of the injector with the existing 130 kV electron gun, and perform measurements to validate these simulations.

- Optimize magnetic elements and RF parameters through multi-objective genetic optimization (MGO) for the Phase 2 CEBAF injector upgrade model at both 180 kV and 200 kV gun voltages. These optimized settings are crucial for the effective operation of the CEBAF injector in the K_L experiment.

- Perform simulations on the CEBAF injector model at both 180 kV and 200 kV to monitor the evolution of beam characteristics. This includes tracking transverse beam sizes, bunch length, energy spread, beam transmission, and normalized transverse emittance. The simulation encompasses a range of bunch charges, from low to high, enabling concurrent operations in all four CEBAF experimental Halls.

- Conduct measurements for Phase 2 of the CEBAF injector at a gun voltage of 180 kV for the K_L experiment. This focus is essential as the gun voltage is set at 180 kV for the fall 2023 operation. Measurements should employ the existing laser with frequencies of 249.5/499 MHz and the new Hall D K_L laser at 15.6 MHz.

- Perform measurements at a 140 kV gun voltage across a range of charges using the K_L laser at 15.6 MHz. Compare these measurements with those conducted at 130 kV and 180 kV DC gun voltages.

1.2 ORGANIZATION OF THE DISSERTATION

This dissertation is organized as follows: Chapter 2 introduces the CEBAF accelerator, providing a technical description of its electron source at Jefferson Lab, including the gun high voltage, drive laser, and CEBAF injector beamline elements. Chapter 3 discusses the optics and beam dynamics, covering basic concepts of accelerator physics, accelerator beamline elements, linear beam dynamics, and derivations of some formalism used in this dissertation. Chapter 4 provides a more detailed explanation of the theoretical background of the space charge effect related to this dissertation. Chapter 5 presents the characterization of the electron beam using simulation techniques, detailed measurement procedures, and results analysis. It includes the evolution of transverse beam size, bunch length, normalized transverse emittances, energy spread, and other relevant parameters along the beam line of the CEBAF injector as a function of charge per bunch for both the pre-existing and existing upgraded configurations of the CEBAF injector. Additionally, it reports on the findings related to the measurement that helped validate and benchmark the simulations against the actual measurement results. Finally, Chapter 6 summarizes the results, conclusions, and future work.

CHAPTER 2

CEBAF OVERVIEW

The Continuous Electron Beam Accelerator Facility (CEBAF) is a nuclear physics research facility located in Newport News, Virginia, which was built by the the United States Department of Energy (DOE). The facility comprises two linear accelerators, recirculating arcs, and four experimental halls labeled A, B, C, and D. The facility's tunnel is situated 8 meters underground and has a circumference of 1.4 km, with a 3-meter height and 4-meter width. The design beam energy of CEBAF is 2.2 GeV per pass, and it can accelerate an electron beam to 11 GeV in Halls A, B, and C after five circulation passes, and to 12 GeV in Hall D after 5.5 circulation passes.

The first electron beam was supplied to users in Hall C with a beam energy of 4 GeV and a beam current of 200 µA in 1995. Two years later, Hall A and Hall B were also provided with the beam. By 1998, all three halls were operating simultaneously. The superconducting radio frequency (SRF) gradient and cryogenic systems were updated in 2000 to support 6 GeV energy operation. The 6 GeV operation concluded in 2012 to pave the way for a 12 GeV upgrade. The upgraded CEBAF was commissioned from late 2013 to 2017, with the addition of a new experimental Hall D. On January 12, 2018, the milestone of simultaneous operation of all four halls in the upgraded facility was officially achieved [4, 5].

2.1 BEAM LINE DESCRIPTION

Figure 2 illustrates the main components of the Jefferson Lab CEBAF accelerator and the location of the injector. The current machine can accelerate electrons up to 12 GeV by recirculating the beam 5.5 times through two 1497 MHz SRF linear accelerators. To create the polarized electron beam, the photo cathode is used at 130 kV DC high voltage. The beam achieves full injection energy of 123 MeV after acceleration by the cryomodules before reaching the injector chicane. The SRF cavities in the cryomodules are either five-cell and 50 cm long (in C20, C50, and C75 cryo-modules) or seven-cell and 70 cm long (in the new C100 cryomodules). Liquid helium is used to fill the cryomodules, which operate at a temperature of 2.07 K. Following the injector chicane, the beam is injected into the North linac.

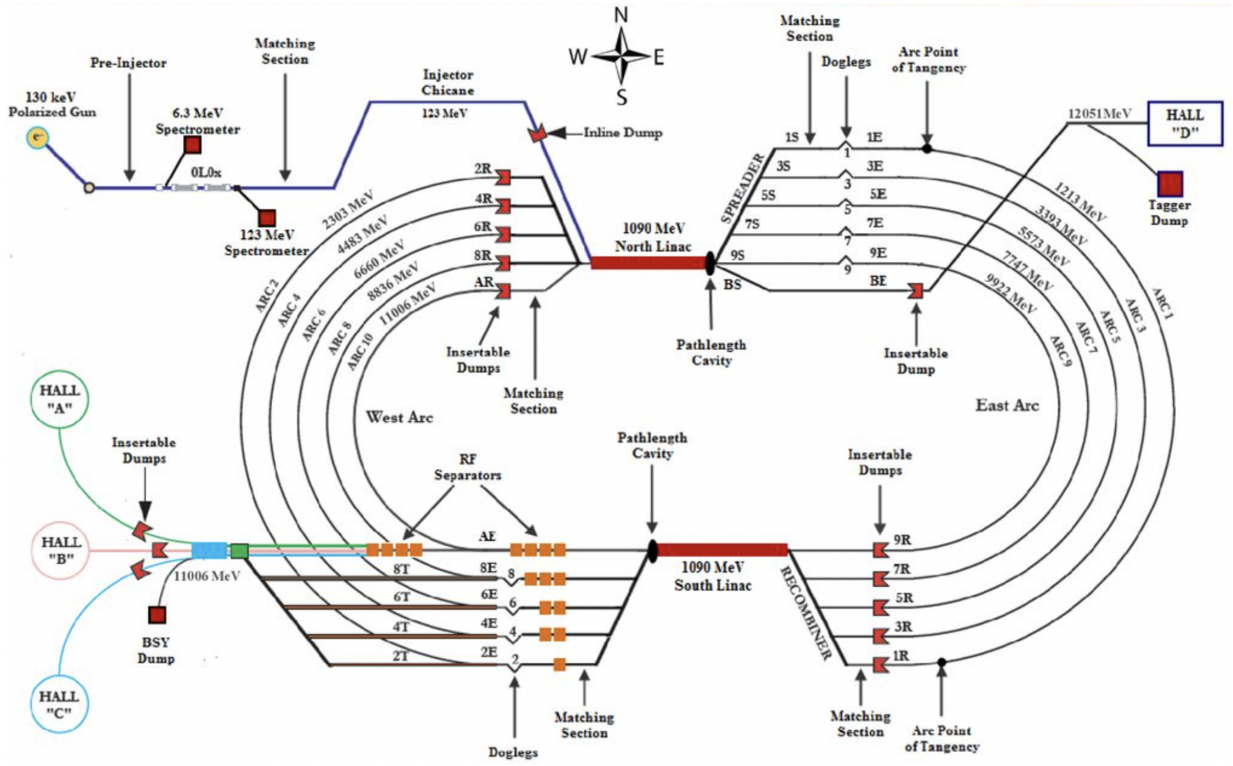

FIG. 2. A schematic layout of the CEBAF accelerator showing the characteristic racetrack design.

The North linac of the CEBAF accelerator is 250 meters long and comprises 25 cryomodules for accelerating the beam. An alternating gradient magnetic lattice is utilized between the cryomodules to ensure that the beam is focused according to the design parameters. As the beam travels through the linac, its energy is raised by 1090 MeV, and it then encounters the East spreader (similar to West spreader used later) (see Fig. 3). The spreader utilizes dipole magnets to vertically separate the beam energies. The lowest energy beam is directed towards the highest elevated arc, Arc1, while the highest energy beam is directed towards the lowest elevated arc, Arc9. The beam passes through the East arcs, namely Arc1, Arc3, Arc5, Arc7, and Arc9, where it is bent by 180°. At the end of the arcs, the beam enters the recombiner (see Fig. 4), which is symmetric with respect to the spreader, and the separated beams are combined back into one as they enter the South linac. Each arc has a different path length, differing by an integer number of RF wavelengths, to maintain synchronicity across different beam passes. Additionally, to minimize bunch length growth in CEBAF, all electrons have the same path length within a single pass, regardless of their energy, implying that the arcs are isochronous. Furthermore, the arc focusing lattice is designed to be achromatic, which means that the position and angle of beam transport at the end of each arc remain unaffected by small changes in beam energy.

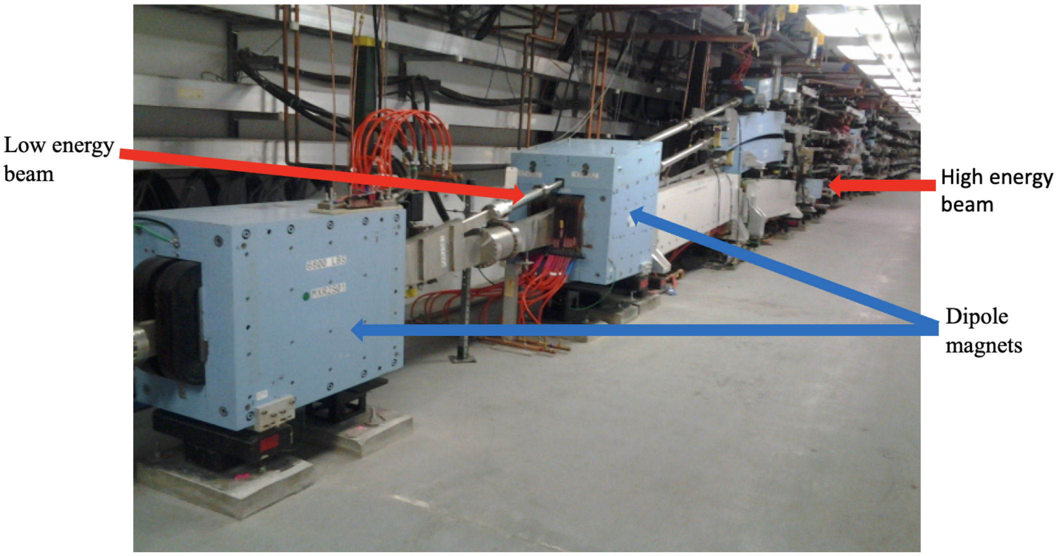

FIG. 3. A photograph of a spreader at the end of South linac.

The South linac has similar acceleration capacity as the North linac, resulting in an increase of 1090 MeV in beam energy. After the South linac, the beam enters the West spreader, which functions similarly to the East spreader. From there, the beam can either be extracted into one of three experimental halls or directed to the West arcs (Arc2, Arc4, Arc6, Arc8, and Arc10), where it is bent 180° and passes through the West recombiner. Once the beam exits the West recombiner, it meets the North linac again; completing a full revolution will increase the beam energy by 2180 MeV. In order to ensure synchronization of successive passes, path length adjustments are made using doglegs in Arcs 1-9. Doglegs are three-magnet chicane systems that match the arrival time of following passes to the crest of the RF wave. The doglegs are located at the beginning of each arc, with five at the beginning of each East arc and four at the beginning of each West arc (except the highest energy arc). During the 12 GeV era, path length adjustments are restricted to 1 cm. This limitation corresponds to 18° of 1497 MHz for the first four doglegs due to power supply limitations. The remaining doglegs exhibit path length changes of less than 1 cm.

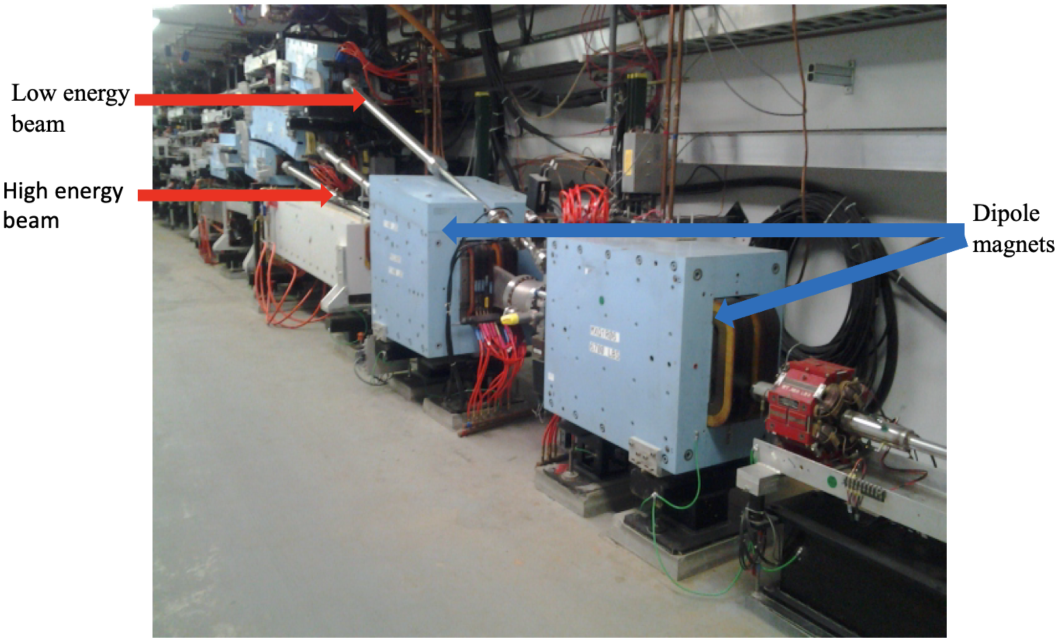

FIG. 4. A photograph of a recombiner at the beginning of South linac.

2.2 CEBAF INJECTOR

The CEBAF injector at Jefferson Lab is responsible for providing beams to the main accelerator and two recirculating linacs. The beams from the injector are delivered to the experimental halls at bunch repetition rates of either 499 MHz or 249.5 MHz.

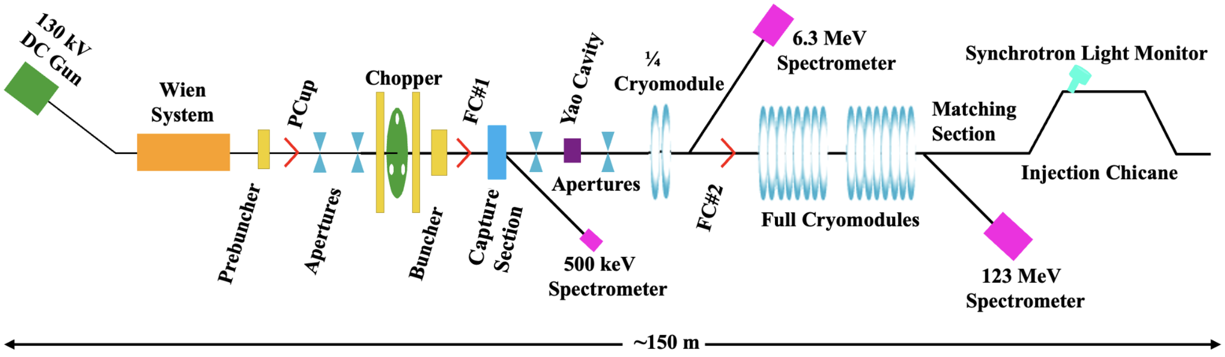

FIG. 5. A layout of the CEBAF injector upgrade Phase 1 section at Jefferson Lab at 130 kV gun voltage. Magnet elements are not shown. PCup, FC#1, and FC#2 are insertable Faraday cups. The longitudinal positions of main beam line elements with respect to the cathode position at z = 0: the prebuncher is located at z = 5.363 m, aperture A1 is at z = 6.48 m, aperture A2 is at z = 7.156 m, the chopper RF cavity is located at z = 7.60 m downstream of the cathode, the buncher is at z = 8.88 m, the Faraday Cup is at z = 9.45 m, the capture is at z = 9.95 m, the quarter cryomodule is at z = 12.80 m, and the upstream of the full cryomodules is approximately at z = 30 m.

Figure 5 illustrates the main components of the CEBAF photoinjector [6–8], which is responsible for generating, transporting, and providing electron beams to the main accelerator. The depicted elements are related to the process of bunching the electrons and controlling their timing. While the magnetic elements: solenoids, dipoles, and quadruples, as well as steering coils, beam position monitors (BPM's), and beam current monitors (BCM's), are not shown in the diagram in Fig. 5, they also play a crucial role in the operation of the CEBAF photoinjector. This photoinjector supports the operation of multiple experimental halls simultaneously [3, 9, 10], supplying continuous-wave (CW) electron pulse trains with varying bunch charge to the main accelerator. The resulting beam has bunch lengths of around 1 ps, 10^{-3} energy spread, and a normalized transverse emittance of <1 mm mrad. The photoinjector's main elements consist of a load-locked DC high-voltage photogun [11–13], a 4π spin-manipulator system (also called the 2-Wien spin flipper) [14], numerous specialized bunching and accelerating RF cavities [6, 7, 9], and the magnetic beam optics used to transport the beam from the photoinjector to the main CEBAF accelerator.

Overall, the CEBAF photoinjector is a complex and sophisticated system that is critical to the successful operation of the CEBAF facility. In Section 2.3 of this thesis, the photoinjector systems are described in beamline order, providing a detailed overview of the various components and how they work together to produce the high-quality electron beams that are essential for a variety of experiments.

2.3 CEBAF INJECTOR BEAMLINE

2.3.1 PHOTOGUN

The CEBAF injector employs a high-voltage photocathode DC gun as its initial component, producing a polarized electron beam with a polarization exceeding 85% and variable charges. The photoemission process begins with a single strained-superlattice GaAs/GaAsP photocathode [15], utilizing four circularly polarized lasers [16], one for each experimental hall. This configuration generates interleaved longitudinally polarized electron pulse trains. The laser beam travels through a vacuum window that is selected to have minimal birefringence. The laser beam then shines directly onto the photocathode at a perpendicular angle. The lasers need to operate at subharmonics of CEBAF's fundamental frequency of 1497 MHz, either at 499 MHz or 249.5 MHz for routine operation. They are configured independently and chosen based on the beam current and delivered bunch charge required for each experiment. During multi-hall operations, the beam current delivered to the four experiment halls can vary significantly, ranging from 100 pA to 100 µA. Moreover, the delivered bunch charge, depending on the requested bunch repetition rate, can range from 0.668×10^{-19} to 0.668×10^{-12} C. The electron bunches leaving the photocathode have a temporal profile similar to the laser pulses used to create them, with a full-width at half-maximum (FWHM) of approximately 45 ps. The DC field in the photogun within the pre-existing injector accelerates the photoelectrons to 130 keV.

Figure 6 illustrates a diagram and photo of the DC high-voltage photogun vacuum chamber, along with its primary components. The cathode is a tee-shaped electrode made of 316LN stainless steel, located at the center of the photogun. It is biased by a high-voltage cable connected to a power supply, and an inverted ceramic insulator insulates the HV cable from the gun chamber vacuum. The region where the cathode and insulator meet, known as the "triple-point," has been demonstrated to generate high-voltage breakdown when the cathode is energized due to its high electric field [18, 19]. To mitigate the electric field at

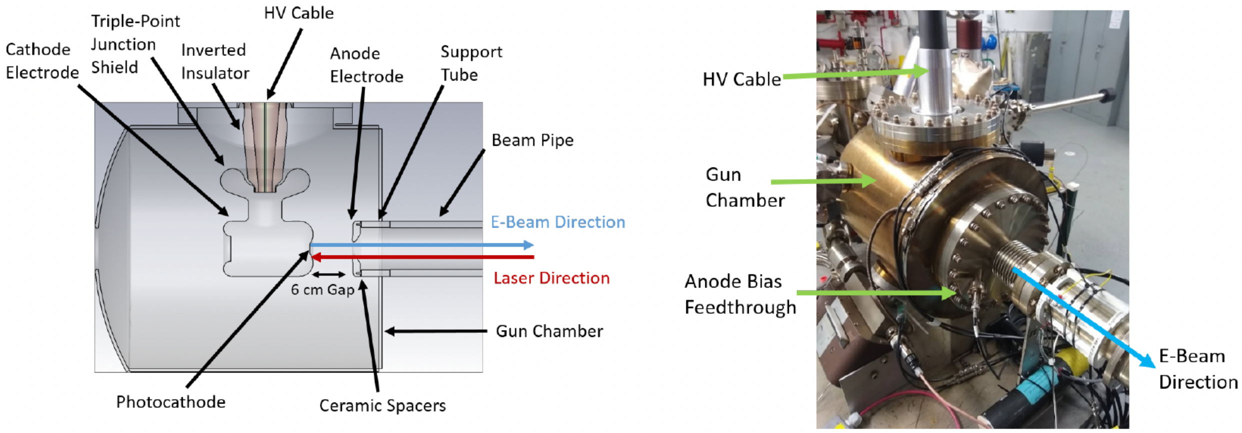

FIG. 6. A schematic of layout and photo of the CEBAF photogun. The CEBAF DC high-voltage photogun with inverted insulator geometry, with essentail components labeled (left) and photograph of the CEBAF DC high-voltage load-locked photogun (right) [17].

this point, the cathode's design has been altered to include an electrostatic shield around the triple-point [20]. Additionally, the Pierce geometry of the cathode's front edge concentrates electrons exiting the photocathode through the anode aperture [21].

2.3.2 STEERING COILS

To ensure that the beam stays along the central axis of the beamline, horizontal and vertical Haimson steering coil pairs are situated at different points along the beamline. As the beam gets a downward kick from the electrostatic shield above the cathode electrode at the start, two steering coil pairs just after the anode work to return the beam to its correct position along the beamline. Additional steering coils further down the beamline correct any irregularities in the beam's path and account for the earth's magnetic field. Figure 7 displays a steering coil pair in a photograph.

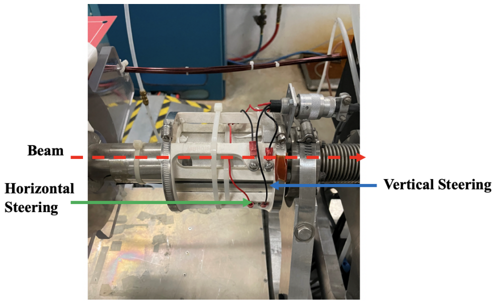

FIG. 7. Photo of a Haimson steering coil pair on the CEBAF beamline.

2.3.3 DIPOLE MAGNET

Once the electron pulse trains pass the third steering coil along the beamline of the CEBAF injector, they are deflected by 15° onto the longitudinal axis of the accelerator with the aid of an air-core dipole magnet. The purpose of the dipole magnet is to enable the lasers to illuminate the photocathode at normal incidence. A photograph of the dipole magnet is presented in Fig. 8.

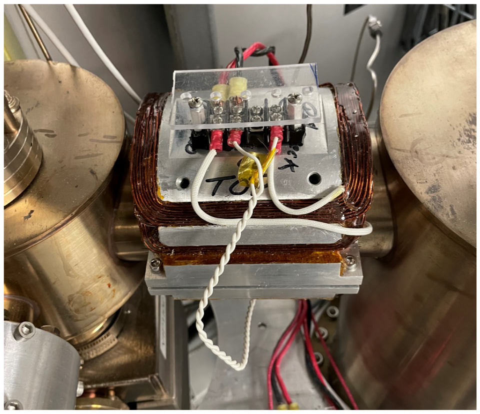

FIG. 8. Photograph of the dipole magnet (15° bend) on the injector beamline.

2.3.4 WEIN SYSTEM

The subsequent segment of the CEBAF Injector beamline is the 4π spin-manipulator system, consisting of two Stanford/Mainz-type Wien filters [22] separated by two single-wound solenoids. The "2-Wien Spin Flipper," as it is known, is illustrated in Fig. 9. The 2-Wien spin flipper is a system that consists of a vertical Wien filter, spin rotating solenoids, and a horizontal Wien filter. The beam travels from left to right, with the large arrows indicating the direction of the beam's polarization. To create "spin flip" polarized beams, where the spin direction is oriented in the horizontal plane but pointing in opposite directions, the polarities of the two solenoid currents (top of the Fig. 9) or the Wien filter dipole current and electrode high voltage polarities (bottom of the Fig. 9) are reversed. In either case, the horizontal Wien filter is utilized to align the spin direction longitudinally at the experiment hall [23].

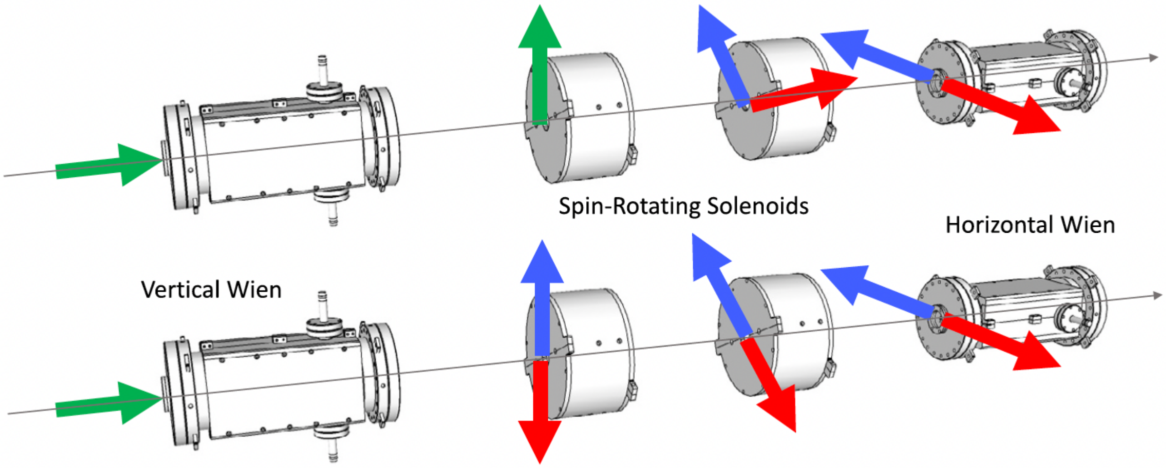

FIG. 9. Illustration depicting the setup of the CEBAF 2-Wien spin flipper. Beam travels left to right, with large arrows depicting beam polarization direction [23].

2.3.5 RF SYSTEM

The RF system is the next section of the CEBAF injector, consisting of both superconducting radio frequency (SRF) and warm RF cavities. In the initial 130 kV experiments, this system includes two RF bunching cavities-prebuncher and buncher, a chopper system, a capture section, two 5-cell superconducting cavities called quarter cryomodule (QCM) and the first two full cryomodules. The accelerating RF system consists of warm capture cavity, quarter cryomodule and the first two full cryomodules. In more recent experiments after the Phase 2 upgrade, the capture section and quarter cryomodule have been replaced with a new booster module containing a 2-cell and 7-cell cavity string. Details about the upgraded injector RF system are described in Section 2.4.

The main purpose of using radio frequency cavities in accelerators is to add energy to (accelerate) charged particle beams with high electric field. The acceleration is achieved via interaction of the particle beam with time-varying longitudinal electric field in an accelerating structure. The highest achievable accelerating gradient (measured in MV/m), however, is not always optimal for an accelerator. There are other factors (both machine-dependent and technology-dependent) that determine operating gradient of RF cavities and influence the cavity design, such as accelerator cost optimization, limitations imposed by existing technology on some components (e.g., maximum power through a fundamental RF input coupler), necessity to extract higher order mode power, etc. Moreover, although the cavity is the heart, the central part of an accelerating module and RF system, it is only one of many parts and its design cannot be easily decoupled from the design of the whole system. In many cases requirements are competing.

The chopper system, described Refs. [9] and [24] and illustrated in Fig. 11, plays a crucial role in controlling the temporal acceptance of the front-end of the CEBAF accelerator. It is composed of three main components: a two-cavity RF-deflector system, two counter-wound solenoids, and three chopping apertures that can be adjusted independently. The RF-deflector system consists of two 499 MHz TM_{210} mode rectangular copper cavities, each driven in two orthogonal transverse deflecting modes, which are phased to sweep the beam in a circular pattern at 499 MHz. The beam at the center of the first cavity is then imaged to the center of the second cavity by a pair of counter-wound solenoid lenses, which bracket the chopping apertures, located midway between the two deflecting cavities. The amplitudes and phases of the fields in the second deflecting cavity are carefully adjusted to cancel out the RF kick from the first cavity. A fully open chopping aperture has a maximum duration of 111 ps, and it regulates very low current beam for experiments that require nA beam

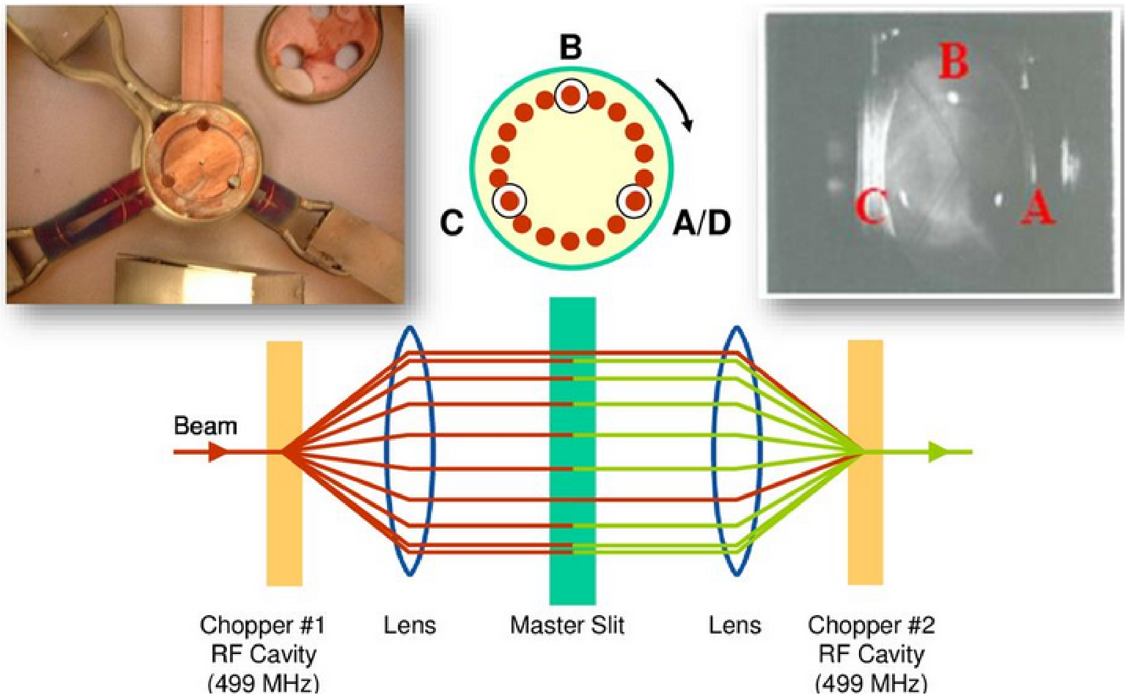

FIG. 10. Diagram of the CEBAF chopper system. A photograph of the three chopping apertures (top left), the chopping system (middle) and a photograph of the electron beams entering the three experimental halls simultaneously (top right) [24].

currents and manages the bleedthrough beam sourced from the higher current beams used for the other experiment halls. Overall, the chopper system not only provides control of the electron bunch downstream but also regulates and manages different types of beams for various experimental needs.

The electron beam current is measured by an insertable Faraday cup after it passes through the chopping system. The Faraday cup consists of an isolated electrode in a circuit with an ammeter that measures the current induced by the electrons when they hit the electrode. Using the Faraday cup in conjunction with the chopping system allows for the measurement of the longitudinal size of an electron bunch. By adjusting the phase of the chopper cavities, the deflection axis of the bunch can be scanned across one of the apertures of the master slit, and the current passing through the slit can be measured by the Faraday cup. Figure 11 depicts a photo of the chopper system and the Faraday cup in the beamline

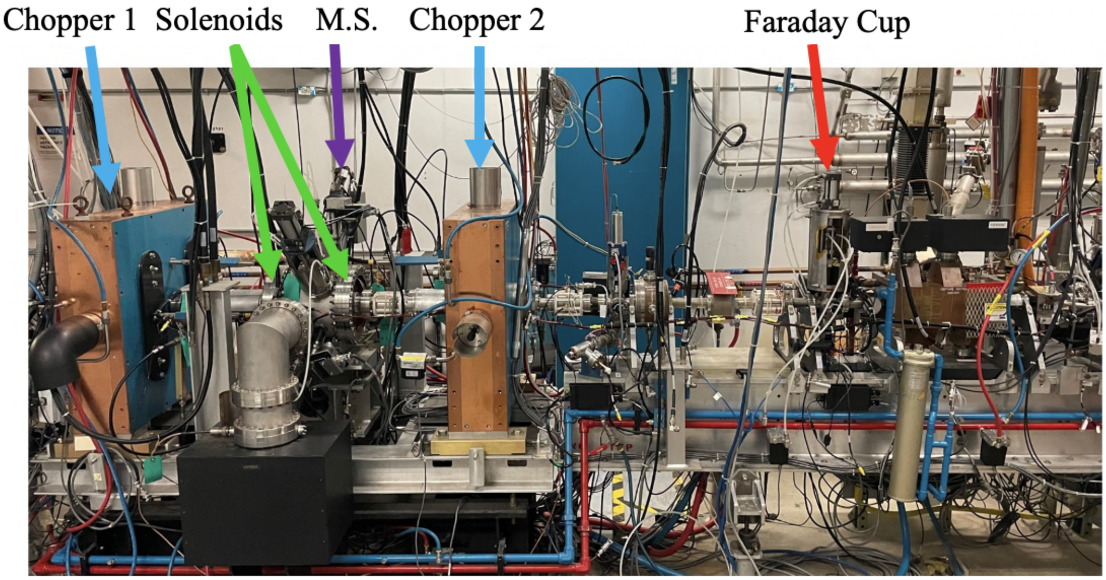

FIG. 11. Photo of the RF chopper system and the Faraday cup.

of the CEBAF injector.

The CEBAF photoinjector uses two RF-bunching cavities, which are re-entrant-style TM_{010} pillbox copper cavities operating at 1497 MHz. These cavities are used to maintain the desired longitudinal bunch length of the non-relativistic beam. The first cavity, called the prebuncher [7, 25], is located between the photocathode and the chopper and is set to zero-crossing. The objective is to counteract the elongation or growth of the bunch length that occurs due to the presence of space-charge forces along the distance between the gun and the chopper system in the injector. Even for bunches with low charges, space-charge forces cause an increase in both the spatial and temporal size of the bunch [26]. If not compensated, the space-charge forces acting on bunches with the highest charges can cause the bunch length to grow beyond 111 picoseconds, resulting in avoidable loss of the beam. The second buncher cavity [27], which is positioned between the center of the chopper system and the following RF cavity referred to as the "capture section", serves as the phase reference for the injector and CEBAF accelerator [28]. Usually, it is set to zero-crossing or within 20° of zero-crossing to initiate the compression of the longitudinal bunch.

The capture section [6, 25, 29] is a type of side-coupled cavity comprising five cells designed with a graded-beta configuration. Its primary function is to boost the 130 keV beam to around 630 keV and enhance bunching. The name “capture section” arises from the fact that it raises the beam’s kinetic energy by approximately 500 keV, which renders it suitably relativistic and matched in beta with the two superconducting cavities that follow downstream.

The quarter cryomodule [6, 25, 30] houses two 5-cell superconducting cavities and is part of the original cryomodules for CEBAF, which have eight 5-cell Cornell style accelerating cavities constructed in four subsections, each containing a pair of cavities. The quarter cryomodule is named after representing one of these cryomodules subsections [31] and is responsible for accelerating the beam to 6.2 MeV. The cavities in the quarter cryomodule are phased off-crest to continue the bunching process initiated in the second buncher cavity, with further drift bunching occurring in the downstream beam transport line. The beams delivered downstream of the quarter cryomodule are further accelerated to 123 MeV using two full cryomodules.

2.3.6 SOLENOID

Solenoid magnets are commonly employed to focus low energy beams in an injector. The elements used to transport the beam from the gun to the quarter cryomodule include solenoids placed at various points along the beam path. These solenoids serve to focus the beam transversely at adjacent downstream components, such as the dipole magnet, Wien filters, and RF cavities.

There are two main types of solenoids used in the beam transport system: single-wound and counter-wound. Between the gun and spin-manipulator system, two single-wound solenoids are used. Between the spin-manipulator system and the quarter cryomodule, three counter-wound solenoids are used, in addition to the two counter-wound solenoids in the chopper system. Counter-wound solenoids are preferred after the spin-manipulator system as they do not alter the polarization and spin configuration, unlike single-wound solenoids. The photo in Fig. 12 displays the first solenoid located after the photogun. The field strength of this solenoid is adjusted to ensure that the beam size is minimized at the center of the dipole magnet.

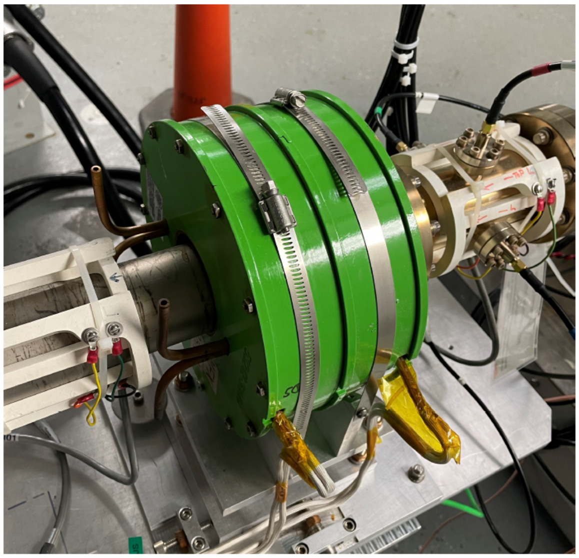

FIG. 12. Photo of a solenoid on the CEBAF injector beamline.

2.3.7 BEAM POSITION MONITOR

Antenna beam-position monitors (BPM's) are utilized in the beamline to monitor and ensure the alignment of the four independent beams by measuring the beam position. These monitors also enable realignment of the beam to an approved orbit whenever adjustments are made to the photocathode lasers or Wien filter spin angles. The antenna-style BPM at the CEBAF photoinjector, depicted in Fig. 13, comprises two pairs of antennae that run parallel to the beamline axis. By measuring the voltage signal induced by the beam, the BPM can determine the transverse position of the beam in either the horizontal (x) or vertical (y) directions.

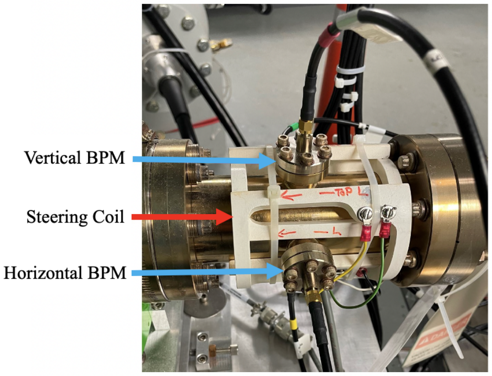

FIG. 13. Photograph of a BPM on the location of a steering coil pair at CEBAF injector beamline.

2.3.8 APERTURES

Four apertures (A_1, A_2, A_3, and A_4) have been positioned along the beamline of the injector to manage the transverse emittance. These apertures have varying hole sizes ranging from 4.0 to 6.5 mm and are utilized to collimate the beam and decrease the extent of transverse phase space. They are named emittance limiting apertures and aid in controlling the beam's launch into and out of the chopper system.

2.3.9 VIEWER

Viewers are utilized to observe the transverse current distribution of the beam, and they consist of an insertable screen made of yttrium aluminum garnet (YAG) that fluoresces when excited by the beam. The screen is positioned at a 45° angle relative to the beam, allowing a charge-coupled device (CCD) camera to capture the fluorescent light passing through a view port. Below saturation the intensity distribution of the light is directly proportional to the transverse current distribution of the beam. To determine the transverse transverse (horizontal and vertical) root mean square (*rms*) beam sizes (σ_x and σ_y), measurements of the distribution projections in the x-and y-directions are taken. Figure 14 displays a photograph of the first viewer positioned after the photogun.

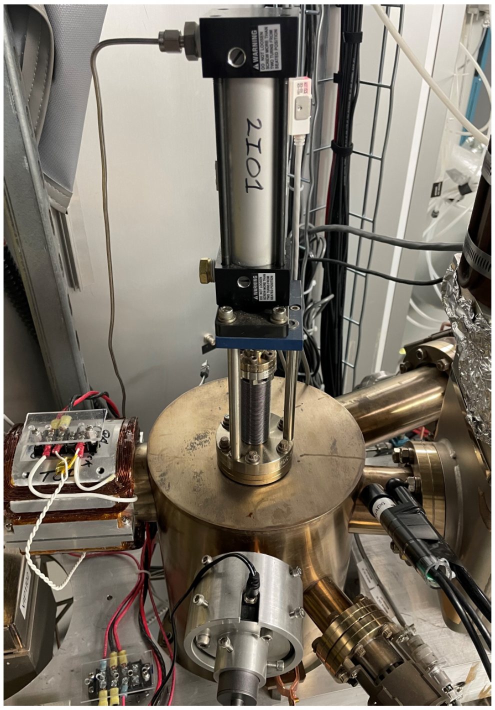

FIG. 14. Photograph of a viewer on the injector beamline.

2.3.10 DRIVE LASERS

The CEBAF injector has four identical photogun drive lasers, which produce RF-pulsed light with an optical pulse width of around 45 ps (FWHM) and are used to create a beam in each of the four experiment halls. The laser beams are combined with interleaved pulse trains, which have a repetition rate of either 249.5 MHz or 499 MHz. For the K_L experiment, the repetition rate will be either 7.8 MHz or 15.6 MHz. They all illuminate the same location on the photocathode. The physical layout of this setup is shown in Fig. 15. The lasers produce 780 nm light that shines onto the photocathode. During CEBAF operations, the intensities of the four lasers are adjusted to create large dynamic ranges in beam currents for each experimental hall [32]. The light from the four lasers is combined using beam splitters and a prism cube, and the combined beam passes through a lens controlled by a stepper motor. The motor can adjust the laser beam's horizontal or vertical deflection, which shifts the laser's position on the photocathode. A power meter inserted after the lens measures

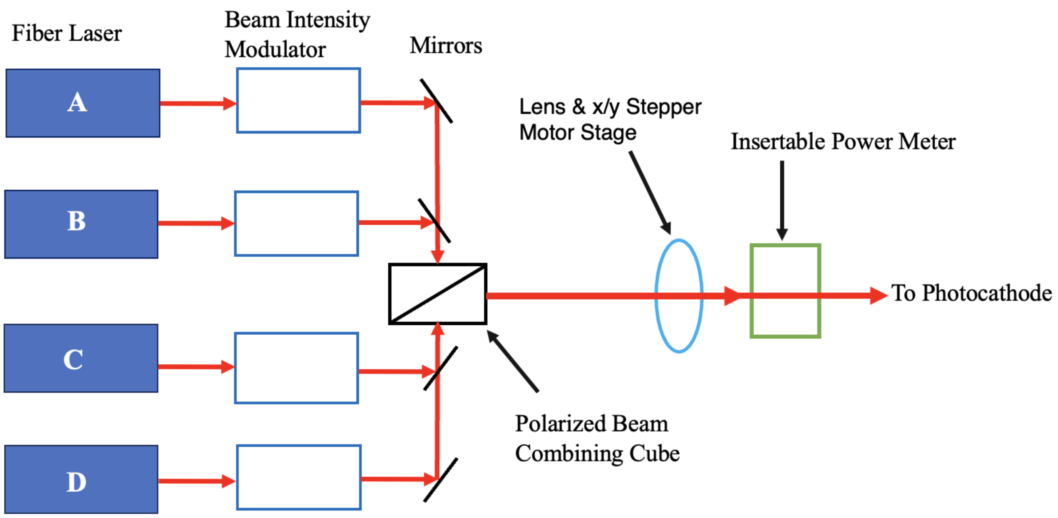

FIG. 15. Schematic of the physical layout of the four fiber lasers [17].

the laser's power before it reaches the photocathode.

2.4 CEBAF INJECTOR UPGRADE

The pre-existing Phase 1 CEBAF injector upgrade utilized a photogun biased at 130 kV with DC high-voltage. The beam is then accelerated using a normal conducting copper-cavity capture section to approximately 630 keV. To achieve the design energy of approximately 5 MeV, a quarter cryomodule consisting of two 1497 MHz SRF five-cell cavities, similar to those used in full cryomodules, was employed. Despite being highly dependable, the beam that passes through the quarter cryomodule experiences a significant transverse deflection due to the existence of asymmetrical fields on the beamline axis caused by the design and implementation of the RF fundamental power couplers and stub tuners [33, 34]. Furthermore, there is strong coupling of xy motion, making it challenging to set the optics on both sides of the quarter cryomodule to achieve a matched beta function, which ultimately limits the adiabatic damping achievable for beam that is delivered to the experiment halls.

In order to resolve the aforementioned problems, a new cryomodule was developed to replace the quarter cryomodule. The newly constructed "booster" cryomodule [35, 36] consists of a 2-cell superconducting capture section, and a 7-cell superconducting cavity which is responsible for most of the beam acceleration. The booster cryomodule, designed to replace the quarter cryomodule, tackles the issues of transverse beam deflection and xy coupling by implementing modern forward power couplers and stub tuners [37–40] to reduce induced electric fields within the cavities. Moreover, it features a modern higher order mode damper [41] that provides inherent up/down symmetry, reducing the skew quadrupole contribution to the field almost to zero, which further reduces the xy coupling. As part of the booster installation, the CEBAF photoinjector underwent simplification by removing the room temperature capture section. This resulted in fewer RF components and a more straightforward injector setup. The removal of the cavity also created additional space for beamline diagnostics, including BPMs. Optics matching tools were utilized to adjust the focusing strength of elements on both sides of the booster, leading to improved lattice matching and enhanced adiabatic damping. Additionally, the beam will be less prone to loss at the injector apertures due to the higher beam energy from the 200 kV bias on the photogun.

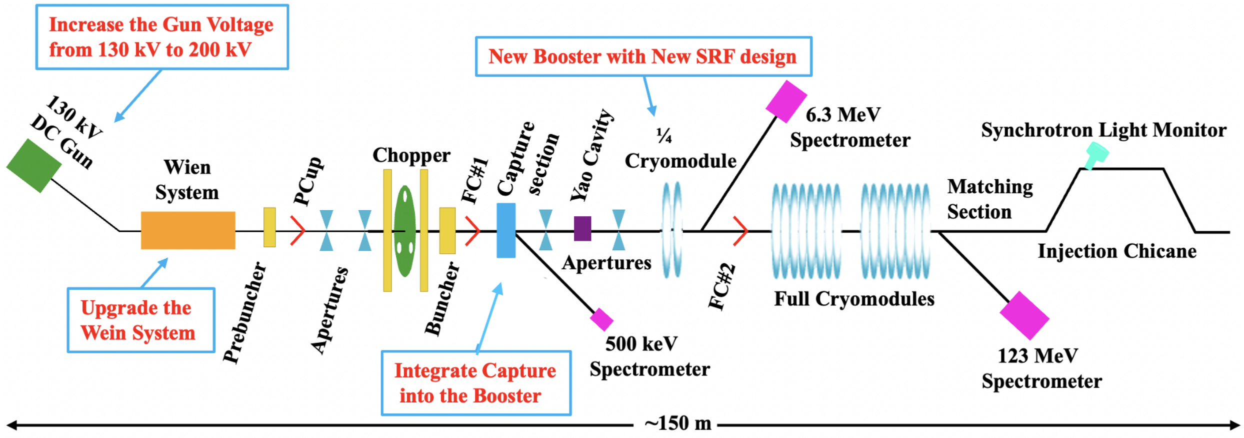

FIG. 16. A layout of the CEBAF injector showing different areas for upgrade (not drawn to scale) from 130 kV to 200 kV gun.

Figure 16 illustrates the different areas of the Phase 2 CEBAF injector upgrade, which was completed during the Scheduled Accelerator Down (SAD) in 2023. Increasing the gun voltage would require adjustments to the operating points of other components in the area. While correctors and solenoids have enough range, the spin manipulators (Wien filters) hardware needed to be upgraded. The choppers, prebuncher, and buncher RF cavities in the 200 keV beam path have enough power to handle the 200 keV beam. The Cornell-type beta-graded five-cell cavity was not matched to a 200 keV input beam. Therefore, the capture section was integrated into the SRF booster, with new 2-7 cell SRF cavities replacing the old 5-5 cell SRF cavities. The CEBAF injector upgrade consists of Phase 1 and Phase 2, as depicted in Fig. 17(a) and Fig. 17(b), respectively. Ultimately, the K_L experiment will be conducted using a 200 kV DC gun.

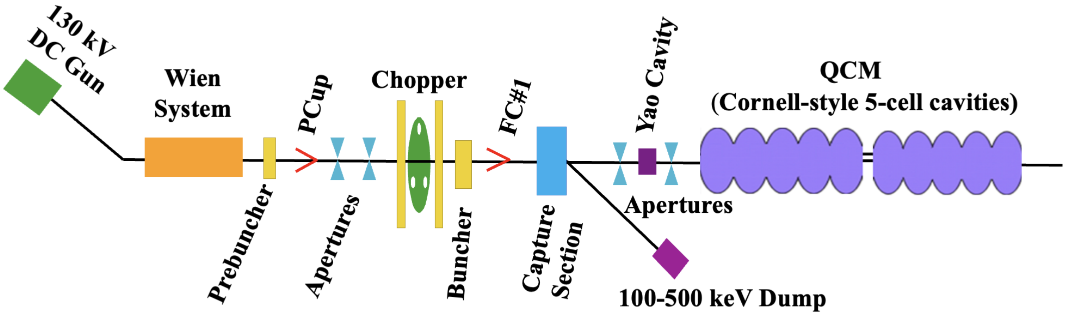

(a) The CEBAF injector upgrade Phase 1.

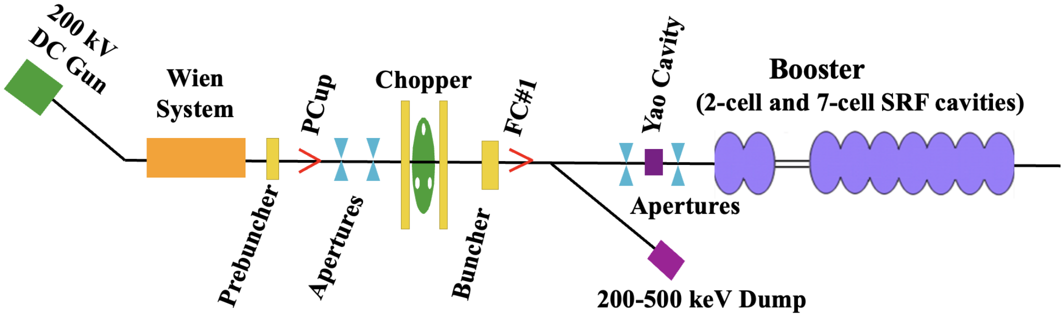

(b) The CEBAF injector upgrade Phase 2.

FIG. 17. CEBAF injector upgrades: (a) Phase 1 and (b) Phase 2. In Phase 2, the capture section is eliminated, the position of the buncher is modified, and the QCM is replaced with 2-cell and 7-cell SRF cavities [42].

CHAPTER 3

OPTICS AND BEAM DYNAMICS

A particle accelerator is a machine that accelerates charged particles like electrons, positrons, or protons. A beam is a collection of particles that have a nonzero average momentum. In modern accelerators, the beam energy is raised using electric fields, mostly radio-frequency (RF) fields. The particle source, also known as a gun, is the starting point of the accelerator, followed by an accelerating section that increases the energy to the desired level. The study of the physical principles that govern the transport and focusing of a particle beam within an accelerator is called “beam optics”. To design the beam optics, the accelerator lattice is essential, consisting of a sequence of elements that the beam passes through, such as solenoids, dipole magnets, quadrupole magnets, sextupole magnets, accelerating cavities, and undulators. Straight sections without electromagnetic fields, called drifts, are also part of the lattice. By utilizing the lattice, a theoretical model of the accelerator is created, which enables the simulation of the machine on a computer.

This chapter aims to introduce the fundamental mathematical framework utilized in accelerator physics. Additionally, we will explore several essential concepts in beam physics that are extensively utilized in this dissertation. The concepts of phase space, beam matrix, and beam emittance will also be introduced and discussed.

3.1 COORDINATE SYSTEMS AND PHASE SPACE COORDINATES

In a particle accelerator, the primary focus is on the movement of a particle *bunch*, consisting of numerous charged particles moving at relativistic speeds through the machine. Due to the complexity of writing the equation of motion for an individual particle in a fixed Cartesian coordinate system, particle coordinates are defined with respect to a *reference orbit*: a path along the accelerator. The reference orbit is typically based on the path an ideal particle would take, such as an arc of a circle in a dipole magnet or a straight line in a drift or quadrupole magnet. However, it can also be defined as a path that no particle would genuinely take, such as a straight line through an undulator.

The motion of particles in a linear accelerator system is typically described by a Cartesian coordinate system (x, y, z), which is established based on the location of the reference particle with momentum p_0 as illustrated in Fig. 18. The curved path in the figure represents the reference trajectory. However, most particles deviate slightly from this trajectory due to differences in position, momentum, and/or time. Consequently, these particles follow paths that are slightly different from the reference trajectory.

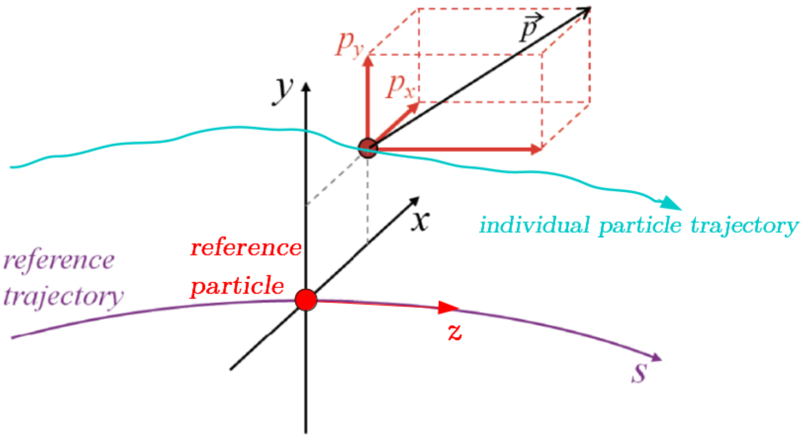

FIG. 18. Reference trajectory and coordinate system.

The deviation of particles from the reference trajectory is described by a set of particle coordinates ($x(s)$, $y(s)$, $z(s)$) that are defined with respect to the ideal particle. These particle coordinates also include relativistic momentum coordinates ($p_x(s)$, $p_y(s)$, $p_z(s)$). The motion of the particle perpendicular to the reference trajectory is described by the transverse coordinates, horizontal ($x(s)$, $p_x(s)$), and vertical ($y(s)$, $p_y(s)$), while motion along the reference trajectory is described by the longitudinal coordinates ($z(s)$, $p_z(s)$). The independent variable s represents the path length along the reference trajectory.

The conventional phase space coordinates are often replaced by geometric coordinates, also known as tracespace, in accelerator physics. These coordinates describe particle motion and are denoted by a vector:

$$\mathbf{X} = \begin{pmatrix} x \\ x' \\ y \\ y' \\ z \\ \delta \end{pmatrix}. \tag{1}$$

Here, $x' = p_x/p_0$, $y' = p_y/p_0$, and $\delta = \Delta p/p_0$, where Δp represents the individual particle momentum difference from p_0.

3.2 EQUATION OF MOTION

The fundamental process of particle acceleration involves the use of electromagnetic fields interacting with the charged particles in a beam. The trajectory of the beam through the accelerator is determined by the dynamics of this interaction, and various components are engineered to accelerate the particles to the desired energy level, steer them along a specific path, and focus them to minimize losses. Consider a point particle with charge q and mass m, whose position is defined by curvilinear coordinates $x(s)$, $y(s)$, and $z(s)$. The magnitude of the velocity of this particle can be expressed as

$$\begin{aligned} \|\mathbf{v}\| &= \sqrt{v_x^2 + v_y^2 + v_z^2} \\ &\equiv \beta c. \end{aligned} \tag{2}$$

Here, c is speed of light in vacuum and β is the Lorentz factor. The relativistic momentum vector of the particle can be expressed as the product of its relativistic mass and velocity vector, which is given by:

$$\begin{aligned} \mathbf{p} &= \gamma m \mathbf{v} \\ &= p_x \hat{x} + p_y \hat{y} + p_z \hat{z}, \end{aligned} \tag{3}$$

with magnitude

$$p = \sqrt{p_x^2 + p_y^2 + p_z^2}. \tag{4}$$

The corresponding mechanical energy of the particle is

$$\begin{aligned} \mathcal{E} &= \sqrt{(pc)^2 + m^2 c^4} \\ &= \gamma m c^2, \end{aligned} \tag{5}$$

where the relativistic factor is

$$\gamma = (1-\beta^2)^{-1/2}. \tag{6}$$

The classical motion of such a particle in an external electric field $\mathbf{E}$ and magnetic field $\mathbf{B}$, without considering radiation losses, is described by the energy gain equation:

$$\frac{d\mathcal{E}}{dt} = q\mathbf{v}\cdot\mathbf{E}, \tag{7a}$$

and the Lorentz force equation:

$$\mathbf{F} = \frac{d\mathbf{p}}{dt} = q\left(\mathbf{E} + \mathbf{v}\times\mathbf{B}\right). \tag{7b}$$

The external electromagnetic fields ($\mathbf{E}$, $\mathbf{B}$) are generated by vector potential $\mathbf{A}$ as $\mathbf{B} = \nabla\times\mathbf{A}$ and scalar potential Φ as $\mathbf{E} = -\nabla\Phi - \partial\mathbf{A}/\partial t$. Since $\mathbf{p} = \gamma m\mathbf{v}$, the Eq. (7b) can be described in general form by the following equation of motion [43–45]:

$$\gamma m\frac{d\mathbf{v}}{dt} + m\mathbf{v}\frac{d\gamma}{dt} = \frac{d\mathbf{p}}{dt} = q\left(-\nabla\Phi - \frac{\partial\mathbf{A}}{\partial t} + \mathbf{v}\times\nabla\times\mathbf{A}\right). \tag{8}$$

Additionally, the external electromagnetic fields ($\mathbf{E}$, $\mathbf{B}$) obey Maxwell's equations in a free space:

$$\nabla\times\mathbf{E} = -\frac{\partial\mathbf{B}}{\partial t}, \quad \nabla\cdot\mathbf{B} = 0. \tag{9}$$

When particles pass through an external electromagnetic field, they can gain energy from static or time-varying electric fields, and static magnetic fields can cause the particle beam to bend and be confined in a transverse direction. Magnetic components, like dipoles and quadrupoles, can bend and focus or defocus the beam while transporting it, forming the basis for the linear approximation. Sextupole and octupole magnets are used beyond the linear approximation to correct non-linear optical aberrations. Linear beam dynamics focuses on linear fields that are either independent of or linearly dependent on a particle's distance from its ideal trajectory. The mathematical description of particle trajectories in the presence of such linear fields is called linear beam dynamics.

3.3 BEAM PHASE SPACE AND TRANSFER MATRIX

The motion of each particle within a bunch can be fully described by its coordinates and momenta in six-dimensional (6D) phase space (x, p_x, y, p_y, z, p_z). The 6D trace space is typically defined as (x, x', y, y', z, δ). If we assume no coupling between dimensions, we can separate the particle motion into transverse (horizontal and vertical) and longitudinal dimensions. The longitudinal dimension determines the length of a bunch, while the transverse dimensions determine its height and width. The beam phase space description is useful for analyzing the distribution of particles, which can be visualized as a "cloud" of points in six-dimensional phase space at a specific time. According to Liouville's theorem, in the absence of acceleration, the differential trace-space volume $d\Gamma \equiv dx\ dy\ dz\ dx'\ dy'\ dp_z$ remains constant at all times in the accelerator.

Liouville's theorem and the Hamiltonian equations for conservative systems allow us to track the motion of a beam and multiple particles in trace space. This can be achieved using a transfer matrix in the 6D trace space, which enables tracking anywhere along the beamline as:

$$\mathbf{X}(s)_f = \mathbf{M} \cdot \mathbf{X}(s)_i, \tag{10}$$

where the subscripts i and f represent the initial and final positions with respect to the reference trajectory and $\mathbf{M}$ is the transfer matrix which represents the linear optical elements (including drift spaces). The Eq. (10) equation can be expanded to full matrix form:

$$\begin{pmatrix} x \\ x' \\ y \\ y' \\ z \\ \delta \end{pmatrix}_f = \begin{pmatrix} \mathrm{M}_{11} & \mathrm{M}_{12} & \mathrm{M}_{13} & \mathrm{M}_{14} & \mathrm{M}_{15} & \mathrm{M}_{16} \\ \mathrm{M}_{21} & \mathrm{M}_{22} & \mathrm{M}_{23} & \mathrm{M}_{24} & \mathrm{M}_{25} & \mathrm{M}_{26} \\ \mathrm{M}_{31} & \mathrm{M}_{32} & \mathrm{M}_{33} & \mathrm{M}_{34} & \mathrm{M}_{35} & \mathrm{M}_{36} \\ \mathrm{M}_{41} & \mathrm{M}_{42} & \mathrm{M}_{43} & \mathrm{M}_{44} & \mathrm{M}_{45} & \mathrm{M}_{46} \\ \mathrm{M}_{51} & \mathrm{M}_{52} & \mathrm{M}_{53} & \mathrm{M}_{54} & \mathrm{M}_{55} & \mathrm{M}_{56} \\ \mathrm{M}_{61} & \mathrm{M}_{62} & M_{63} & \mathrm{M}_{64} & \mathrm{M}_{65} & \mathrm{M}_{66} \end{pmatrix} \begin{pmatrix} x \\ x' \\ y \\ y' \\ z \\ \delta \end{pmatrix}_i . \tag{11}$$

If there is no momentum offset, the transverse properties of a beam can be determined and analyzed, resulting in a four-dimensional (4D) system that excludes z and δ. The total transfer matrix $\mathbf{M}$ can be obtained by multiplying together the matrices that represent linear motion through various optical elements, including drifts, bends, and quadrupoles as:

$$\mathbf{M} = \mathbf{M_N M_{N-1} ......M_2 M_1}. \tag{12}$$

An electron bunch is a collection of electrons moving together at relativistic speeds. Its properties are determined by the total charge and the statistical distribution of the particles within the bunch. The beam is often modeled as a statistical ensemble described by a normalized distribution function $f(u,\, u')$ in the (u,u')-plane, where u is the horizontal or vertical displacement (x or y) relative to the ideal trajectory, and primes indicate differentiation with respect to s. To characterize the distribution, statistical central moments are used as:

$$\langle u \rangle = \int_{-\infty}^{+\infty} \int_{-\infty}^{+\infty} u \ f(u,u') \ du \ du' \approx \frac{1}{N} \sum_{i=1}^{N} u_i, \tag{13a}$$

$$\langle u' \rangle = \int_{-\infty}^{+\infty} \int_{-\infty}^{+\infty} u' \ f(u,u') \ du \ du' \approx \frac{1}{N} \sum_{i=1}^{N} u'_i, \tag{13b}$$

$$\left\langle u^2 \right\rangle = \int_{-\infty}^{+\infty} \int_{-\infty}^{+\infty} u^2 \ f(u,u') \ du \ du' \approx \frac{1}{N} \sum_{i=1}^{N} u_i^2, \tag{13c}$$

$$\left\langle u'^2 \right\rangle = \int_{-\infty}^{+\infty} \int_{-\infty}^{+\infty} u'^2 \ f(u,u') \ du \ du' \approx \frac{1}{N} \sum_{i=1}^{N} u_i^2, \tag{13d}$$

$$\langle uu' \rangle = \int_{-\infty}^{+\infty} \int_{-\infty}^{+\infty} u \ u' \ f(u,u') \ du \ du' \approx \frac{1}{N} \sum_{i=1}^{N} u_i u'_i, \tag{13e}$$

where N is the number of particles in the bunch. Additionally, the quantities σ_u and σ'_u are called *rms* beam size and beam divergence, and $\sigma_{uu'}$ is the correlation. These parameters are defined by the following relations:

$$\sigma_u^2 = \int_{-\infty}^{+\infty} \int_{-\infty}^{+\infty} (u - \langle u \rangle)^2 f(u,u') \ du \ du' \approx \frac{1}{N} \sum_{i=1}^{N} (u_i - \langle u \rangle)^2, \tag{14a}$$

$$\sigma_u'^2 = \int_{-\infty}^{+\infty} \int_{-\infty}^{+\infty} (u' - \langle u' \rangle)^2 \ f(u,u') \ du \ du' \approx \frac{1}{N} \sum_{i=1}^{N} (u'_i - \langle u' \rangle)^2, \tag{14b}$$

$$\sigma_{uu'} = \int_{-\infty}^{+\infty} \int_{-\infty}^{+\infty} (u - \langle u \rangle)(u' - \langle u' \rangle) f(u,u') \ du \ du' \approx \frac{1}{N} \sum_{i=1}^{N} (u_i - \langle u \rangle)(u'_i - \langle u' \rangle). \tag{14c}$$

Here, first order moments $\langle u \rangle$ and $\langle u' \rangle$ are 0 for a zero-centered beam distribution.

Longitudinal bunch distribution is also commonly described by its *rms* bunch length $\sigma_z = \sqrt{\langle z^2 \rangle}$ and energy spread $\sigma_{\delta_{\mathcal{E}}} = \sqrt{\langle \Delta\gamma^2 \rangle} / \langle \gamma_0 \rangle$. Here, $\delta_{\mathcal{E}}$ is defined as $\Delta\mathcal{E}/\mathcal{E}_0 = \Delta\gamma/\gamma_0$, where γ_0 stands for the Lorentz factor of the bunch's center of mass.

3.3.1 BEAM EMITTANCE AND BEAM MATRIX

The beam emittance is an intrinsic characteristic of a charged particle beam in a particle accelerator that quantifies its quality. Essentially, it represents the volume of phase space occupied by the beam. The emittance of a beam provides information on how well it can be transported over long distances or focused into a small space [46].

Liouville's theorem states that the area in phase space occupied by charged particles will remain constant under the influence of conservative forces [47]. Although the shape of the ellipse enclosing the distribution of particles may be distorted by focusing and defocusing elements along a beamline, the area of the ellipse remains constant, satisfying Liouville's theorem. Accelerator physicists typically describe a distribution of particles as being enclosed by an ellipse in phase space, where the area of the ellipse corresponds to the beam emittance. This can refer to either transverse phase space (spot size and divergence) or longitudinal phase space (bunch length and energy spread).

For the transverse motion, a diagram of the ellipse is shown in Fig. 19. The geometric emittance ϵ refers to the area of the beam ellipse in the (u, u') coordinate system and given by:

$$\int_{\text{ellipse}} du\ du' = \pi\epsilon. \tag{15}$$

The normalized and geometric emittances are related simply by

$$\epsilon_n = \gamma\beta\epsilon, \tag{16}$$

where β and γ are the Lorentz factors. The normalized emittance in an ideal machine would stay constant from the source throughout the transport. However, in reality, non-linear magnetic fields and wakefields are among the factors that degrade the emittance.

The beam ellipse is characterized by three independent parameters and one dependent parameter: $\alpha(s)$, $\beta(s)$, and $\gamma(s)$ are the Courant-Snyder parameters (also known as Twiss parameters) [48], and ϵ represents the geometrical emittance. It is important to note that the Twiss parameters differ from the Lorentz factors even though the notation is the same. In the case of linear motion, the distribution of the beam in two-dimensional (2D) phase space can be enclosed by an ellipse of the form:

$$\epsilon = \gamma u^2 + 2\alpha u u' + \beta u'^2, \tag{17}$$

where ϵ is called the geometric emittance, and $\pi\epsilon$ gives the area enclosed by the ellipse. The community uses different conventions to specify the fraction of the beam inside the ellipse. In proton accelerators, an ellipse containing 90% of the particles is considered the 90% emittance. On the other hand, the electron beam community commonly uses the *rms* emittance as defined by [49]:

$$\epsilon_{rms} = \sqrt{\sigma_u^2\sigma_{u'}^2 - \sigma_{uu'}^2} = \sigma_u\sigma_{u'}\sqrt{1 - r^2}, \tag{18}$$

where r is defined to be the correlation coefficient, $r = \sigma_{uu'}/\sqrt{\sigma_u^2\sigma_{u'}^2}$, whose absolute value is less than or equal to one. The correlation coefficient will be zero in the absence of correlation of the phase space variables, u and u'.

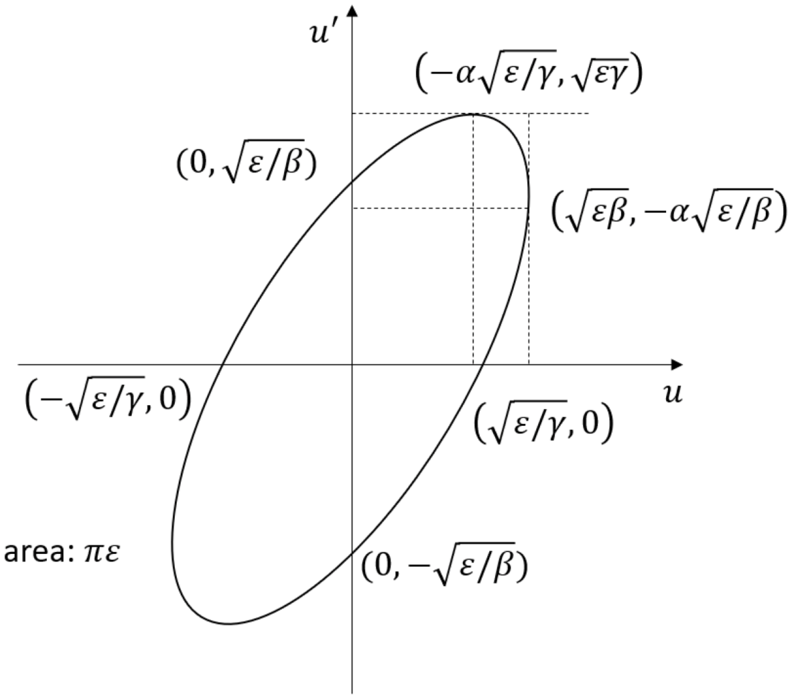

FIG. 19. Beam phase space ellipse characterized by the Twiss Parameters.

The three Courant-Snyder parameters, $\beta(s)$, $\alpha(s)$ and $\gamma(s)$, which are also called beam optical functions, are proportional to the three second moments of the beam distribution. The constant of proportionality is the *rms* beam emittance. This mathematical relation is expressed as follows [50]:

$$\begin{pmatrix} \beta \\ -\alpha \\ \gamma \end{pmatrix} = \frac{1}{\epsilon_{rms}} \begin{pmatrix} \langle u^2 \rangle \\ \langle uu' \rangle \\ \langle u'^2 \rangle \end{pmatrix} = \frac{1}{\epsilon_{rms}} \begin{pmatrix} \sigma_{11} \\ \sigma_{12} \\ \sigma_{22} \end{pmatrix}; \quad \text{with} \quad \gamma\beta - \alpha^2 = 1. \tag{19}$$

The relationship between the beam ellipse and the Courant-Snyder parameters can be understood by comparing Eq. (19) with Fig. 19. Specifically, $\sqrt{\epsilon\beta}$ corresponds to the beam half-width, $\sqrt{\epsilon\gamma}$ corresponds to the beam half-divergence, and α is the correlation term between u and u'. If $\alpha > 0$, the beam is converging; if $\alpha < 0$, the beam is diverging; and if $\alpha = 0$, the beam has a local minimum or maximum β, as $\alpha = -\beta'/2$ [50]. Additionally, from Eq. (19), we can see that the *rms* width of the beam is $\sqrt{\epsilon_{rms}\beta}$. Therefore, the beta

(β) function describes the beam envelope and must be kept small enough to avoid colliding the outermost particles with the beam chamber.

For the Gaussian distribution in (u, u') :

$$\begin{aligned} f(u,u') &= \frac{1}{2\pi\epsilon_{rms}} \exp\left(-\frac{\epsilon}{2\epsilon_{rms}}\right) \\ &= \frac{1}{2\pi\epsilon_{rms}} \exp\left(-\frac{\gamma u^2 + 2\alpha u u' + \beta u'^2}{2\epsilon_{rms}}\right). \end{aligned} \tag{20}$$

Changing the phase space coordinates to the normalized coordinates as:

$$u_n = \frac{u}{\beta}, \quad u'_n = \sqrt{\beta} u' + \frac{\alpha u}{\sqrt{\beta}}, \tag{21}$$

and normalizing the distribution function $f(u, u')$, we get

$$\begin{aligned} \int_{\infty}^{\infty}\int_{\infty}^{\infty} f(u,u')\ du\ du' &= \int_{\infty}^{\infty}\int_{\infty}^{\infty} \frac{1}{2\pi\epsilon_{rms}} \exp\left(-\frac{{u_n}^2 + {u'_n}^2}{2\epsilon_{rms}}\right) du_n\ du'_n \\ &= \int_{0}^{\infty} \frac{1}{2\pi\epsilon_{rms}} \exp\left(-\frac{\epsilon}{2\epsilon_{rms}}\right) \pi d\epsilon = 1. \end{aligned} \tag{22}$$

The average emittance is

$$\begin{aligned} \langle\epsilon\rangle &= \int_{0}^{\infty} \frac{1}{2\epsilon_{rms}} \exp\left(-\frac{\epsilon}{2\epsilon_{rms}}\right) \epsilon d\epsilon \\ &= 2\epsilon_{rms}. \end{aligned} \tag{23}$$

The beam *rms* emittance is equal to the half of the average beam emittance.

With this statistical description of the beam in hand, the 2 × 2 horizontal *beam matrix* also called *sigma matrix*, may be defined as:

$$\Sigma(s) \equiv \begin{pmatrix} \langle u^2\rangle & \langle uu'\rangle \\ \langle u'u\rangle & \langle u'^2\rangle \end{pmatrix} = \begin{pmatrix} \sigma_{11} & \sigma_{12} \\ \sigma_{21} & \sigma_{22} \end{pmatrix} = \epsilon_{rms} \begin{pmatrix} \beta(s) & -\alpha(s) \\ -\alpha(s) & \gamma(s) \end{pmatrix}, \tag{24}$$

Note that Det $(\Sigma(s)) = \epsilon_{rms}^2$. The beam matrix at any position s_2 from s_1 can be obtained using the known transfer matrices and the relation:

$$\Sigma(s_2) = \mathbf{M}\ \Sigma(s_1)\ \mathbf{M^T}, \tag{25}$$

where $\Sigma(s_1)$ is the beam matrix at position s_1, $\Sigma(s_2)$ is the beam matrix at position s_2, and $\mathbf{M}$ is the transfer matrix that describes the transformation from position s_1 to another position s_2. Equation (25) describes how observable *rms* beam sizes evolve as they move through the lattice. For a unimodular (Det $(\mathbf{M}) = 1$) matrix transformation with $|\mathrm{Tr}(\mathbf{M})| < 2$, the ellipses $\gamma u^2 + 2\alpha u u' + \beta u'^2 = \epsilon$ are invariant under the linear action of $\mathbf{M}$ implying that

$$\gamma_2 u_2^2 + 2\alpha_2 u_2 u_2' + \beta_2 u_2'^2 = \gamma_1 u_1^2 + 2\alpha_1 u_1 u_1' + \beta_1 u_1'^2 = \epsilon. \tag{26}$$

Applying the phase space coordinate changes from s_1 to s_2 using the transport matrix, and inverting the matrix with $\mathrm{Det}(\mathbf{M}) = 1$, we obtain

$$\begin{pmatrix} u_2 \\ u_2' \end{pmatrix} = \begin{pmatrix} \mathrm{M}_{11} & \mathrm{M}_{12} \\ \mathrm{M}_{21} & \mathrm{M}_{22} \end{pmatrix} \begin{pmatrix} u_1 \\ u_1' \end{pmatrix}; \begin{pmatrix} u_1 \\ u_1' \end{pmatrix} = \begin{pmatrix} \mathrm{M}_{22} & -\mathrm{M}_{12} \\ -\mathrm{M}_{21} & \mathrm{M}_{11} \end{pmatrix} \begin{pmatrix} u_2 \\ u_2' \end{pmatrix}. \tag{27}$$

Substituting the values of u_1 and u_1' from Eq. (27) and using the equation Eq. (26),

$$\begin{aligned} \gamma_2 u_2^2 + 2\alpha_2 u_2 u_2' + \beta_2 u_2'^2 = (\mathrm{M}_{22}^2\gamma_1 - 2\mathrm{M}_{21}\mathrm{M}_{22}\alpha_1 + \mathrm{M}_{21}^2\beta_1)u_2^2 + 2[-\mathrm{M}_{12}\mathrm{M}_{22}\gamma_1 + \\ (\mathrm{M}_{11}\mathrm{M}_{22} + \mathrm{M}_{12}\mathrm{M}_{21})\alpha_1 - \mathrm{M}_{11}\mathrm{M}_{21}\beta_1]u_2 u_2' + (\mathrm{M}_{12}^2\gamma_1 - 2\mathrm{M}_{12}\mathrm{M}_{11}\alpha_1 + \mathrm{M}_{11}^2\beta_1)u_2'^2. \end{aligned} \tag{28}$$

Solving Eq. (28), we get the changes in the ellipse or Twiss parameters expressed in matrix form as:

$$\begin{pmatrix} \gamma(s_2) \\ \alpha(s_2) \\ \beta(s_2) \end{pmatrix} = \begin{pmatrix} \mathrm{M}_{22}^2 & -2\mathrm{M}_{21}\mathrm{M}_{22} & \mathrm{M}_{21}^2 \\ -\mathrm{M}_{12}\mathrm{M}_{22} & \mathrm{M}_{11}\mathrm{M}_{22} + \mathrm{M}_{12}\mathrm{M}_{21} & -\mathrm{M}_{11}\mathrm{M}_{21} \\ \mathrm{M}_{12}^2 & -2\mathrm{M}_{12}\mathrm{M}_{11} & \mathrm{M}_{11}^2 \end{pmatrix} \begin{pmatrix} \gamma(s_1) \\ \alpha(s_1) \\ \beta(s_1) \end{pmatrix}. \tag{29}$$

At a new location s_2 along the beamline, the phase space ellipse still has the same area $\pi\epsilon$ as it did at the original location s_1. However, the ellipse parameters change as described by Eq. (29), resulting in a different shape and orientation of the phase space ellipse. This implies that the phase space ellipse undergoes continuous changes in shape and orientation as the beam propagates along the beamline, while the area of the ellipse remains constant.

Using Eq. (29), the beam parameters at any point along the beamline can be extrapolated with knowledge of the initial values of parameters α_1, β_1, and γ_1. Alternatively, we can express the elements of the transfer matrix $\mathbf{M}$ from s_1 to s_2 in terms of the optical functions at the initial and final locations as:

$$\mathbf{M}(s_1, s_2) = \begin{pmatrix} \sqrt{\frac{\beta_2}{\beta_1}}(\cos\phi + \alpha_1 \sin\phi) & \sqrt{\beta_2\beta_1}\sin\phi \\ \frac{1}{\sqrt{\beta_2\beta_1}}\left((\alpha_1 - \alpha_2)\cos\phi - (1 + \alpha_1\alpha_2)\sin\phi\right) & \sqrt{\frac{\beta_1}{\beta_2}}(\cos\phi - \alpha_2 \sin\phi) \end{pmatrix}, \tag{30}$$

where $\phi = (\phi_2 - \phi_1)$ is the betatron phase advance between the two locations, mathematically given by

$$\phi = \oint_{s_1}^{s_2} \frac{1}{\beta_u}\, ds. \tag{31}$$

3.3.2 THERMAL EMITTANCE

Thermal emittance is the emittance achieved when particles are emitted from a source at constant temperature. In photocathodes, it mainly depends on the illuminating wavelength, the degree of negative affinity, and the band structure of the photocathode material [51]. The statistical definition of the phase space normalized *rms* emittance in (x, x') plane is given by [52]:

$$\epsilon_{nx} = \frac{1}{mc}\sqrt{\langle x^2\rangle \langle p_x^2\rangle - \langle xp_x\rangle}. \tag{32}$$

The thermal emittance can be calculated by assuming the electrons from the cathode are emitted uniformly and isotropically within a radius r in the presence of an accelerating field. Introducing the transverse thermal energy of the cathode $k_BT_\perp$, and invoking the equipartition theorem, we write $\frac{1}{2}m\langle v_x^2\rangle = \frac{1}{2}k_BT_\perp$, where k_B is Boltzmann constant and $T_\perp$ is transverse tempearature. For nonrelativistic photoelectrons, $v_x = p_x/m$ represents the transverse component of the velocity. The correlation term in Eq. (32) is absent at the photocathode surface, so the normalized thermal emittance is given by [51]:

$$\epsilon_{nx} = \sigma_x\sqrt{\frac{k_BT_\perp}{mc^2}}, \tag{33}$$

where $\sigma_x = \langle x^2\rangle$ is the *rms* laser spot size on the cathode.

3.4 LINEAR TRANSVERSE BEAM DYNAMICS

Particles in a beam undergo transverse and longitudinal oscillations around the reference trajectory or closed orbit during transport along the beamline. The transverse (horizontal or vertical) differential equation of motion of a particle in an accelerator, assuming no momentum deviation from designed momentum is given by the linearized Hills's equation [52, 53] :

$$u'' + K_u(s)u = 0, \tag{34}$$

where u is the horizontal or vertical displacement (x or y) relative to the ideal trajectory, and primes indicate differentiation with respect to s. The focusing function $K_u(s)$ describes the magnetic field strength present at a location s along the beamline, and it is periodic for a circular machine.

For the linear motion through the beamline elements, a solution of Eq. (34) can be represented in a matrix form with cosine-like and sine-like elements:

$$\begin{pmatrix} u_f \\ u'_f \end{pmatrix} = \begin{pmatrix} \mathrm{M}_{11} & \mathrm{M}_{12} \\ \mathrm{M}_{21} & \mathrm{M}_{22} \end{pmatrix} \begin{pmatrix} u_i \\ u'_i \end{pmatrix} = \begin{pmatrix} C(s) & S(s) \\ C'(s) & S'(s) \end{pmatrix} \begin{pmatrix} u_i \\ u'_i \end{pmatrix}, \tag{35}$$

where, $\begin{pmatrix} u_{i,f} \\ u'_{i,f} \end{pmatrix}$ are initial(final) positions of a particle and $\mathbf{M}$ is the transport matrix.

A typical electron injector comprises of an electron source and solenoidal lenses that form an electron gun, as well as drift spaces, dipole and quadrupole magnets, and various types of RF cavities, such as a buncher, a chopper, and SRF accelerating cavities. Sextupole and octupole magnets may also be included for aberration compensation. Most of the accelerator-transport components are described using a paraxial approximation solution of Eq. (34). A thorough derivation of first and second-order accelerator optics can be found in Ref. [54].

3.4.1 MOTION IN DRIFT ELEMENT

A drift section in an accelerator is a region of the beam pipe where there are no electromagnetic fields, and particles move in a straight line without experiencing external forces. However, in such field-free regions, the particles in the electron beam are still affected by the internal Coulomb fields, known as space-charge forces. Ignoring the space-charge forces, the linearized axial motion of the electrons can be represented in a matrix form with $K_x(s) = K_y(s) = 0$ in Eq. (34) as follows:

$$\mathbf{M}_{\text{drift}} = \begin{pmatrix} 1 & L & 0 & 0 \\ 0 & 1 & 0 & 0 \\ 0 & 0 & 1 & L \\ 0 & 0 & 0 & 1 \end{pmatrix}, \tag{36}$$

where L is the length of the field-free region. The space-charge forces will be included in the simulations later in this thesis.

3.4.2 MOTION IN DIPOLE CORRECTOR/BEND

Dipole magnetic correctors are necessary to adjust the alignment of the beam in the beamline. The effect of a dipole magnet can be described as a change in the beam's momentum in the transverse plane, which is determined by the magnetic rigidity ($B\rho$) and bending radius (ρ) following the equation $B\rho = p/q$. To correct for the vertical and horizontal displacement, dipole correctors are usually arranged in pairs to address both the horizontal and vertical kicks. The result can be expressed in a concise form as:

$$\begin{pmatrix} \delta p_x \\ \delta p_y \end{pmatrix} = \begin{pmatrix} d_x \\ d_y \end{pmatrix}. \tag{37}$$

Here (d_x, d_y) is a constant vector, where $d_{x,y}$ corresponds to the dipole kick value in the x or y plane.

A sector dipole is a type of dipole magnet that bends the beam in the horizontal plane with a bending angle θ and a bending radius ρ. Its end faces and fields are perpendicular to the design trajectory at both the entrance and exit. As the dipole magnet bends only in one direction, the vertical direction can be considered as a drift. Therefore, the transfer matrix for a sector dipole with $K_x(s) = 1/\rho^2(s)$ and $K_y(s) = 0$ in Eq. (34) becomes:

$$\mathbf{M}_{\text{sector}} = \begin{pmatrix} \cos\theta & \rho\sin\theta & 0 & 0 \\ -\frac{1}{\rho}\sin\theta & \cos\theta & 0 & 0 \\ 0 & 0 & 1 & \rho\theta \\ 0 & 0 & 0 & 1 \end{pmatrix}. \tag{38}$$

It is worth noting that the transfer matrix for a sector dipole resembles a scaled rotation in the horizontal plane and a drift of length $L = \rho\theta$ in the vertical plane.

In a rectangular dipole, the bending magnet field abruptly starts and stops along the particle trajectory, requiring correction of the previous matrix and consideration of edge focusing. To obtain the complete matrix for the rectangular dipole with edge focusing, three matrices must be multiplied: edge focusing for the entrance, sector dipole, and edge focusing for the exit. So, the complete matrix for the rectangular dipole with edge focusing becomes [52]:

$$\mathbf{M}_{\text{rect}} = \begin{pmatrix} 1 & \rho\sin\theta & 0 & 0 \\ 0 & 1 & 0 & 0 \\ 0 & 0 & \cos\theta & \rho\sin\theta \\ 0 & 0 & -\frac{1}{\rho}\sin\theta & \cos\theta \end{pmatrix}. \tag{39}$$

The transfer matrix for a rectangular dipole can be decomposed into a drift of length $L = \rho\sin\theta$ in the horizontal deflecting plane and a sector dipole in the vertical non-deflecting plane.

3.4.3 QUADRUPOLE FOCUSING

Quadrupoles are accelerator magnets that introduce linear focusing that depends on the position coordinate s. If Hill's equation has focusing in the horizontal direction, then it will have defocusing in the vertical direction and vice versa. The transfer matrix of a horizontally focusing (vertically defocusing) quadrupole with length L is given by [50]:

$$\mathbf{M}_{\text{quad}} = \begin{pmatrix} \cos kL & \frac{1}{k}\sin kL & 0 & 0 \\ -k\sin kL & \cos kL & 0 & 0 \\ 0 & 0 & \cosh kL & \frac{1}{k}\sinh kL \\ 0 & 0 & k\sinh kL & \cosh kL \end{pmatrix}, \tag{40}$$

where $k = \sqrt{K}$ and $K = \text{sgn}(q)B'/(B\rho)$ are both positive-definite. Note that the sign of the derivative of the magnetic field ($B' = dB_y/dx$) depends on the sign of the charge of the particle (q).

When a quadrupole is horizontally defocusing, the 2×2 matrix sub-blocks for the horizontal and vertical planes are swapped. This occurs when $k = \sqrt{-K}$ is positive and K is negative in Hill's equation. When the quadrupole is short, a close approximation can be achieved by setting the length $L \to 0$ while keeping KL constant. The resulting transfer matrix is:

$$\mathbf{M}_{\text{thin}-\text{quad}} = \begin{pmatrix} 1 & 0 & 0 & 0 \\ -1/f & 1 & 0 & 0 \\ 0 & 0 & 1 & 0 \\ 0 & 0 & 1/f & 1 \end{pmatrix}, \tag{41}$$

where $KL = 1/f$, $L << |f|$, and f is the focal length of the quadrupole lens.

The motion equations in the $x - y$ plane for skew quadrupoles are as follows [52]:

$$\begin{aligned} x'' + \frac{B'}{B\rho}y = x'' + k^2 y = 0, \\ y'' + \frac{B'}{B\rho}x = y'' + k^2 x = 0. \end{aligned} \tag{42}$$

The skew quadrupole provides focusing in the $x + y$ plane and defocusing in the $x - y$ plane. The corresponding transformation matrix for the skew quadrupole is provided by [52]:

$$\mathbf{M}_{\text{skew}-\text{quad}} = \frac{1}{2}\begin{pmatrix} c^+ & \frac{s^+}{k} & c^- & \frac{s^-}{k} \\ -ks^- & c^+ & -ks^+ & c^- \\ c^- & \frac{s^-}{k} & c^+ & \frac{s^+}{k} \\ -ks^+ & c^- & -ks^- & c^+ \end{pmatrix}, \tag{43}$$

where the short-hand notations $c^\pm = \cos kL \pm \cosh kL$ and $s^\pm = \sin kL \pm \sinh kL$ are used. In the thin lens approximation where the length of the quadrupole becomes very small ($L \to 0$) while maintaining the integrated magnet strength or the focal length f, the Eq. (43) for the matrix reduces to the simple form:

$$\mathbf{M}_{\text{skew}-\text{thin}} = \begin{pmatrix} 1 & 0 & 0 & 0 \\ 0 & 1 & -\frac{1}{f} & 0 \\ 0 & 0 & 1 & 0 \\ -\frac{1}{f} & 0 & 0 & 1 \end{pmatrix}, \tag{44}$$

where the focal length is defined as $f^{-1} = KL$.

3.4.4 SOLENOID FOCUSING

Solenoid magnets are frequently used in accelerators to focus low energy beams. In a solenoid, the longitudinal magnetic field on the axis is peaked at the center of the solenoid, decreases toward the ends, and approaches zero far away from the solenoid. In contrast, the radial magnetic field is peaked near the ends of the solenoid. A sketch of a solenoid and its field is shown in Fig. 20.

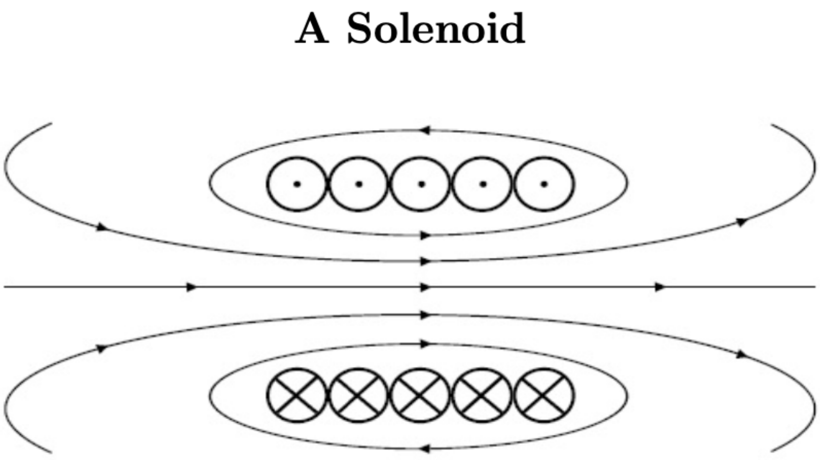

FIG. 20. Magnetic field lines of a solenoid.

The linear optics longitudinal and radial fields of a solenoid can be expressed as follows:

$$B_z(r,z) = B_z(r=0,z) = B_z; \quad B_r(r,z) = -\frac{r}{2}B_z', \tag{45}$$

where z is the distance along the solenoid axis, r is the radial distance from the solenoid axis, and the prime denotes a derivative with respect to z. Such a field may be described by a single azimuthal component (A_θ) of the magnetic vector potential as

$$A_\theta = \frac{1}{2}B_z(z)r. \tag{46}$$

The canonical angular momentum (CAM) P_θ is

$$P_\theta = \gamma m r^2\dot{\theta} + qrA_\theta = \gamma m r^2\dot{\theta} + \frac{1}{2}qB_z r^2, \tag{47}$$

where $\dot{\theta}$ is the angular velocity. The conservation of CAM, due to the axial symmetry of the solenoid, is known as Busch's theorem.

When a particle enters the solenoid parallel to the axis and with specific initial conditions ($A_\theta = 0$, $\dot{\theta} = 0$ and $\beta_z = \beta$) and thus $P_\theta = 0$. CAM is conserved due to Busch's theorem and so $\dot{\theta} = eB_z/2\gamma m = \omega_L$. Here, ω_L is the Larmor frequency. The radial equation of motion for this particle takes on the form of a harmonic oscillator equation in r as:

$$r'' + k(s)r = 0, \tag{48}$$

where $k(s) = (eB_z/2\beta\gamma mc)^2 = \omega_L^2/\beta^2c^2 = (B_z/2B\rho)^2$ is the focusing strength. The Larmor frequency ω_L determines the rotation of the beam around its axis inside the solenoidal lens. The rotation ceases when the particle exits the solenoid field. This means that a solenoidal lens not only images the electron beam but also causes it to rotate. The focal length of the solenoid f is given by:

$$\frac{1}{f} = \frac{q^2}{4\beta^2\gamma^2m^2c^2}\int_{-\infty}^{\infty} B_z^2 dz = \frac{q^2}{4p^2}\int_{-\infty}^{\infty} B_z^2 dz. \tag{49}$$

It is important to note that the focal length of a solenoid lens is proportional to the square of the momentum and inversely proportional to the square of the charge of the particles. This means that the solenoid lens will be more effective for particles with low momentum p and high charge q.

We can examine how a particle behaves upon entering a solenoid with its velocity along the z-axis, $\mathbf{v} = v\hat{z}$. The radial component of the field, also known as fringe field, gives rise to angular momentum in the beam, given by $\Delta p_\theta = qrB_z/2$. This means that the radial magnetic field causes an angular kick that alters the beam's divergence as:

$$\begin{aligned} \Delta x' &= k_L y; \\ \Delta y' &= -k_L x, \end{aligned} \tag{50}$$

where $k_L = qB_z/2p_z = B_z/2B\rho$. The magnetic field inside the solenoid is uniform and aligned along the z-axis, resulting in circular motion of the particle in the $x - y$ plane. The total rotation angle of the particle over the length L of the solenoid can be calculated as follows:

$$\theta = \omega t_{cross} = -\frac{qB_z}{m}\frac{L}{v_z} = -\frac{B_z L}{B\rho} = -2k_L L. \tag{51}$$

Here, t_{cross} is the time taken by the charged particle to cover the distance L along the length of the solenoid. The solenoid can be divided into three parts, the entry region, body region, and exit region, for the purpose of approximation. If we assume that the angular kick happens only at a specific longitudinal position at the entrance of the solenoid, the corresponding matrix is:

$$\mathbf{M}_{\text{entry}} = \begin{pmatrix} 1 & 0 & 0 & 0 \\ 0 & 1 & k_L & 0 \\ 0 & 0 & 1 & 0 \\ -k_L & 0 & 0 & 1 \end{pmatrix}. \tag{52}$$

The matrix that describes the particle's behavior at the exit of the solenoid is identical to the one at the entrance, except for a reversal in the sign of the kick. The corresponding matrix at the exit can be expressed as:

$$\mathbf{M}_{\text{exit}} = \begin{pmatrix} 1 & 0 & 0 & 0 \\ 0 & 1 & -k_L & 0 \\ 0 & 0 & 1 & 0 \\ k_L & 0 & 0 & 1 \end{pmatrix}. \tag{53}$$

The angle and position transformations result in the following transfer matrix for the body of the solenoid:

$$\mathbf{M}_{\text{body}} = \begin{pmatrix} 1 & \frac{\sin 2k_L L}{2k} & 0 & \frac{1-\cos 2k_L L}{2k_L} \\ 0 & \cos 2k_L L & 0 & \sin 2k_L L \\ 0 & -\frac{1-\cos 2k_L L}{2k_L} & 1 & \frac{\sin 2k_L L}{2k_L} \\ 0 & -\sin 2k_L L & 0 & \cos 2k_L L \end{pmatrix}. \tag{54}$$

The complete transfer matrix for a solenoid with a magnetic field strength of B and a length of L can be obtained by multiplying the entry, body, and exit matrices together as follows [52]:

$$\mathbf{M}_{\text{solenoid}} = \begin{pmatrix} c^2 & \frac{1}{k_L}sc & sc & \frac{1}{k_L}s^2 \\ -k_L sc & c^2 & -k_L s^2 & sc \\ -sc & -\frac{1}{k_L}s^2 & c^2 & \frac{1}{k_L}sc \\ k_L s^2 & -sc & -k_L sc & c^2 \end{pmatrix}, \tag{55}$$

where the short-hand notations $c = \cos k_L L$ and $s = \sin k_L L$ are used. The determinant of the diagonal blocks $\mathbf{M}_{xx}$ and $\mathbf{M}_{yy}$ of the solenoid matrix is not equal to 1, which means that the emittances of xx' and yy' are not preserved. Additionally, the non-null $\mathbf{M}_{xy}$ and $\mathbf{M}_{yx}$ matrices indicate a coupling between the transverse dimensions through a solenoid. Therefore, a solenoid can be seen as having an effect of both transverse dimensions focusing and rotation of the xy space of angle $k_L L$.

The thin lens approximation can be achieved by considering a small length L and a small angle θ, and by keeping only the first term of the Taylor series for the cosine and sine. In this case, the transfer matrix takes the following form:

$$\mathbf{M}_{\text{solenoid}} = \begin{pmatrix} 1 & 0 & 0 & 0 \\ -\frac{1}{f} & 1 & 0 & 0 \\ 0 & 0 & 1 & 0 \\ 0 & 0 & -\frac{1}{f} & 0 \end{pmatrix}, \tag{56}$$

where f is the focal length given by:

$$\frac{1}{f} = k_L^2 L = \frac{q^2 B_z^2}{4p^2} L. \tag{57}$$

3.4.5 TRANSVERSE RADIOFREQUENCY DEFOCUSING

In a linac, acceleration is commonly achieved through radiofrequency (RF) electric fields generated inside a structure called a cavity. Although there are various types of cavities, their specific details are not crucial for analyzing the effect on the transverse motion of beam particles. What matters is that an accelerating cavity concentrates high-frequency electromagnetic fields within a small space around the beam axis.

A cylindrical linac cavity operates in a resonating mode and has three non-zero field components, namely E_z, E_r and B_θ, where $\mathbf{E}$ is the electric field and $\mathbf{B}$ is the magnetic flux density, while z, r, and θ represent the longitudinal, radial, and azimuthal coordinates respectively. When considering the EM fields in a cylindrical structure near the beam axis, it can be approximated that the longitudinal electric field is independent of the radial position [55]:

$$E_z(r, z, t) = E(0, 0, z)\cos(\omega t + \phi_s), \tag{58}$$

where ω is the angular frequency and ϕ_s is the phase as the particle passes the center of the cavity. If the longitudinal electric field $E_z(r, z, t)$ is independent of the radial position r near the axis, then according to the divergence and curl relationships of Maxwell's equations, the following transverse fields are obtained:

$$E_r = -\frac{r}{2}\frac{\partial E_z}{\partial z}, \qquad B_\theta = \frac{r}{2c^2}\frac{\partial E_z}{\partial t}. \tag{59}$$

The resulting Lorentz force leads to a change in transverse momentum of a particle of charge q and velocity βc is given by integration of the transverse fields across the length L of the accelerating cavity:

$$\Delta p_r = q\int_{-\frac{L}{2}}^{\frac{L}{2}} (E_r - \beta c B_\theta)\frac{dz}{\beta c}. \tag{60}$$

Using Eq. (59), Eq. (60) becomes:

$$\Delta p_r = -\frac{q}{2}\int_{-\frac{L}{2}}^{\frac{L}{2}} r\left(\frac{\partial E_z}{\partial z} + \frac{\beta}{c}\frac{\partial E_z}{\partial t}\right)\frac{dz}{\beta c}. \tag{61}$$

The partial derivative with respect to the longitudinal position can be substituted with the total derivative using:

$$\frac{dE_z}{dz} = \frac{\partial E_z}{\partial z} + \frac{1}{\beta c}\frac{\partial E_z}{\partial t}. \tag{62}$$

we get, the radial momentum impulse is

$$\Delta p_r = -\frac{qr}{2\beta c}\int_{-\frac{L}{2}}^{\frac{L}{2}} \left[\frac{dE_z}{dz} + \frac{\beta}{c}\frac{\partial E_z}{\partial t}\right] dz. \tag{63}$$

The integral over the total derivative vanishes if the interval L extends to zero field at both ends, or if the field is periodic with period L. In these cases, the radial momentum change can be expressed as:

$$\Delta p_r = -\frac{qr\omega}{2\beta^2\gamma^2c^2}\int_{-\frac{L}{2}}^{\frac{L}{2}} E(0, 0, z)\sin(\omega t + \phi_s)dz. \tag{64}$$

Suppose a particle is located at the origin at time $t = 0$, so that $\omega t = kz$, where $k = 2\pi/\beta\lambda$. Using the trigonometric identity, the radial momentum change can be written as:

$$\Delta p_r = -\frac{qr\omega}{2\beta^2\gamma^2c^2}\sin\phi_s\int_{-\frac{L}{2}}^{\frac{L}{2}} E(0, 0, z)\cos kz\ dz. \tag{65}$$

Substituting $p_r = mc\beta\gamma r'$ and using $\int_{-L/2}^{L/2} E(0,0,z)\cos kz\ dz = E_{acc}.L = V_c$ and $L = \beta\lambda/2$, where E_{acc} is the accelerating gradient and V_c accelerating cavity voltage, we obtain:

$$\Delta(\gamma\beta r') = -\frac{\pi q V_c \sin\phi_s}{mc^2\gamma^2\beta^2\lambda} r. \tag{66}$$

Equation (66) indicates that the amount of radial deflection in a RF cavity is directly proportional to the accelerating voltage, the radial position, and the sine of the RF phase, while being inversely proportional to $(\beta\gamma)^2$ and the RF wavelength λ. Equation (66) provides us with the transverse divergence change as:

$$\Delta(\gamma\beta x') = kx; \quad \Delta(\gamma\beta y') = ky, \tag{67}$$

where

$$k = -\frac{\pi q V_c \sin\phi_s}{mc^2\gamma^2\beta^2\lambda}. \tag{68}$$

Since the usual coordinate system use x' and y' one has first to transform to normalized momentum, apply the equations above and the change in beam energy, and then transform back into the x' y'. The total transfer matrix for a RF defocusing cavity is given by

$$\mathbf{M}_{\text{rfd}} = \begin{pmatrix} 1 & 0 \\ 1/(\beta\gamma)_f & 1 \end{pmatrix} \begin{pmatrix} 1 & 0 \\ k & 1 \end{pmatrix} \begin{pmatrix} 1 & 0 \\ 0 & (\beta\gamma)_i \end{pmatrix} = \begin{pmatrix} 1 & 0 \\ k/(\beta\gamma)_f & (\beta\gamma)_i/(\beta\gamma)_f \end{pmatrix}. \tag{69}$$

Here, $(\beta\gamma)_i$ and $(\beta\gamma)_f$ represent the initial and final relativistic factors, $\beta\gamma$, before and after the cavity, respectively.

3.5 DISPERSION

The momentum of particles in a beam varies within a finite range around a fixed reference momentum p_0, which creates a dispersion in the system. For a relative momentum deviation, expressed as $\delta = \Delta p/p_0$, the dispersion is found by the inhomogeneous Hill's equations:

$$\begin{aligned} x''(s) + K(s)x(s) &= \frac{\delta}{\rho(s)}, \\ y''(s) + K(s)y(s) &= 0, \end{aligned} \tag{70}$$

assuming that dynamics of off-momentum particles are important only in the horizontal plane, and there is no bending in the vertical direction. When particles pass through bending elements, their trajectories become dispersed by a certain amount, denoted as $D\delta$. Along the central design trajectory, the total displacement x of a particle can be calculated as follows:

$$x(s) = x_\beta(s) + x_D(s) = x_\beta(s) + D(s)\delta, \tag{71}$$

where $x_D(s)$ describes the deviation of the closed orbit for an off-momentum particle with $p = p_0 + \Delta p$ and $x_\beta(s)$ describes the betatron oscillation around the orbit $x_D(s)$. The equation for horizontal motion (Eq. (70)) can be split into two parts:

$$\begin{aligned} x''_\beta(s) + K(s)x_\beta(s) &= 0, \\ D''(s) + K(s)D(s) &= \frac{\delta}{\rho(s)}. \end{aligned} \tag{72}$$

The trajectory of dispersion inside a magnet is determined by the solution of a dispersion equation:

$$D(s) = S(s)\int_0^t \frac{1}{\rho(t)}C(t)\ dt - C(s)\int_0^t \frac{1}{\rho(t)}S(t)\ dt. \tag{73}$$

The solution for the position and divergence coordinates of particles with off-momentum can be expressed as:

$$\begin{pmatrix} x(s) \\ x'(s) \\ \delta(s) \end{pmatrix} = \begin{pmatrix} C & S & D \\ C' & S' & D' \\ 0 & 0 & 1 \end{pmatrix} \begin{pmatrix} x_0 \\ x'_0 \\ \delta_0 \end{pmatrix}. \tag{74}$$

For example, for focusing bend, the solution given by Eq. (74) can be represented by 3×3 matrix as

$$\begin{pmatrix} x(s) \\ x'(s) \\ \delta \end{pmatrix} = \begin{pmatrix} \cos\theta & \rho\sin\theta & \rho(1-\cos\theta) \\ -\frac{1}{\rho}\sin\theta & \cos\theta & \sin\theta \\ 0 & 0 & 1 \end{pmatrix} \begin{pmatrix} x(s_0) \\ x'(s_0) \\ \delta \end{pmatrix}, \tag{75}$$

where bending angle $\theta = s/\rho$. Since $x(s) = D(s)\delta$, where $D(s)$ is the dispersion function. Dividing by δ on both sides of Eq. (75), we get

$$\begin{pmatrix} D(s) \\ D'(s) \\ 1 \end{pmatrix} = \begin{pmatrix} \cos\theta & \rho\sin\theta & \rho(1-\cos\theta) \\ -\frac{1}{\rho}\sin\theta & \cos\theta & \sin\theta \\ 0 & 0 & 1 \end{pmatrix} \begin{pmatrix} D(s_0) \\ D'(s_0) \\ 1 \end{pmatrix}. \tag{76}$$

If we have access to the 3×3 transport matrix and the dispersion function and its derivative at the starting point s_0, we can determine the dispersion $D(s)$ at any downstream location s along the beamline. It is important to note that the simplified dipole calculation provided here is for illustrative purposes only, and does not take into account edge focusing in the dipole. When edge focusing is included, a slightly different 3×3 transport matrix is obtained [52].

At any given location, the *rms* beam size can be determined by taking into account two distinct factors: the betatron motion of particles and the finite momentum spread present in the beam. The horizontal beam size is given by

$$\sigma_x(s) = \sqrt{\epsilon_x \beta_x + D_x^2(s)\sigma_\delta^2}, \tag{77}$$

where ϵ_x is the horizontal beam emittance and σ_δ is the rms relative momentum spread. Similarly, the angular beam divergence $\sigma_{x'}(s)$ is given by

$$\sigma_{x'}(s) = \sqrt{\epsilon_x \gamma_x(s) + D_x'^2(s)\sigma_\delta^2}, \tag{78}$$

where $D_x'(s)$ is the dispersion derivative along the beamline.

3.6 LONGITUDINAL BEAM DYNAMICS IN A LINAC

To accelerate charged particles, a non-zero force in the direction of motion is required. Such fields are known as longitudinal accelerating fields and are responsible for imparting energy to the charged particles. However, the use of electrostatic high voltages is limited due to electric breakdown at around 10 million volts. Instead, modern high-energy particle accelerators rely on radio frequency (RF) cavities that operate at microwave frequencies to accelerate charged particles. In this section, we will explore how charged particles interact with the longitudinal electric field to facilitate the process of particle acceleration.

3.6.1 ENERGY GAIN IN A RF CAVITY

R. Wideroe introduced the concept of creating accelerating fields in resonating RF cavities [56]. These cavities are fed with traveling electromagnetic waves that generate a longitudinal electric field, capable of accelerating charged particles. In a linac, a series of RF cavities is typically used to efficiently accelerate particles. The rate of change of energy for a given particle per passage through an SRF cavity is

$$\frac{d\mathcal{E}}{dt} = \frac{d}{dt}(\gamma mc^2) = e\mathbf{E}(\mathbf{r}, t) \cdot \mathbf{v}, \tag{79}$$

where $\mathbf{E}(\mathbf{r}, t)$ is the electric field, and $\mathbf{v}$ is the velocity of the particle, $\mathbf{r}$ is the position coordinate vector. For particles moving mainly in the z direction, only the on-axis component of the electric field needs to be considered, while ignoring any radial dependence [55] as

$$E_z(r, z, t) = E(0, 0, z)\cos(\omega t + \phi_s), \tag{80}$$

the total energy gain per passage is given by

$$\begin{aligned} \Delta\mathcal{E} = \Delta(\gamma mc^2) &= e\int_{-\infty}^{\infty} E(0, 0, z)\cos\left(\frac{\omega z}{\beta c} + \phi_s\right) dz \\ &= eV_c \cos\phi_s, \end{aligned} \tag{81}$$

Here, V_c is the accelerating cavity voltage for the charge particles and is defined as

$$V_c = \left| \int_{-\infty}^{\infty} E_z(0,0,z) \exp\left(i\frac{\omega z}{\beta c} \right) dz \right|, \tag{82}$$

where ω is the angular frequency, and ϕ_s is the phase of the particle passing through the cavity with respect to the crest[1] (maximum) phase when the field pattern is placed with even symmetry on the z axis. Here, z is the beam axial distance, L is the effective length of the RF cavity, given by $L = \beta\lambda_{RF}/2$, where λ_{RF} is the RF wavelength, β is the normalized velocity, and c is the speed of light in a vacuum.

The accelerating field E_{acc} is defined by

$$E_{acc} = \frac{V_c}{L}. \tag{83}$$

The accelerating gradient E_{acc} is normalized by the cavity length L and is expressed in the unit of [MV/m].

3.6.2 M_{56} OF A DRIFT

Assume an electron with a velocity $v = c\beta$ and relativistic momentum $p = \gamma m v = \gamma\beta m c$ goes through a drift length L, where m is the electron mass, and c is the speed of light. To cross a drift of length L, the reference particle needs time

$$t = \frac{L}{v} = \frac{L}{\beta c}. \tag{84}$$

The change in time to cover distance L for the particle with higher or lower energy is given by

$$\Delta t = -\frac{L\Delta\beta}{\beta^2 c} = -\frac{L}{\beta c}\frac{\Delta\beta}{\beta}. \tag{85}$$

Note that $\Delta t < 0$ is negative for a higher-energy particle and $\Delta t > 0$ for the lower-energy particle than the reference particle in a bunch.

Now, writing the location of a particle with respect to the reference particle, considering $\Delta t < 0$, is:

$$\Delta z = -\beta c \Delta t = L\frac{\Delta\beta}{\beta}. \tag{86}$$

---

[1] For sin function, the crest phase is 90^0, and for cos function, the crest phase is 0^0. Harmonic cavity section uses cos function to denote the crest phase.

Now, using the relativistic momentum equation $p = \beta\gamma mc$, the fractional change in relativistic momentum of a particle with the reference particle is given by:

$$\begin{aligned} p &= \gamma\beta mc = mc\beta(1-\beta^2)^{-1/2}, \\ \Delta p &= mc\left((1-\beta^2)^{-1/2} + \beta^2(1-\beta^2)^{-3/2}\right)\Delta\beta, \\ \Delta p &= mc(1-\beta^2)^{-3/2})(1-\beta^2+\beta^2)\Delta\beta = mc\gamma^3\Delta\beta, \\ \therefore\ \frac{\Delta p}{p} &= \frac{mc\gamma^3}{mc\gamma\beta}\Delta\beta = \gamma^2\frac{\Delta\beta}{\beta}. \end{aligned} \tag{87}$$

So, from Eq.(86) and Eq.(87), the following expression is obtained.

$$\Delta z = \frac{L}{\gamma^2}\frac{\Delta p}{p} = \frac{L}{\gamma^2}\delta, \tag{88}$$

where $\delta = \Delta p/p$ is the fractional change of momentum of a particle with respect to the reference particle.

Since the distance change can be written as

$$\Delta z = \mathrm{M}_{56}\frac{\Delta p}{p}, \tag{89}$$

then

$$\mathrm{M}_{56} = \frac{L}{\gamma^2}. \tag{90}$$

This suggests that longitudinal motion is possible when a particle within the beam bunch is not moving with relativistic velocity, and there is a difference in the energy of particles within the bunch. The M_{56} depends on the distance (L) and γ^2.

3.6.3 RF BUNCHER

An RF cavity is used to introduce a velocity difference between the particles of an electron bunch. The bunching RF cavity is a single-cell copper structure [57] that operates near zero crossing of the RF phase. At zero crossing, the tail particles will receive an added energy while the head particles will receive an energy decrease. After traversing a drift, the bunch length is decreased; and the bunch is compressed. Ballistic compression is carried out by chirping an electron bunch in a chirper cavity (RF cavity) at zero crossing, followed by a drift where slow electrons at the head move back with respect to the centroid and fast electrons at the tail catch up with the centroid as shown in Fig. 21.

Consider an ideal short bunching cavity designed to create a longitudinal waist after a drift distance L. At the entrance of the buncher, downstream of the buncher, and at the

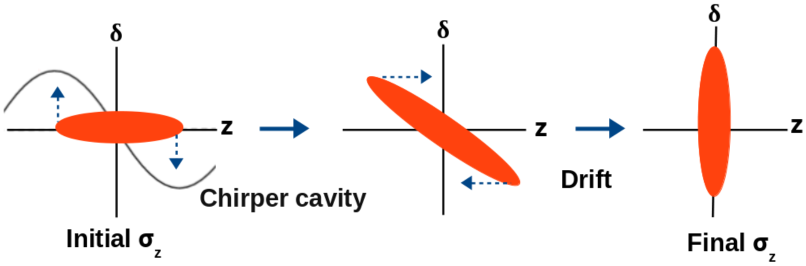

FIG. 21. The schematic of the action of the buncher along the beam transport line.

end of the drift, let $(\Delta z_1,\ \delta_1)$, $(\Delta z_2,\ \delta_2)$, and $(\Delta z_3,\ \delta_3)$ denote the longitudinal position z and fractional momentum $\delta = \Delta p/p$, where Δ indicates the deviation from the synchronous value.

From the relativistic energy-momentum relation $\mathcal{E}\Delta\mathcal{E} = pc^2\Delta p$ and $\mathcal{E} = \gamma mc^2$ and the relativistic momentum $p = \gamma\beta mc$, one easily obtains:

$$\Delta p = \frac{\Delta\mathcal{E}}{\beta c}. \tag{91}$$

A particle located at Δz with respect to the bunch center arrives at the buncher cavity at a time given by:

$$\Delta t = -\frac{\Delta z}{\beta c}, \tag{92}$$

where the negative sign indicates that the particle arrives earlier than at the center. If the buncher is at the positive-going zero crossing, the energy gain (change) using the energy gain equation $\Delta\mathcal{E} = eV\sin\omega t$, where V is the buncher voltage, is given by:

$$\Delta\mathcal{E} = eV\sin\omega t = eV\omega\Delta t. \tag{93}$$

This holds true for bunches much shorter than the RF wavelength.

In linear approximation of thin RF buncher cavity, the momentum offset δ changes but the longitudinal offset Δz does not. So using Eq. (91), Eq. (92), and Eq. (93), the linear transfer matrix equation for the buncher cavity is:

$$\begin{pmatrix}\Delta z_2\\ \delta_2\end{pmatrix} = \begin{pmatrix}1 & 0\\ \mathrm{M}_{65} & \mathrm{M}_{66}\end{pmatrix}\begin{pmatrix}\Delta z_1\\ \delta_1\end{pmatrix} = \begin{pmatrix}1 & 0\\ -eV\omega/\gamma\beta^3 mc^3 & 1\end{pmatrix}\begin{pmatrix}\Delta z_1\\ \delta_1\end{pmatrix}. \tag{94}$$

From the definition of M_{56}, the offset length of a particle with fractional momentum deviation δ going through the drift is:

$$\Delta z_3 = \Delta z_2 + \frac{L}{\gamma^2}\delta_2, \tag{95}$$

and the corresponding matrix equation is

$$\begin{pmatrix} \Delta z_3 \\ \delta_3 \end{pmatrix} = \begin{pmatrix} 1 & \mathrm{M}_{56} \\ 0 & 1 \end{pmatrix} \begin{pmatrix} \Delta z_2 \\ \delta_2 \end{pmatrix} = \begin{pmatrix} 1 & L/\gamma^2 \\ 0 & 1 \end{pmatrix} \begin{pmatrix} \Delta z_2 \\ \delta_2 \end{pmatrix}. \tag{96}$$

Here, e is the particle charge, γ and β are the usual relativistic parameters. The combined matrix of the buncher cavity followed by a drift length L is

$$\mathbf{M} = \begin{pmatrix} 1 + \mathrm{M}_{65}\mathrm{M}_{56} & \mathrm{M}_{56}\mathrm{M}_{66} \\ \mathrm{M}_{65} & \mathrm{M}_{66} \end{pmatrix} = \begin{pmatrix} 1 - eV\omega L/\gamma^3\beta^3 mc^3 & L/\gamma^2 \\ -eV\omega/\gamma\beta^3 mc^3 & 1 \end{pmatrix}. \tag{97}$$

The particle's longitudinal position and energy at the end of the drift are given in terms of its initial values:

$$z_3 = \left(1 - \mathrm{M}_{56}\frac{eV\omega}{\gamma\beta^3 mc^3}\right) z_1 + M_{56}\delta_1; \quad \delta_3 = \delta_1 - \frac{eV\omega}{\gamma\beta^3 mc^3} z_1; \quad \text{with} \quad \mathrm{M}_{56} = \frac{L}{\gamma^2}. \tag{98}$$

For the full compression [58], $1 + \mathrm{M}_{65}\mathrm{M}_{56} = 0$, which gives the buncher voltage as:

$$V_{bun} = \frac{mc^3\gamma^3\beta^3}{e\omega L} = \frac{\lambda_{RF} mc^2\gamma^3\beta^3}{2\pi e L}. \tag{99}$$

Here Lorentz factor γ corresponds to the energy at which the bunching takes place and $\lambda_{RF} = c/f_{RF}$ is the RF wavelength. Assuming that the incoming beam distribution has no energy-position correlation $\langle\delta_1\Delta z_1\rangle = 0$, then the final *rms* bunch length is

$$\sigma_{z_3} = \sqrt{\langle z_3^2\rangle} = \mathrm{M}_{56}\sigma_{\delta_1} = \frac{L}{\gamma^2}\sigma_{\delta_1}. \tag{100}$$

Since $\delta = \Delta p/p = 1/\beta^2 . \Delta\mathcal{E}/\mathcal{E} = \delta_{\mathcal{E}}/\beta^2$, the Eq. (100) for the final *rms* bunch length can be written as in terms of energy spread as:

$$\sigma_{z_3} = \sqrt{\langle z_3^2\rangle} = \frac{L}{\gamma^2\beta^2}\sigma_{\delta\mathcal{E}_1}. \tag{101}$$

CHAPTER 4

SPACE CHARGE EFFECT FOR LOW ENERGY BEAM

The previous chapter (Chapter 3) discusses how charged particles moving in an accelerator interact with the external electromagnetic fields. The external forces **F** used for the beam transport and expressed by Eq. (7b) do not depend on the beam current. In a real accelerator, however, there is another important source of electromagnetic fields to be considered, the beam itself, which, circulating inside the pipe, produces additional electromagnetic fields called "self-fields". These fields, which depend on the intensity of the beam current and on the charge distribution, perturb the external guiding fields.

The self-fields are responsible for several unwanted phenomena related to beam dynamics, such as energy loss, a shift in the synchronous phase and frequency, changes in betatron frequencies, and instabilities. The study of self-fields is conventionally divided into two categories: space charge fields and wakefields. Space charge forces are generated directly by the charge distribution, incorporating image charges and currents resulting from the beam's interaction with a perfectly conducting smooth pipe [59]. On the other hand, wakefields are produced due to the finite conductivity of the walls and any geometric variations in the beam pipe, such as resonant devices and transitions of the beam pipe [60]. The impact of the self-field created by the beam alone is referred to as 'direct' space-charge tune shifts and spreads. In a real accelerator, however, the system includes a vacuum pipe, accelerator gaps, magnets, beam diagnostics, and a high-intensity beam. This high-intensity beam induces surface charges or currents into this environment, which then exert an influence on the beam, potentially leading to an 'indirect' space-charge tune shift. The detailed discussion can be found in the Refs. [26, 59].

This chapter describes fundamental concepts related to space charges, including transverse and longitudinal direct space charge forces and their impact on beam envelope, beam sizes, and bunch lengths.

4.1 SPACE CHARGE FORCES

Space charge fields are among the factors influenced by the beam current and charge distribution. These fields encompass Coulomb repulsive forces within the charge distribution, and they can perturb the external fields responsible for guiding the beam through the accelerator. The smoothed space-charge forces acting on a particle can be treated as an external force, which can be further divided into linear and nonlinear components based on the displacement from the beam axis. The linear space-charge term typically causes beam defocusing and leads to an increase in beam size, while the nonlinear space-charge term distorts the phase-space distribution, leading to an increase in *rms* emittance.

4.1.1 TRANSVERSE DIRECT SPACE CHARGE FORCE

In electron injectors, especially when the particle energy is relatively low and particle density is moderate, the primary influence arises from the average Coulomb forces resulting from the beam's charge distribution. This phenomenon is known as the space charge effect. To assess the impact of the space charge effect, we can compute the radial force acting on an electron within a cylindrically symmetric beam featuring either a uniform or Gaussian charge distribution, as outlined in references [26, 59].

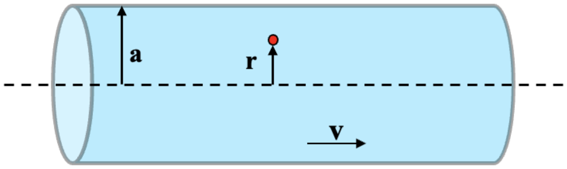

FIG. 22. Uniform cylindrical charge distribution with radius a, moving with velocity $v = \beta c$.

Consider a beam with a uniform cylinder of radius a so that the longitudinal charge distribution (charge per unit of length) $\lambda(r) = \lambda_0 \ (r/a)^2$, moves with constant velocity $v = \beta c$ as shown in Fig. 22. It has a total current of $I = \beta c \lambda(r)$. The electric and magnetic fields due to the charge distributions can be computed [26, 59]. Applying Gauss's law,

$$E_r(2\pi r)\Delta z = \frac{\lambda(r)}{\varepsilon_0}\Delta z \ \Rightarrow E_r = \frac{\lambda(r)}{2\pi\varepsilon_0 r}. \tag{102}$$

Here ε_0 denotes the vacuum permitivity. Applying Ampere's law

$$B_\phi(2\pi r) = \mu_0 I = \mu_0 \beta c \lambda(r) \;\Rightarrow B_\phi = \frac{\lambda(r)}{2\pi\varepsilon_0} = \frac{\beta\lambda(r)}{2\pi\varepsilon_0 c r} = \frac{\beta}{c}E_r, \tag{103}$$

where $c^2 = 1/\varepsilon_0\mu_0$, and μ_0 is the permeability of free space. Thus, the electromagnetic transverse force acting on a charge inside the beam is given by the Lorentz force.

$$F_r(r,z) = e(E_r - vB_\phi) = e(1-\beta^2)E_r, \tag{104a}$$

$$F_r(r,z) = \begin{cases} \dfrac{e\lambda_0}{2\pi\varepsilon_0\gamma^2 a^2}r = \dfrac{eI}{2\pi\varepsilon_0\beta c\gamma^2 a^2}r & (r \le a), \\ \dfrac{e\lambda_0}{2\pi\varepsilon_0\gamma^2 r} = \dfrac{eI}{2\pi\varepsilon_0\beta c\gamma^2 r} & (r > a). \end{cases} \tag{104b}$$

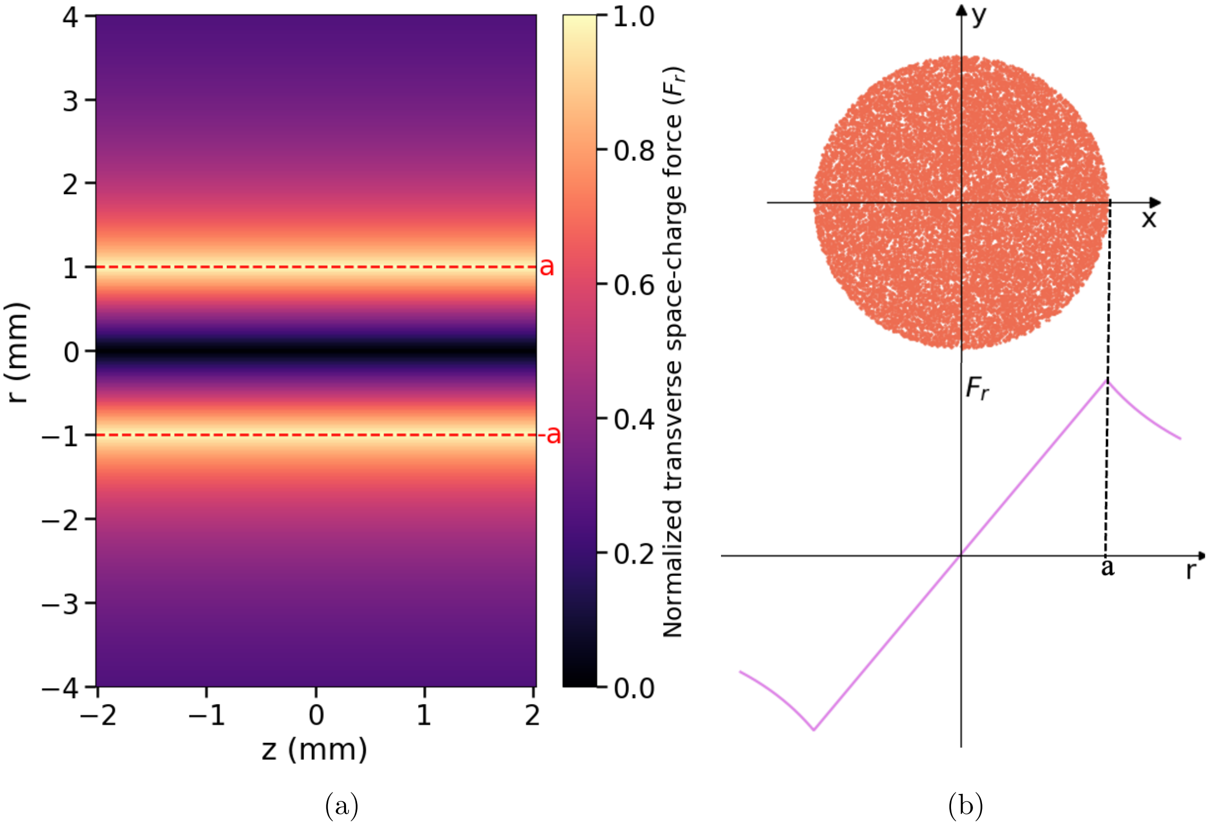

(a) (b)

FIG. 23. Transverse space charge force for uniform beam distribution. (a) 2D distribution of space-charge force in the r-z plane, (b) 1D distribution of space-charge force with beam transverse coordinates.

The transverse or radial space charge force causes defocusing in both planes. For highly relativistic particles with substantial energy, this force is negligible. The force is zero when $\beta = 1$. However, for non-relativistic particles, particularly low-energy beams near the cathode, the beam rapidly spreads due to this defocusing effect. It is worth noting that this transverse space charge force is inversely proportional to the bunch dimensions. Figure 23 illustrates the distribution of the transverse space charge force in accordance with Eq. (104b).

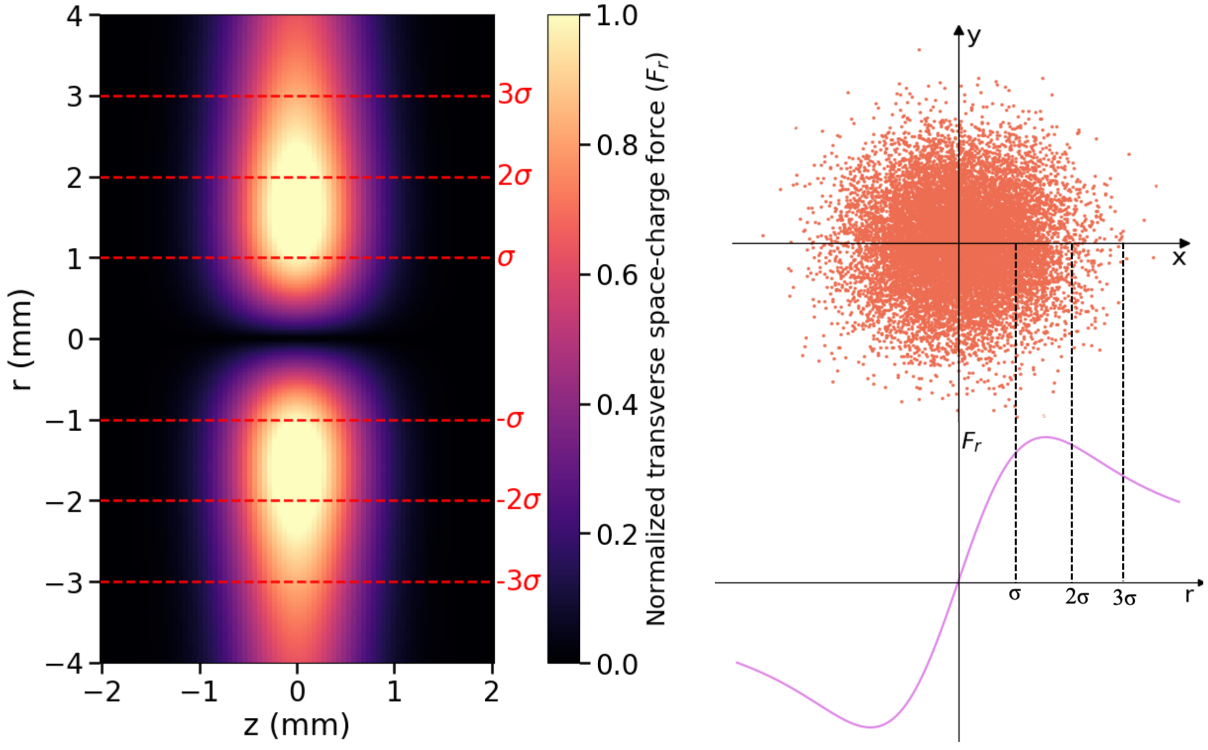

(a)

(b)

FIG. 24. Beam with a Gaussian beam distribution. (a) 2D distribution of space-charge force in the r-z plane, (b) 1D distribution of space-charge force with beam transverse coordinates.

For a Gaussian distribution, such as:

$$\rho(r,z) = \frac{Q}{(2\pi)^{3/2}\sigma_z\sigma_r^2}\exp\left(-\frac{z^2}{2\sigma_z^2}\right)\exp\left(-\frac{r^2}{2\sigma_r^2}\right), \tag{105}$$

the space-charge force or self field force in radial direction is then

$$\begin{aligned} F_r(r,z) &= \frac{e}{2\pi\varepsilon_0\gamma^2}\frac{Q}{\sqrt{2\pi}\sigma_z}\exp\left(-\frac{z^2}{2\sigma_z^2}\right)\left[\frac{1-\exp\left(-\frac{r^2}{2\sigma_r^2}\right)}{r}\right] \\ &\approx \frac{e}{4\pi\varepsilon_0\sigma_r^2\gamma^2}\frac{Q}{\sqrt{2\pi}\sigma_z}\exp\left(-\frac{z^2}{2\sigma_z^2}\right)r, \quad \text{for} \quad r \ll \sigma_r, \end{aligned} \tag{106}$$

where Q is the bunch charge, σ_r and σ_z are the *rms* beam size in the transverse and longitudinal directions, respectively. Figure 24 illustrates the distribution of the transverse space charge force in accordance with Eq. (106).

It is evident that the radial space charge force diminishes as γ^2 increases. Consequently, in proximity to the cathode and the low-energy (keV) beam region of the injector, the space charge effect is more pronounced than after the accelerating RF cavity and at medium energy (a few MeV). Additionally, for an intense beam with small transverse dimensions, the nonlinear space charge force can exert a significant influence during the acceleration from low to higher energy and during the long drift, potentially leading to emittance growth.

4.1.2 LONGITUDINAL DIRECT SPACE CHARGE FORCE

The longitudinal electric field, responsible for the longitudinal forces, can be derived based on the understanding of the transverse fields. The transverse electric field within the beam ($r \leq a$) can be expressed using the first equation of Eq. (104b). However, this expression can be extended to encompass non-uniform longitudinal distributions $\lambda(z)$. Outside the beam ($r \geq a$), the longitudinal electric field due to space charge is given by:

$$E_z(r,z) = -\frac{1}{\gamma^2}\frac{\partial}{\partial z}\int_r^b E_r(r,z)\,dr. \tag{107}$$

For a uniform transverse distribution, which however can be generalized by considering a non uniform longitudinal distribution $\lambda(z)$, the longitudinal force is given by [26]:

$$\begin{aligned} F_z(r,z) = eE_z(r,z) &= -\frac{e}{\gamma^2}\frac{\partial}{\partial z}\int_0^b E_r(r,z)\,dr \\ &= -\frac{e}{2\pi\varepsilon_0\gamma^2}\left(\int_r^a \frac{r'}{a^2}\,dr' + \int_a^b \frac{1}{r'}\,dr'\right)\frac{\partial\lambda(z)}{\partial z} \\ &= -\frac{e}{4\pi\varepsilon_0\gamma^2}\left(1-\frac{r^2}{a^2}+2\ln\frac{b}{a}\right)\frac{\partial\lambda(z)}{\partial z}. \end{aligned} \tag{108}$$

Therefore, the longitudinal force acting on a charge is positive (negative) in the region with negative (positive) density slope. For a Gaussian beam distribution in both planes:

$$F_z(r,z) = eE_z(r,z) = -\frac{e}{2\pi\varepsilon_0\gamma^2}\frac{Q}{\sqrt{2\pi}\sigma_z}\left(\frac{\partial}{\partial z}\exp\left(-\frac{z^2}{2\sigma_z^2}\right)\right)\int_r^b\left[\frac{1-\exp\left(-\frac{r'^2}{2\sigma_r^2}\right)}{r'}\right]\,dr'. \tag{109}$$

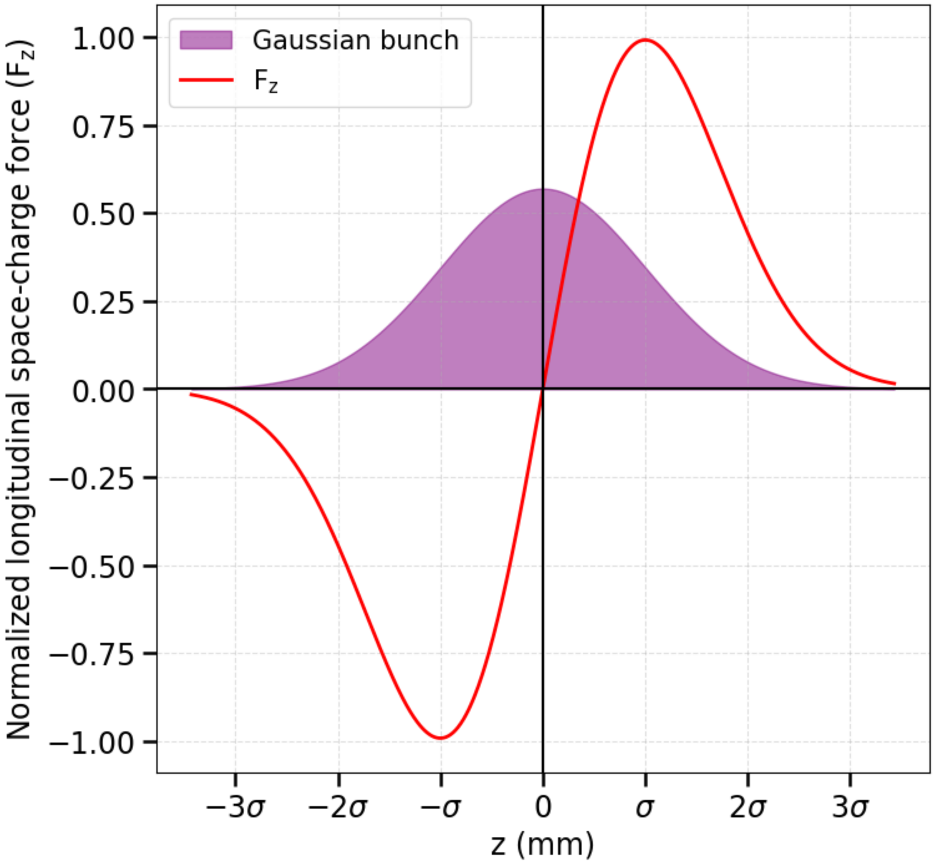

FIG. 25. Longitudinal space charge force for Gaussian beam distribution.

The longitudinal space charge forces modify the synchrotron frequency, which is particularly important near transitions in storage rings. They also cause bunch lengthening in low-energy electron beams in the injector (linac). An initial observation is the highly nonlinear nature of space charge forces. Another important observation is that the radial force is directly proportional to the longitudinal density, while the longitudinal force is proportional to the derivative of the longitudinal density. When linearizing longitudinal forces (applicable for very small amplitudes where $r \ll \sigma_r$ and $z \ll \sigma_z$), it results in the following expression [61]:

$$\begin{aligned} F_z(r,z) &\approx \frac{e}{2\pi\varepsilon_0\gamma^2}\frac{Q}{\sqrt{2\pi}\sigma_z}\left(\frac{-2z}{2\sigma_z^2}\right)\left(\frac{a^2}{4\sigma_r^2}+\ln\frac{b}{a}\right) \\ &= \frac{e}{4\pi\varepsilon_0\gamma^2}\frac{Q}{\sqrt{2\pi}\sigma_z^3}\left(1+2\ln\frac{b}{a}\right)z = \frac{eg}{4\pi\varepsilon_0\gamma^2}\frac{Q}{\sqrt{2\pi}\sigma_z^3}z. \end{aligned} \tag{110}$$

where $a = \sqrt{2}\sigma_r$ and $g = (1 + 2\ln b/a)$. The normalized longitudinal force due to space charge for the Gaussian distribution is depicted in Fig. 25. Similarly to the transverse space charge forces, the longitudinal space charge force is maximum at a low energy and diminishes at high energy.

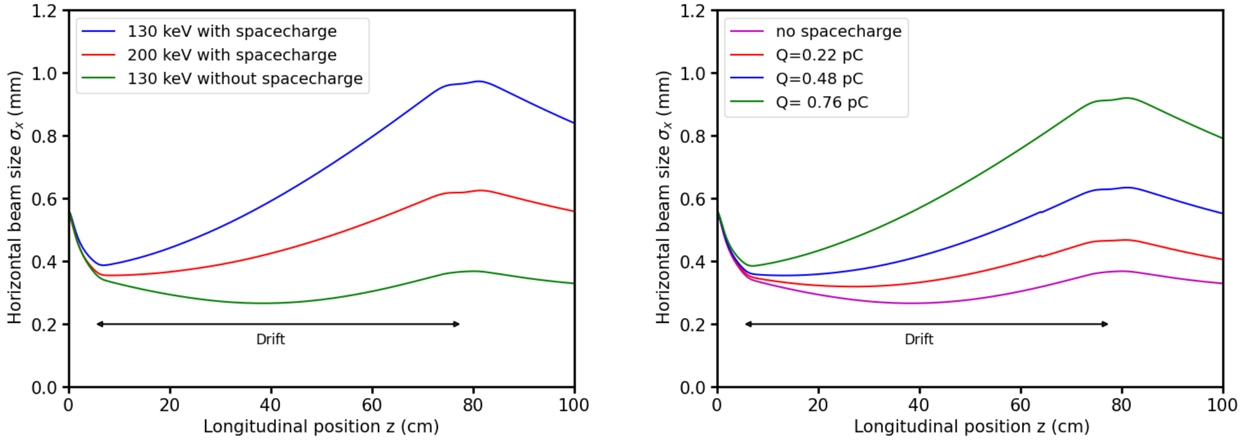

(a) (b)

FIG. 26. Transverse size of electron beam expansion due to space charge forces. (a) Simulation results showing the horizontal *rms* beam sizes as a function of distance from the photocathode for different beam energies, considering a bunch charge of 0.64 pC in the CEBAF injector, (b) Simulation results illustrating the horizontal *rms* beam sizes as a function of distance from the photocathode for various bunch charges at a beam energy of 130 keV.

The space charge forces, both transverse and longitudinal, demonstrate linearity for small amplitudes and defocusing. In this thesis, the General Particle Tracer (GPT) is employed for simulating space charge effects. The simulated results illustrating the increase in transverse *rms* beam sizes and the *rms* bunch length as functions of the distance from the photocathode due to space charge forces are presented in Figs. 26 and 27, respectively.

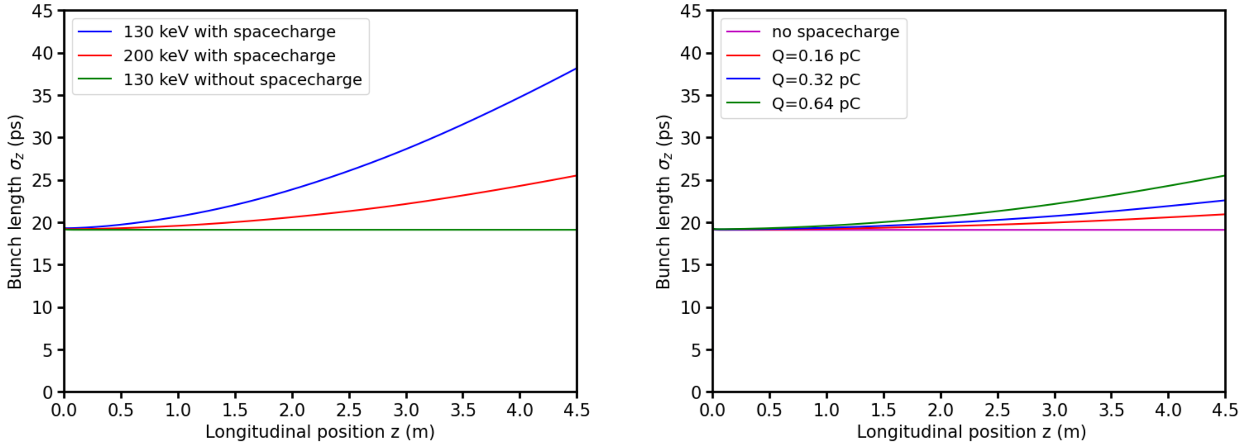

(a) (b)

FIG. 27. Electron bunch length expansion due to space charge. (a) Simulation results displaying the *rms* bunch length as a function of distance from the photocathode for different beam energies, considering a bunch charge of 0.64 pC in the CEBAF Injector. (b) Simulation results showing the *rms* bunch length as a function of distance from the photocathode for various bunch charges at a beam energy of 200 keV.

4.2 DIRECT SPACE CHARGE EFFECTS IN A LINAC

In a Linac (injector) or a beam transport line, direct space charge effects can result in significant longitudinal-transverse correlations of the bunch parameters. This, in turn, may lead to a mismatch with the focusing and accelerating devices, contributing to emittance growth and energy spread. Matching conditions that are suitable for preserving beam quality can be derived from a simple model, as demonstrated hereafter. For a more in-depth discussion can be found in the Refs. [45, 62].

Examine a bunched beam with an initially uniform charge distribution in a cylinder with a radius of R and a length of l_b. This beam carries a current I and moves with a longitudinal velocity $v = \beta c$. The linear components of the longitudinal and transverse space charge fields are provided in [63] as follows:

$$E_r(r,\zeta) = \frac{Ir}{2\pi\varepsilon_0 R^2 \beta c} g(\zeta); \quad E_z(\zeta) = \frac{IL}{2\pi\varepsilon_0 R^2 \beta c} h(\zeta), \tag{111}$$

where the field form factors are described by the functions:

$$h(\zeta) = \sqrt{A + (1-\zeta)^2} - \sqrt{A + \zeta^2} + (2\zeta - 1), \tag{112a}$$

$$g(\zeta) = \frac{(1-\zeta)}{2\sqrt{A^2 + (1-\zeta)^2}} + \frac{\zeta}{2\sqrt{A^2 + \zeta^2}}, \tag{112b}$$

where $\zeta = z/L$ is the normalized longitudinal coordinate along the bunch and $A = R/\gamma L$ is the beam aspect ratio. As γ increases $g(\zeta) \to 1$ and $h(\zeta) \to 0$. Consequently, direct space charge fields primarily influence the transverse beam dynamics.

The transverse beam dynamics of a beam, taking into account the space charge effect and characterized by an *rms* envelope σ and transverse normalized thermal *rms* emittance $\epsilon_{n,th}$ at the source, can be conveniently described. Under the paraxial ray approximation, the *rms* envelope equation for an axisymmetric beam is given as [45]:

$$\sigma'' + \frac{\gamma'}{\gamma}\sigma' + k_{ext}^2 \sigma = \frac{K_{sc}}{\gamma^3 \sigma} + \frac{\epsilon_{n,th}^2}{\gamma^2 \sigma^3}. \tag{113}$$

Here, the first term represents the change in the envelope slope, the second term drives envelope oscillation damping due to acceleration, the third term accounts for linear external focusing forces, the fourth term represents the defocusing effects caused by space charge, and the fifth term deals with the internal pressure due to emittance. In this equation, $K_{sc} = I_{peak}/I_A$ is the beam perveance, I_{peak} stands for the peak current, I_A represents the Alfvén current ($I_A = 4\pi\epsilon_0 mc^3/e \sim 17\,\mathrm{kA}$), and $\gamma' = eE_{acc}/mc^2$, where E_{acc} is the accelerating field.

Based on the envelope equation Eq. (113), we can distinguish between two regimes of beam propagation: space charge-dominated and emittance-dominated. A beam is considered to be space charge-dominated when the collective forces generated by space charge significantly outweigh the influence of emittance pressure. The relative significance of space charge effects versus emittance pressure is quantified by the laminarity parameter, which is defined as the ratio between the space charge term and the emittance term:

$$\rho = \frac{I_{peak}\sigma^2}{2I_A\gamma\epsilon_{n,th}^2}. \tag{114}$$

When ρ greatly exceeds unity, the beam behaves like a laminar flow, where all beam particles move on trajectories that do not intersect. In this regime, successful transport and acceleration require precise tuning of focusing and accelerating elements to maintain laminarity. Correlated emittance growth is typical in this regime but can be conveniently reversed if proper beam matching conditions are met. When $\rho < 1$, the beam is emittance-dominated (also referred to as the thermal regime, corresponding to a Debye length significantly larger than the bunch envelope), and space charge effects can be neglected. The transition to the thermal regime occurs at $\rho \simeq 1$, which corresponds to the transition energy:

$$\gamma_{tr} = \frac{I_{peak}\sigma^2}{2I_A\epsilon_{n,th}^2}. \tag{115}$$

For example, consider a beam with I_{peak}= 200 mA, ϵ_n=1 µm, and σ= 0.55 mm. This beam is transitioning from the space charge-dominated regime to the thermal regime at an energy level of 910 keV. This example illustrates that the space charge-dominated regime is typically associated with low-energy beams. However, in applications such as linac-driven free electron lasers, high-density beams with peak currents exceeding kA are essential. Even if the bunch energy surpasses the γ_{tr} threshold, space charge effects may reoccur if bunch compressors are active, leading to an increase in I_{peak}. Therefore, one must consider a new transition energy level associated with higher I_{peak}.

CHAPTER 5

ELECTRON BEAM CHARACTERIZATION: SIMULATIONS AND MEASUREMENTS

The Jefferson Lab CEBAF is uniquely equipped with the capability to deliver polarized electron beams of varying specifications to four separate experiment halls simultaneously. Different experiments that will run concurrently with the K_L experiment in different experimental halls have distinct average beam currents, repetition rates, and charge per bunch. However, for CEBAF operations, it is necessary to transmit both high and low-charge beams for different drive frequencies of the laser, each with different specifications, simultaneously through the injector using the same injector optics. To meet the diverse beam requirements of the different halls, computer modeling is utilized to derive suitable settings for magnetic elements (solenoids and quads) and gradient amplitude and phases of the RF systems. These settings are critical in ensuring the effective transmission of both low and high-charge beams through the injector and ensuring the desired beam characteristics out of the injector sections within the limits of the CEBAF injector operations. Beam characteristics include bunch lengths, energy spread, total energy, horizontal and vertical beam sizes, normalized transverse emittances, and beam transmission along the injector beamline. After performing computer modeling and simulations, measurements under the same conditions as the simulations help validate the simulations against the actual measurements.

The beamline modeling and simulations of the CEBAF injector, spanning from the gun to the upstream of the first full cryomodules 30.0 m downstream of the gun, were performed using General Particle Tracer (GPT) [64]. The beamline was modeled separately using the GPT program. These simulations were executed to investigate the evolution and transmission of beams with varying charge per bunch within the CEBAF injector. Beam characteristics were analyzed across a broad spectrum of charge values to support the simultaneous operation of CEBAF's four experimental Halls.

Initially, beam dynamics simulations and a beam study were conducted for the preexisting CEBAF Phase 1 injector upgrade at a DC gun voltage of 130 kV. Subsequently, optimization and simulations were carried out to determine the magnetic elements and RF settings for the existing CEBAF Phase 2 injector at a gun voltage of 200 kV. During the

Scheduled Accelerator Down (SAD) in 2023, the DC gun voltage was set to 180 kV for operation. Later, due to gun tripping, it dropped to 140 kV for the final measurements reported in this thesis. As a result, beam studies were performed at DC gun voltages of 130 kV, 140 kV, and 180 kV. All measurements at these gun voltages utilized the JLab ops accelerator account and OPS desktop, making use of available Experimental Physics and Industrial Control System (EPICS) tools. Data were collected and recorded in JELI (Jefferson Lab Electronic Logbook Interface) and saved on the Acceleration Operations (OPS) desktop. Afterwards, the results obtained from both measurements and simulations were processed using Gnuplot and Python.

The values of the beam energy or corresponding Lorentz factor and the bunch charge are crucial factors for beam transmission and beam characteristics in the low-energy sections of the injector. The gun voltage, corresponding kinetic energy, total energy, relativistic momentum, and relativistic factors β and γ for the simulations and measurements conducted, which are discussed in this thesis, are tabulated in Table 2.

TABLE 2. CEBAF injector DC gun voltage and corresponding beam parameters.

Gun Voltage (kV)	$\beta = \frac{v}{c}$	$\gamma = \frac{1}{\sqrt{1-\beta^2}}$	E=γmc^2 (MeV)	p =$\gamma\beta mc$ (MeV/c)	K.E = $(\gamma-1)mc^2$ MeV
130	0.6037	1.2544	0.641	0.3869	0.130
140	0.6196	1.2740	0.651	0.4034	0.140
180	0.6731	1.3522	0.691	0.4652	0.180
200	0.6953	1.3914	0.711	0.4944	0.200

In the upcoming sections, simulations and measurements from beam experiments will be presented, encompassing various beam currents and bunch charge specifications in the CEBAF injector across different gun voltages. Subsequently, the key findings of this research will be presented. The organizational structure of the results is as follows: the simulation and measurement results at 130 kV DC gun voltage will be presented first, followed by the measurements, optimizations and simulations conducted at 180 kV DC gun voltage. The final set of measurements will be presented at 140 kV DC gun voltage. Finally, discussions about injector optimizations and simulations at 200 kV DC gun voltage will be undertaken.

5.1 GPT MODELING OF THE CEBAF INJECTOR

The three-dimensional (3D) space charge code GPT played a crucial role in this work. GPT employs two 3D space charge solvers, specifically *spacecharge3Dmesh* and *spacecharge3D*, to model space charge effects. The mesh version, utilizing GPT's mean-field space charge algorithm, employs a non-equidistant 3D multigrid Poisson solver [65, 66] to calculate the mean-field interaction of the entire bunch, including image charge effects. On the other hand, the *spacecharge3D* routine is a particle-particle solver [67] that uses fully relativistic field equations without approximations, although it requires a substantial amount of CPU time compared to the meshed approach. Furthermore, GPT enables users to define custom optical elements and position and overlay electromagnetic field maps in 3D space. These features offer the necessary versatility to accurately model the CEBAF injector, where the fields of multiple elements overlap.

The GPT model spans from the gun to the entrance of the first full cryomodules in the linac section of the injector, encompassing detailed element models. This model addresses both longitudinal and transverse beam dynamics, covering the quarter cryomodules (QCM) in the 130 kV Phase 1 CEBAF injector upgrade and the booster for the Phase 2 CEBAF injector upgrade. It ensures that the longitudinal and transverse beam dynamics are appropriate at the entrance of the injector linac section. Comprehensive discussions on GPT injector modeling for different phases of the CEBAF injector with varying gun voltages can be found in the references [68], [42], and [69], as well as in the following subsections.

5.2 CEBAF INJECTOR AT 130 kV DC GUN VOLTAGE

The beamline layout for the Phase 1 CEBAF inejector upgrade is explained in Chapter 2 and detailed in Table 3. The gun starts at 0.2 m and extends the beamline 30.0 m downstream, upstream of the first full cryomodules. There are 11 solenoids, namely MFXs (MFX2I01, MFX1I03, MFX0I01), spin solenoids MFGs (MFG1I04A and MFG1I04B), and MFDs (MFD0I04A and MFD0I04B), MFAs (MFA0I03, MFA0I05, MFA0I06), and MFL0I07, starting from the gun to just before the QCM. These solenoids are used for beam focusing

TABLE 3. Locations of the beamline elements for the Phase 1 CEBAF injector upgrade at 130 kV gun voltage. Here, MDR represents the dipole magnet, MFs denote the solenoids, MQs stand for the quadrupole magnets. VWien and HWien refer to the vertical and horizontal Wien filters.

Location of Beam Line Elements			
Elements	Positions (m)	Elements	Positions (m)
MFX2I01	0.780796	MFA0I05	8.42042
MDR1I02	1.717802	Buncher	8.88413
MFX1I03	2.261358	MFA0I06	9.14772
MQW1I03	2.636135	Capture	9.953398
VWien	2.911598	A3	10.61717
MQW1I04	3.187061	MFL0I07	10.70130
MFG1I04A	3.573776	first 5-cell	12.42626
MFG1I04B	3.816954	second 5-cell	13.18493
MQW1I05	4.114669	MQS0L01	14.76567
HWien	4.390132	MQJ0L01	14.9641
MQW1I06	4.665595	MQS0L01A	16.95193
Prebuncher	4.823223	MQJ0L02	18.0041
MFX0I01	5.515352	MQS0L02	18.33187
Pcup	5.801864	MQJ0L02A	18.6143
A1	5.938770	MQS0L02B	21.7726
A2	6.616446	MQJ0L03A	23.80147
MFA0I03	6.813255	MQS0L03	24.1523
MFD0I04A	7.514275	MQJ0L03	24.43177
Chopper	7.60	MQS0L04	27.3836
MFD0I04B	7.685725	MQJ0L04	27.585

in the keV beam energy region of the CEBAF injector. After the QCM, the beam is focused using quadrupole magnets. There are 12 quadrupoles and skew quadrupoles after the QCM, extending from the QCM to about 28.0 m downstream from the gun.

In simulations conducted for the 130 kV DC gun voltage, we followed the previously optimized settings [70] of the magnetic elements and RF systems. Employing these settings, we systematically varied the initial beam sizes, pulse lengths, and charges per bunch across a spectrum ranging from low to high charge (representative of a space charge-dominated beam), corresponding to the $\mathrm{K_L}$ bunch charge.

The previously modeled and developed 2D, and 3D field maps were utilized in the simulation for most of the beamline elements at specific locations in the CEBAF injector. The longitudinal electric field of the 3D electric field map of the DC gun is depicted in Fig. 28(a). The longitudinal magnetic fields of the 2D and 3D magnetic field maps for the focusing and spin-flipping solenoids are shown in Fig. 28(b), Fig. 28(c), Fig. 28(d), Fig. 28(f), and Fig. 28(e). The MFGs spin-flipping solenoid between the Wien system is single-wound to provide spin manipulations, as shown in Fig. 28(c), and the rest of the focusing solenoids are counter-wound. In the plots (Fig. 28, Fig. 29, Fig. 51, and Fig. 52), the thickness indicates a minor fluctuation in the longitudinal electric and magnetic fields relative to the transverse coordinates (x, y), while the longitudinal coordinates (z) remain constant.

Different types of field maps are utilized for both warm RF cavities (prebuncher, buncher, capture) and SRF cavities (5-cell cavities) in the beam dynamics simulation. The prebuncher field map is a 3D rectangular field map representing a standing electromagnetic wave pattern. It incorporates modifications on *Map3D_TM*, referred to as *Map3D_TM_scope*, which includes a drift in the field map; this version specifies the map element to be LOCAL. The buncher field map is also a 3D rectangular field map, depicting an oscillating electric field, with modifications on *Map3D_Ecomplex* and *map3D_Hcomplex* known as *Map3D_Ecomplex_scope* and *Map3D_Hcomplex_scope*. Similarly, *Map25D_TM_scope* reads a 2.5D cylindrical symmetric field map of a cavity in TM-mode and is used for the capture cavity. *Map3D_TMparmela_scope*, a modification of the original *Map3D_TM* (a 3D rectangular field map for a standing electromagnetic wave pattern), removes any field component that might generate transverse kicks and is used for two 5-cell SRF cavities. These field maps are described in the GPT user manual [67]. The longitudinal electric fields of the 2D and 3D electric filed maps of the RF systems (prebuncher, buncher, capture, and 5-cell SRF cavities) is illustrated in Fig. 29.

The field maps, converted to the General Datafile Format (GDF), are employed in the GPT kernel for simulations. Additionally, each element along the injector beamline contains a *xymax* or *rmax* statement, which is configured to eliminate particles from the simulation if they move beyond the defined space of the field map. The specific values for *rmax* and

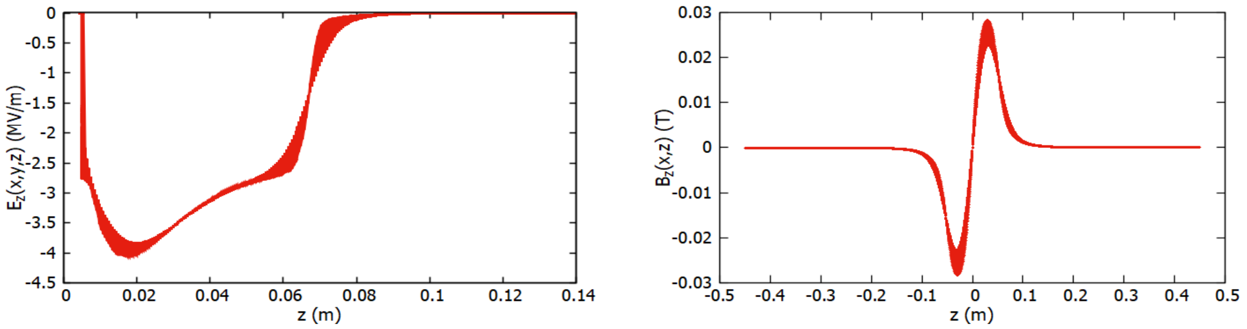

(a) Longitudinal electric field in the DC gun.

(b) Longitudinal magnetic field in the MFXs.

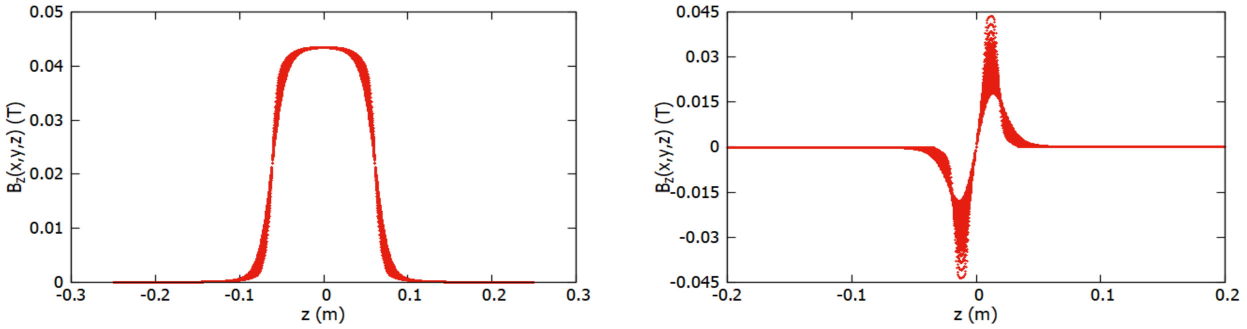

(c) Longitudinal magnetic field in the MFGs.

(d) Longitudinal magnetic field in the MFAs.

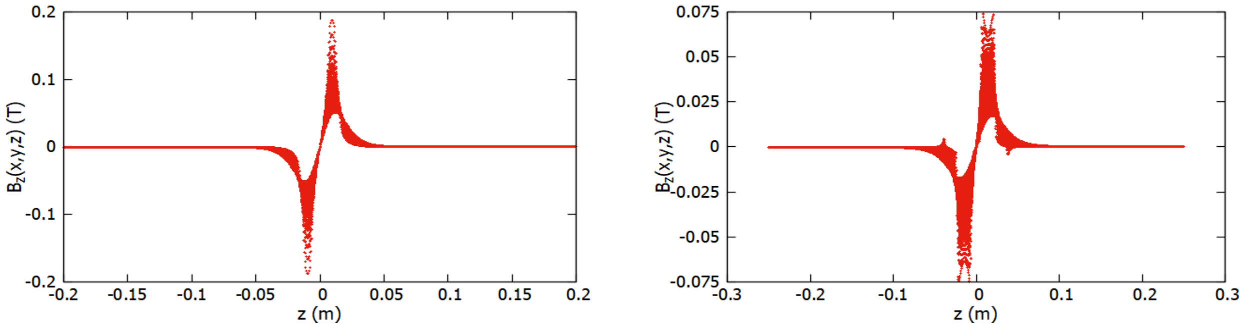

(e) Longitudinal magnetic field in the MFL.

(f) Longitudinal magnetic field in the MFDs.

FIG. 28. Longitudinal electric and magnetic fields for: (a) 3D field map of the high-voltage DC gun, where the transverse coordinates vary from 0 to ±6 mm, (b) 2D field map of counter-wound focusing solenoids (MFXs) after the DC gun, where the transverse coordinate varies from 0 to 22 mm, (c) 3D field map of single-wound spin-flipping solenoids MFGs in between the Wien system, (d) 3D field map of the solenoids MFAs before and after the chopper and after the buncher, (e) 3D field map of the solenoid MFL after the capture. In these field maps, the transverse coordinates vary from 0 to ±12 mm, and (f) 3D field map of the solenoids MFDs in between the choppers, where the transverse coordinates vary from 0 to ±22 mm.

xymax are determined based on the locations of the beamline elements.

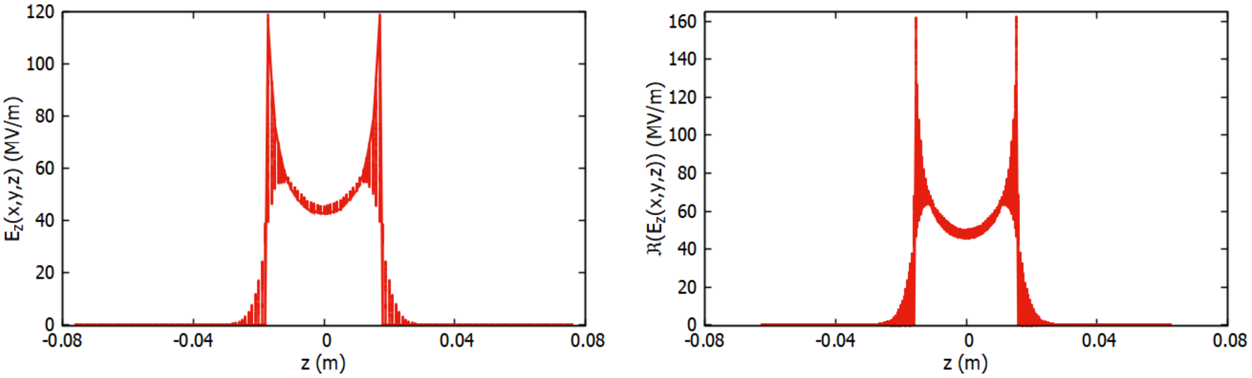

(a) Longitudinal electric field in prebuncher cavity. (b) Longitudinal electric field in the buncher cavity.

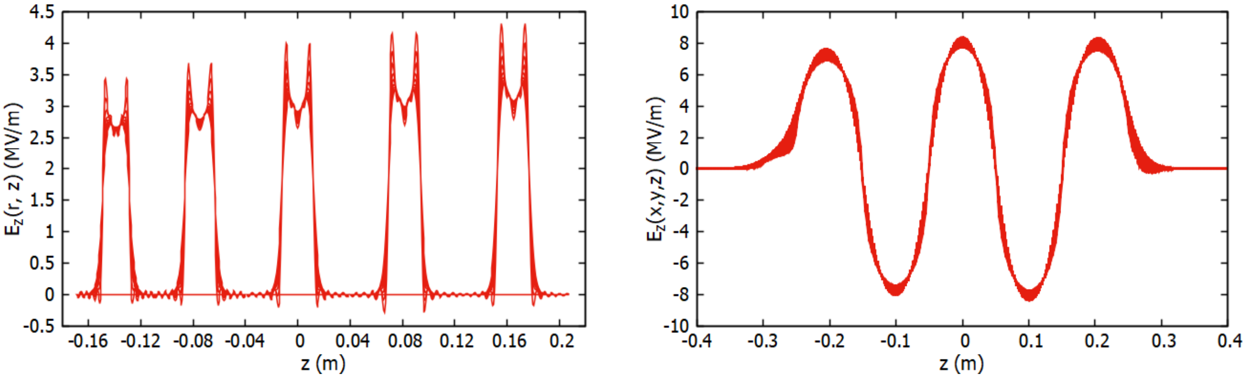

(c) Longitudinal electric field in the capture cavity. (d) Longitudinal electric field in the 5-cell cavity.

FIG. 29. Longitudinal electric field for 2.5D and 3D electric field maps of warm and cold SRF cavities at 130 kV gun voltage.(a) 3D field map of the prebuncher cavity, (b) 3D field map of the buncher cavity. In these cavity field maps, the transverse coordinates vary from 0 to ±6 mm. (c) 2.5D field map of the capture cavity, in which radial coordinates vary from 0 to 6 mm, and (d) 3D field map of the 5-cell SRF cavity, in which transverse coordinates vary from 0 to ±20 mm.

In the simulation, the beam, initiated from a 130 keV photocathode, traverses the injector elements along a 30.0 m downstream beamline, including the prebuncher cavity, buncher cavity, capture section, QCM, focusing solenoids, and quadrupoles. Strategically placed steering magnets (correctors) between the gun and the first solenoid are used to center the beam on-axis and compensate for the gun's kick. Particle distributions, defining the electron bunch from the photocathode, are generated using the GPT suite. Calculations reveal a negligible impact ($< 0.01\%$ increase) of dipole magnets on bunch length due to the beam's low energy spread. The M_{56} of a short bend magnet is small, reducing the influence of the bending magnet, and hence it is excluded from the simulation. RF choppers are not included because their impact effectively "cancels out" upon the beam's return to the axis. The straight beamline model, excluding choppers, is used, and Wiens are turned OFF as the K_L experiment does not require spin manipulation.

For the particle distribution at the cathode in the simulation, the beam is assumed to have a Gaussian distribution in t, x, y, p_x, and p_y, following the profile of the laser. Initially, at the cathode, the transverse beam sizes are $4\sigma_x$ =2.237 mm and $4\sigma_y$ =2.093 mm, with a laser pulse length (FWHM) of 45 ps. The energy spread at the cathode is $\sigma_{\beta\gamma} = 2.45 \times 10^{-4}$. The longitudinal and transverse beam distributions at the cathode are shown in Fig. 30. The beam current varies from 5 µA to 160 µA, and the corresponding bunch charges at 249.5 MHz laser frequency are calculated using the relation: $Q = I/f$. For high bunch charge, the space charge effect is incorporated using the *spacecharge3Dmesh* algorithm [65, 66]. The applied macroparticle number in the simulation is 10,000. Instead of initial emittance, the mean transverse energy (MTE) was included. The MTE is a figure of merit used to characterize the photocathode thermal emittance [51]. The normalized *rms* transverse emittance at the cathode is given by:

$$\epsilon_{\mathrm{n},\perp} = \sigma_\perp \sqrt{\frac{\mathrm{MTE}}{mc^2}}, \tag{116}$$

is 0.1348 mm mrad for a mean transverse energy of 30.691 meV for the GaAs photocathode.

5.2.1 BEAM TRANSMISSION AT 130 kV

The beam dynamics simulations were conducted to assess the beam transmission through the CEBAF injector by determining the beam interceptions at the apertures, varying the charge per bunch from low to high. Figure 31 illustrates the beam transmission through the apertures as a function of the bunch charge. The graph depicts a decrease in transmission with an increase in bunch charge. Specifically, for a 64 ns bunch spacing and a 0.32 pC bunch charge, the beam transmission is approximately 92%. However, the transmission decreases

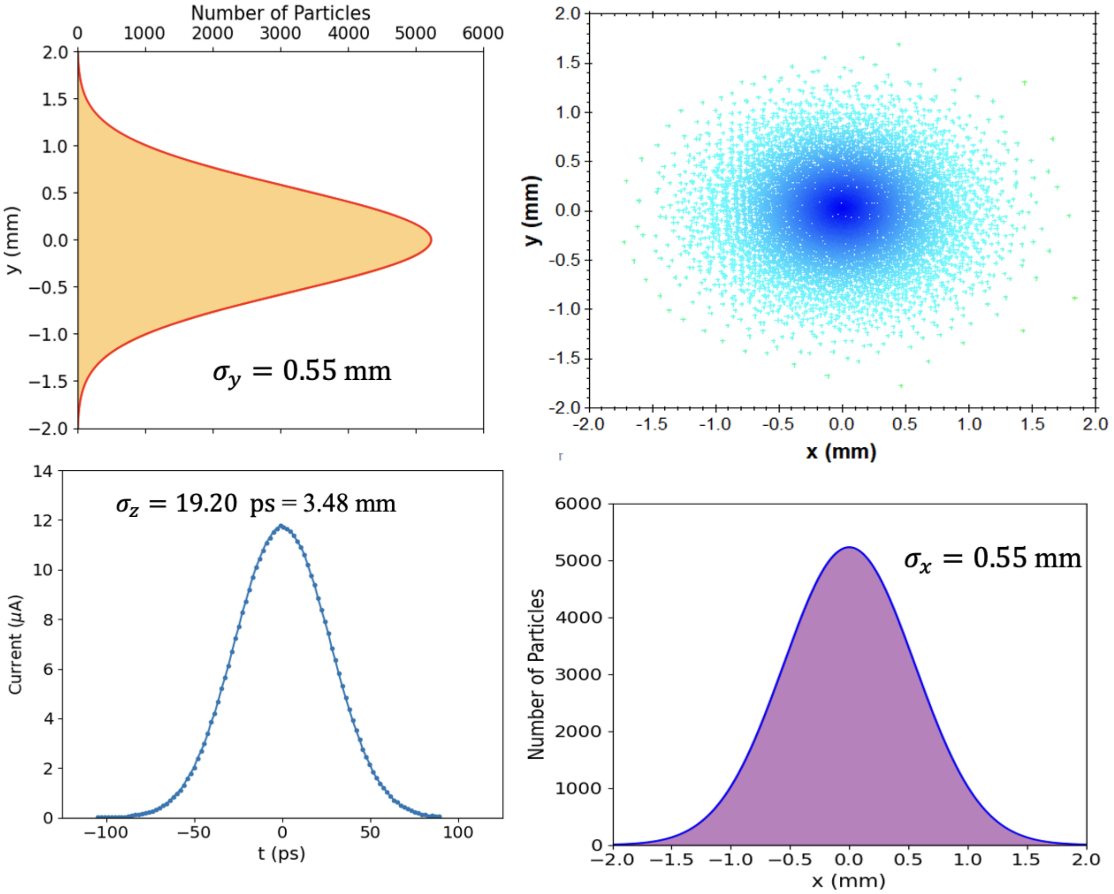

FIG. 30. Initial particle distribution at cathode for GPT simulation. The transverse and longitudinal beam distributions at the cathode are Gaussian in both transverse and longitudinal directions, with $\sigma_x = \sigma_y = 0.55\,\mathrm{mm}$ and $\sigma_z = 19.20\,\mathrm{ps}$ (3.48 mm).

to about 82% for a 128 ns bunch spacing and a 0.64 pC bunch charge.

Throughout this thesis a goal of 90% beam transmission through the apertures is considered acceptable, based on previous operating experience at CEBAF. The simulations indicate that for most conditions, 0.32 pC bunches have acceptable transmission. On the other hand, the higher-charge 0.64 pC bunches transmit cleanly over a much more limited range of parameters.

Additionally, we varied the laser spot size and the laser pulse length at the cathode to observe the transmission as a function of these parameters. Figure 32 displays the beam

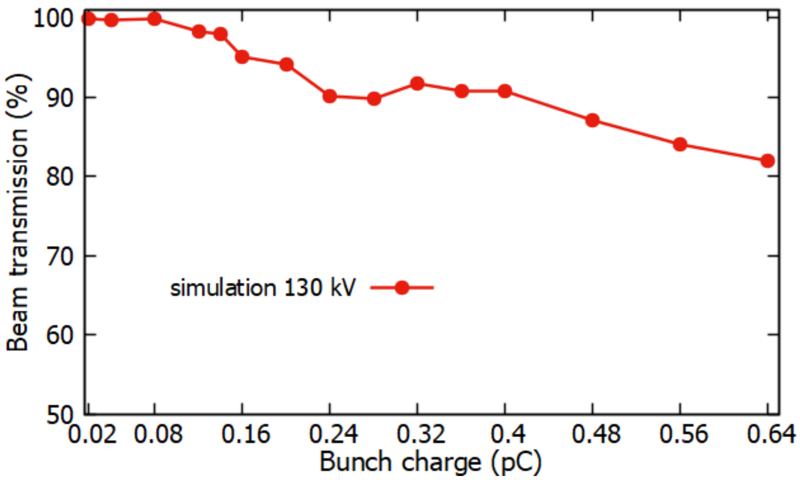

FIG. 31. Simulated beam transmission through the apertures A1 and A2 as a function of bunch charge at 130 kV DC gun voltage.

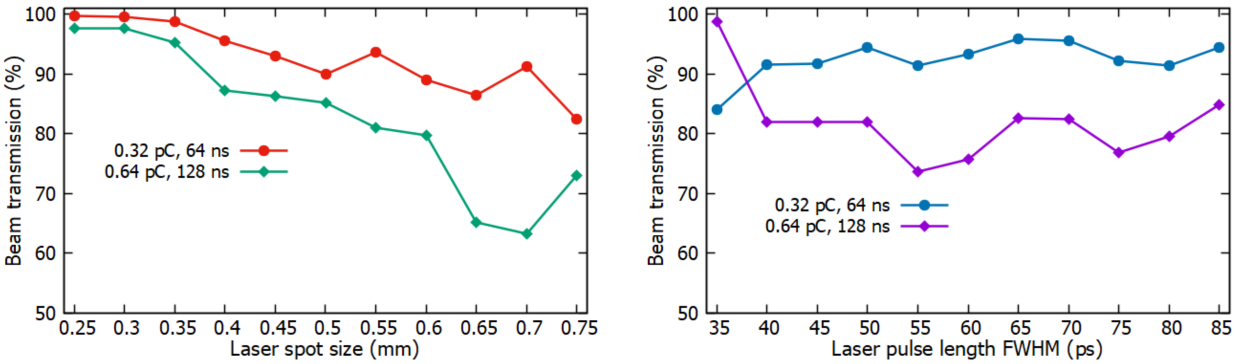

(a) Beam transmission versus laser spot size. (b) Beam transmission versus laser pulse length.

FIG. 32. Simulated beam transmission through the apertures A1 and A2 with variation of (a) laser spot size (b) laser pulse length at cathode size for 64 ns and 128 ns beam at 130 kV gun voltage.

transmission versus laser spot size and laser pulse length at the cathode for two different bunch spacings: 128 ns and 64 ns, respectively. In Fig. 32(a) it is evident that the beam transmission decreases for both bunch spacings (128 ns and 64 ns) with an increase in spot size. However, after an initial decrease, the transmission starts to increase. Furthermore, in Fig. 32(b), for both bunch spacings, there is no consistent increase or decrease in beam transmission with an increase in laser pulse length.

Following the simulations, we conducted experimental measurements to analyze beam transmission concerning bunch charge at varying drive frequencies of the laser: one at 249.5 MHz and another at 499 MHz. Figure 33(a) reveals that for a 499 MHz drive frequency, only 0.4 pC of charge could be obtained from the gun, resulting in approximately 10% beam loss. Conversely, at the 249.5 MHz laser drive frequency, more charge than the K_L beam requirement was achievable, although losses in the apertures (A1, A2, and MS) were notably high. With a 0.65 pC bunch charge from the gun, the loss amounted to approximately 39%. Furthermore, we compared the experimental measurement of beam transmission with particle tracking GPT simulations, illustrated in Fig. 33(b). Our simulation results closely align with the measurements. The beam transmission experiences a decline with an increasing charge per bunch due to the space charge effect. The self-induced forces resulting from space charge consistently exhibit defocusing effects in either the x or y directions [26].

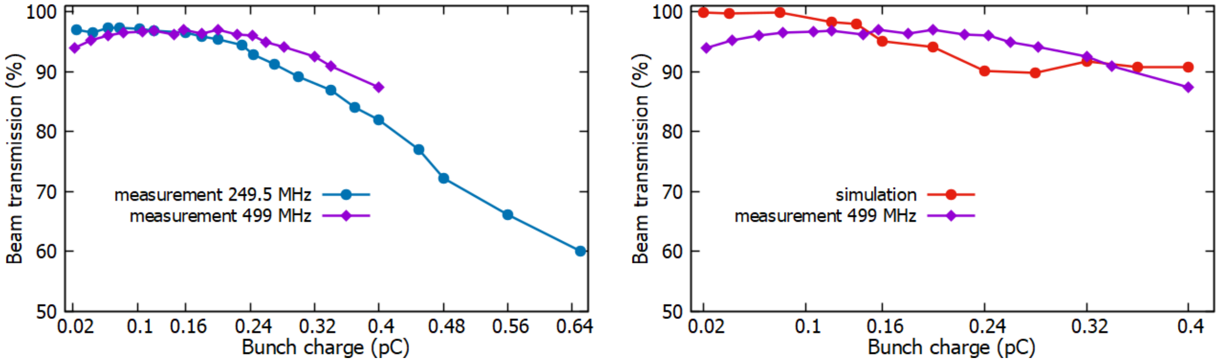

(a) Measured beam transmission.

(b) Comparison: simulation and measurement.

FIG. 33. Comparison between simulation and measurement for beam transmission vs. bunch charge: (a) Beam transmission through apertures A1, A2, and Master slit vs. bunch charge from the gun for different laser drive frequencies, and (b) Comparison between simulation and measurement for beam transmission vs. bunch charge at the 130 kV DC gun voltage.

5.2.2 BUNCH LENGTH MEASUREMENT AT 130 kV

The slit-chopper scan (chopper phase scanning) is an invasive technique used to measure the bunch length of a beam at the location of a chopper. To perform the measurements, the prebuncher gradient is set to zero. One of the CEBAF drive lasers (either 249.5 MHz or 499 MHz) is used to produce an RF-bunched beam, which is then sent to the chopper cavities. The average beam current is varied by adjusting the power of the drive laser light, and it is measured using a Faraday cup upstream of components that intercept the beam. For each beam current, the bunches are moved across the narrow chopping aperture by incrementally adjusting the laser phase relative to the chopper cavities in 0.5-degree steps. The electron beam passing through the slit is monitored using a downstream Faraday cup, providing a measurement of the electron bunch length (full width half maximum, FWHM) and shape. As the chopper frequency is 499 MHz, the pulse length of the beam at different drive frequencies is calculated as 5.6 ps per degree.

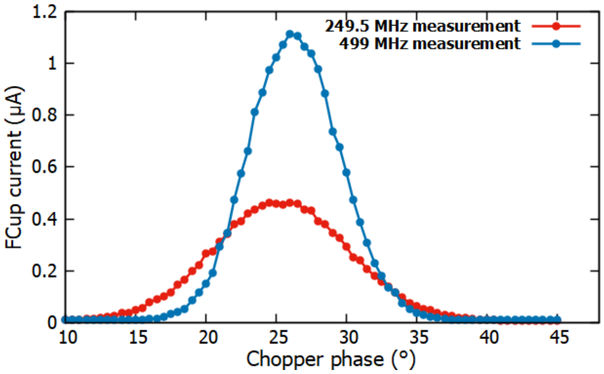

FIG. 34. Chopper phase scan for measuring beam pulse length for different beam frequency created by the drive laser C at 130 kV gun voltage. Measurements at low charge per bunch and negligible space charge, reflecting the laser pulse length.

The actual bunch length is determined by deconvolving the notch size from the raw data using the formula:

$$\sigma_{cor} = \sqrt{\sigma_{meas}^2 - \text{notchsize}^2} \tag{117}$$

Here, σ_{cor} is the full width at half maximum (FWHM) for the actual bunch length, σ_{meas} is the FWHM for the measured bunch length, and the notch size is equal to $(18 \pm 1\ )$ ps, which represents the width of the narrow chopper slit. The statistical fluctuations in the measurements are smaller than the data points on the graphs.

The length and shape of a 10 fC electron bunch at 249.5 MHz and 499 MHz frequency for C laser is measured at the location of 499 MHz chopper. Figure 34 shows the measurement data and corresponding Gaussian fit for finding the pulse length of the beam for different drive frequency of the laser. The length of the bunch is about 42.50 ± 0.22 ps full width at half maximum (FWHM) for 499 MHz drive frequency and about 63.83 ± 0.27 ps FWHM for 249.5 MHz drive frequency. The data shows that the different mode of drive frequency has beam of different pulse length, when space charge is low.

Compared to the pulse length at low current the electron bunch length is much longer for higher currents (higher bunch charge) as shown in Fig. 35. The results demonstrate that the bunch length increases with increasing charge per bunch. Furthermore, for the same charge per bunch the space charge effects are reduced for 249.5 MHz beam as at the cathode it begins longer. With increasing charge per bunch, the longitudinal temporal distributions of the bunch initially become Gaussian and then become non-Gaussian (e.g., Super-Gaussian of higher order), as shown in Fig. 35.

At low charges up to 60 fC, the longitudinal profile of the bunch at chopper is Gaussian, given by the following formula:

$$f(x) = \frac{A}{\sigma\sqrt{2\pi}} \exp\left(-\frac{(x-\mu)^2}{2\sigma^2}\right), \tag{118}$$

where A is the amplitude, σ is the *rms* value of the distributions, and μ is the mean of the distributions. When the bunch charge is increased the longitudinal profile of the bunch at chopper is a Super-Gaussian function that describes a more rectangular distribution by the following formula [71]:

$$\begin{aligned} g(x) &= \frac{A}{\sigma_0\sqrt{2\pi}} \exp\left(-\frac{(\text{abs}(x-\mu))^N}{2\sigma_0^N}\right) \\ \text{with} \quad \sigma &= \sigma_0 \left(\frac{\pi}{2}\right)^{2/N-1}. \end{aligned} \tag{119}$$

Here, σ_0 is the *rms* value of the Super-Gaussian distributions, and N is the exponent of the Super-Gaussian and will give a Gaussian distribution for $N = 2$. For large N, the function

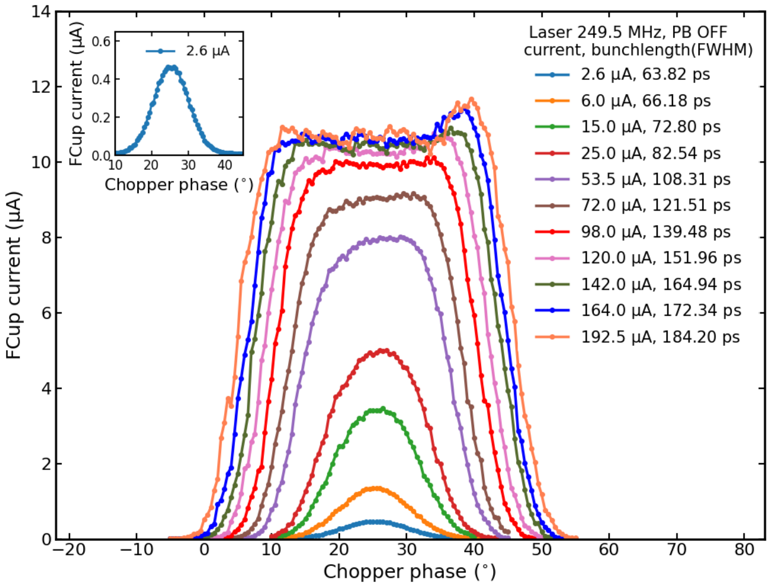

(a) Bunch length measurement at 249.5 MHz.

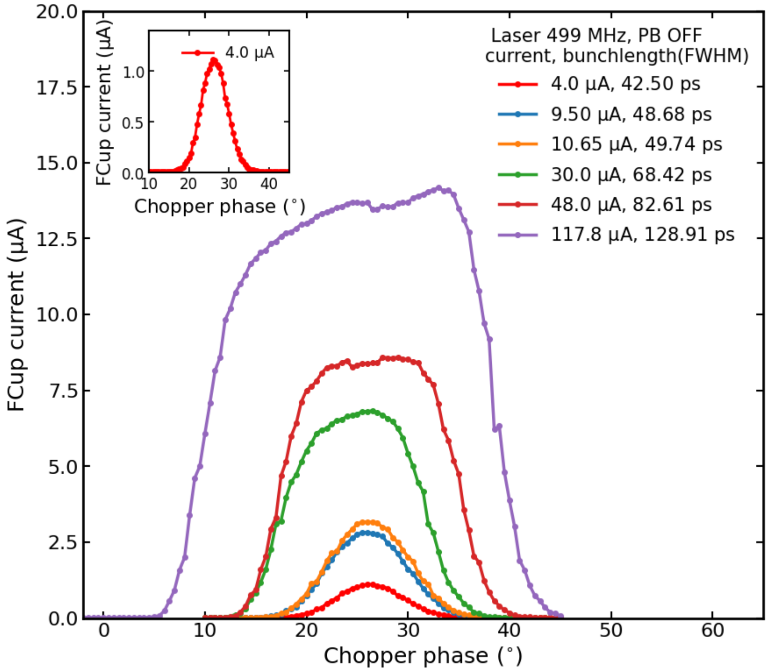

(b) Bunch length measurement at 499 MHz.

FIG. 35. Electron bunch length measurements using the RF chopper cavity at 130 kV gun voltage. The average beam current ranges from (a) 2 to 195 µA at 249.5 MHz laser and (b) 4 to 120 µA at 499 MHz. The insets at the top of each plot provide more detail for the lowest current measurements, which experience the least amount of space charge-induced bunch length growth.

will describe a more rectangular distribution, while for small N, it fits to a distribution with long tails on both ends. The measurement data and corresponding super Gaussian fits for pulse lengths at various charges for different drive frequencies of the laser are shown in Fig. 36.

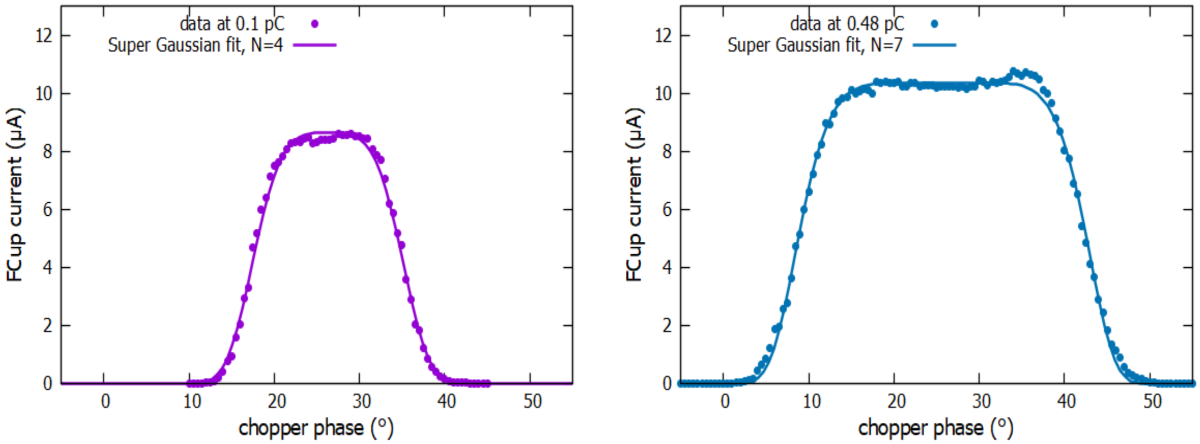

(a) Chopper phase scan at 0.1 pC.

(b) Chopper phase scan at 0.48 pC.

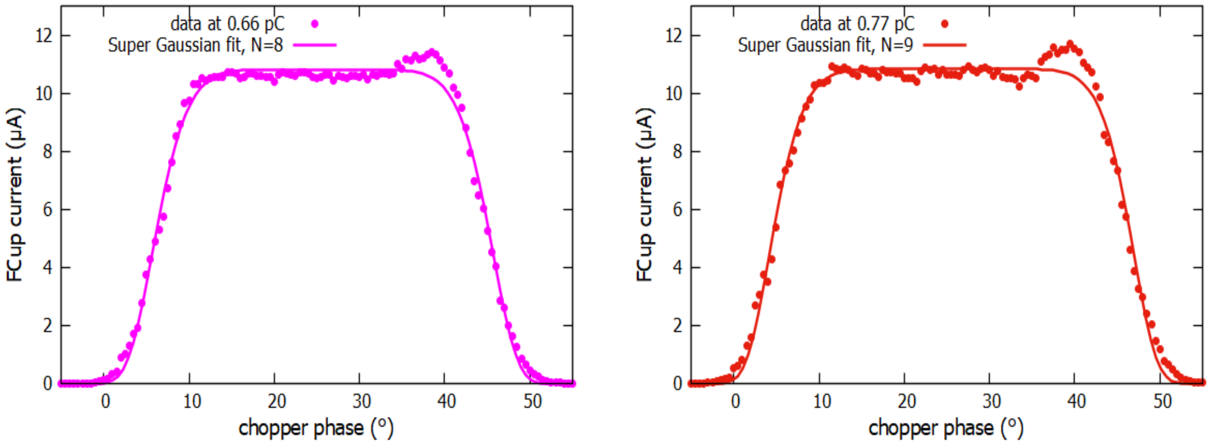

(c) Chopper phase scan at 0.66 pC.

(d) Chopper phase scan at 0.77 pC.

FIG. 36. Longitudinal bunch profile measurements at the chopper for 130 keV beam for (a) 0.1 pC at 499 MHz Laser, (b) 0.48 pC at 249.5 MHz Laser, (c) 0.66 pC at 249.5 MHz Laser, and (d) 0.77 pC at 249.5 MHz Laser.

Note that at higher currents (charge) for both drive frequencies of the laser, the electron bunch shape first becomes a symmetric Super-Gaussian, but then it becomes asymmetric with some cusps in the distribution. This behavior is completely different from the previously observed longitudinal temporal bunch profile described in Refs. [72] and [16]. The shape of the bunches changes from an asymmetric Gaussian distribution in Ref. [72] to the symmetric super-Gaussian distribution for high charge. The initial beam sizes of the laser at the photocathode is greater than the factor of 2 in our case than that of Ref. [72]. Additionally, it has been found that the bunch length of the electron bunch decreases with an increase in the laser spot size at the cathode. Moreover, the rate of expansion in bunch length is different for both repetition rates, with the smaller bunch length at low current (low charge) for 499 MHz expanding more rapidly than that of 249.5 MHz. For a bunch charge of 0.1 pC and for both repetition rates, the measured bunch length is 82.60 ps, and the longitudinal bunch profile is shown in Fig. 37. The reduced space charge effect is evident in the 249.5 MHz beam, as it retains its more Gaussian longitudinal distribution for the same charge because the beam has expanded less.

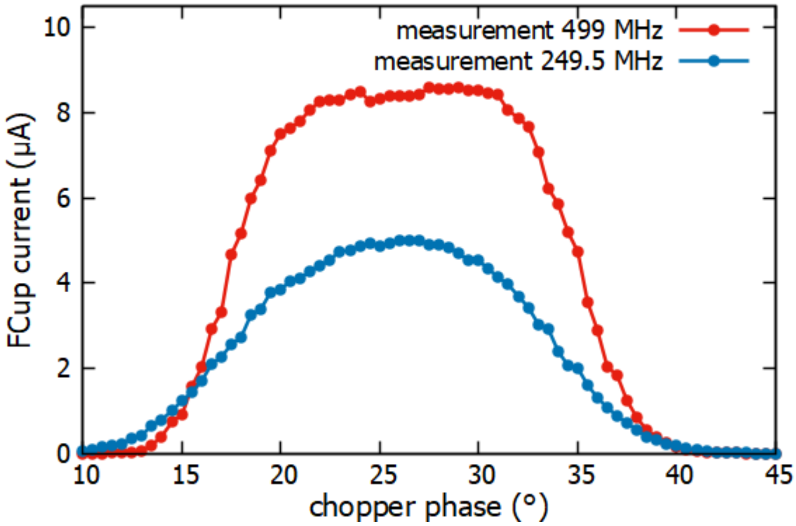

FIG. 37. Longitudinal bunch profile measurements at the chopper for different drive frequencies for 0.1 pC bunch charge at 130 kV gun voltage.

To understand the measurements obtained from the chopper phase scan technique, we utilized the General Particle Tracer (GPT) [64] modeling program to forecast the electron bunch-length at the chopper location. In this study, for this case we used both space charge scheme, *spacecharge3Dmesh* [65, 66] and *Spacecharge3D* [67] to calculate the space charge. Both algorithms employed identical field maps for the gun and RF components as well as the solenoid magnet. The longitudinal shape and the laser pulse length used in the simulations were measured for each drive frequency by sending a near-zero charge beam (10 fC) through the injector (see Fig. 34). As there is very little growth from space charge, the temporal profile remains nearly constant throughout the simulations along the beamline. The laser pulses used had a full width at half maximum (FWHM) of 41.6 ps for the 499 MHz laser and 62.5 ps for the 249.5 MHz laser. The beam current varied from 2.5 µA to 200 µA for the 249.5 MHz laser frequency and from 4.0 µA to 120 µA for the 499 MHz laser frequency as we performed in the experimental measurements. The presented results are based on simulations made with 10,000 macroparticles.

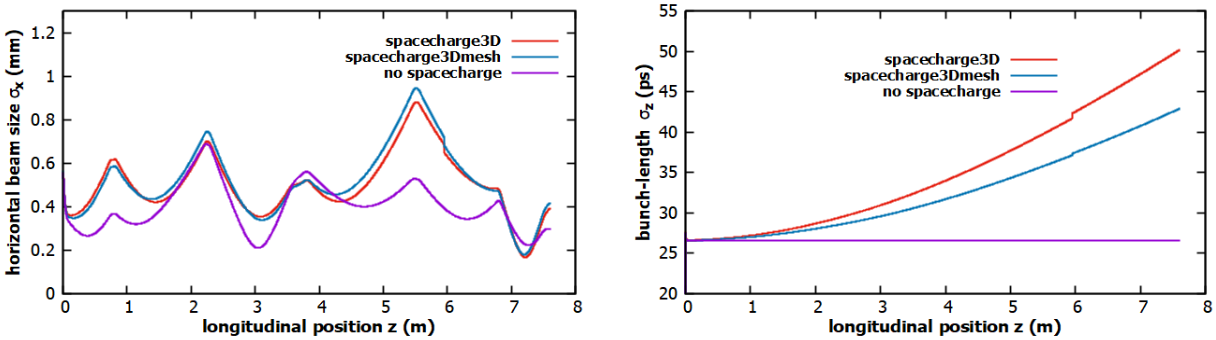

(a) Horizontal *rms* beam size at 0.40 pC.

(b) Longitudinal *rms* beam size at 0.40 pC.

FIG. 38. Simulation results showing the (a) horizontal and (b) longitudinal, *rms* beam sizes as a function of distance from the photocathode for different space-charge schemes for 0.40 pC bunch charge at 130 kV gun voltage.

Figure 38 shows examples of the beam evolution, including the horizontal beam size (σ_x)

and bunch length (σ_z), for beams originating at the photocathode and extending through the injector, for various space-charge models at a laser drive frequency of 249.5 MHz. Similarly, the evolution of bunch length (σ_z) for beam originating at the photocathode and extending through the injector, for several bunch charge with *spacecharge3D* routines at a bunch repetition rate 249.5 MHz is shown in Fig. 39.

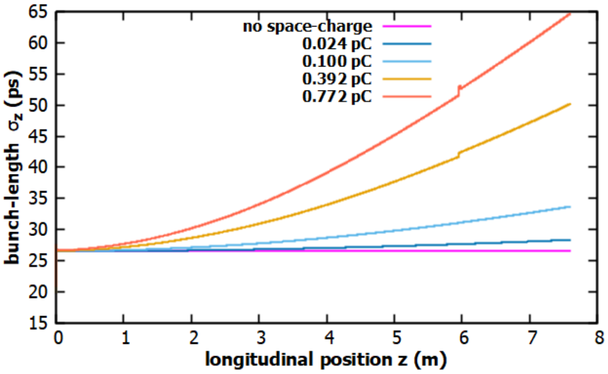

FIG. 39. Simulation results showing the *rms* bunch length as a function of distance from the photocathode for *spacecharge3D* scheme for various bunch charges at 130 kV gun voltage.

The bunch length values obtained from measurements and simulations for different space charge schemes are presented in Fig. 40, using both laser frequencies of 249.5 and 499 MHz. The results show that there is excellent agreement between the measurements and simulations for the *spacecharge3D* scheme at low charges, with a deviation of no more than 15% even at high charges. For the *spacecharge3Dmesh* scheme, there is also good agreement between the measurements and simulations at low charges. However, the deviation between the simulation results and measurements becomes more significant at high charges (currents). The simulation data and measurement data and corresponding Gaussian fit for low current 2.6 µA and simulation data, measurement data and corresponding Super-Gaussian fit for high current 192.5 µA out of the DC gun at 249.5 MHz are shown in Fig. 41. Also, the longitudinal bunch profiles obtained from the chopper phase scanning technique and particle

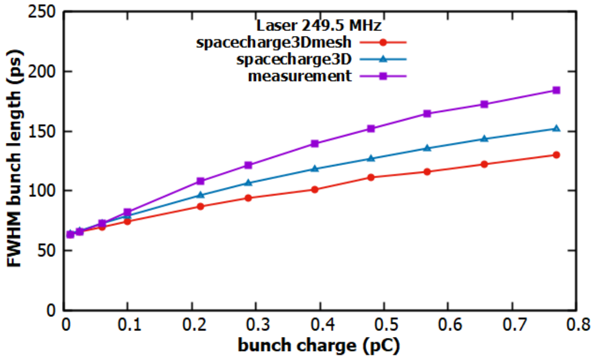

FIG. 40. Electron bunch length as a function of bunch charge with measurements obtained using the invasive chopper phase scanning technique together with simulation results using the particle tracking code GPT for different space charge schemes at 249.5 MHz laser (left) and at 499 MHz laser (right) at 130 kV gun voltage with prebuncher OFF.

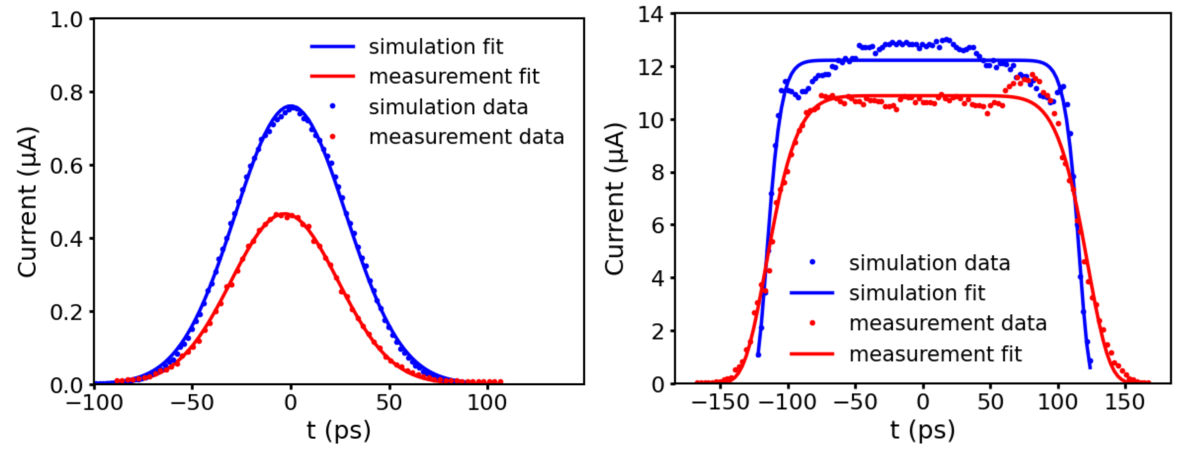

(a) Measurement and simulation 2.6 µA. (b) Measurement and simulation 192.5 µA.

FIG. 41. Comparison of longitudinal bunch profiles between chopper phase scanning and GPT simulation for low and high charge at 130 kV gun voltage. (a) 2.6 µA, and (b) 192.5 µA at 249.5 MHz laser.

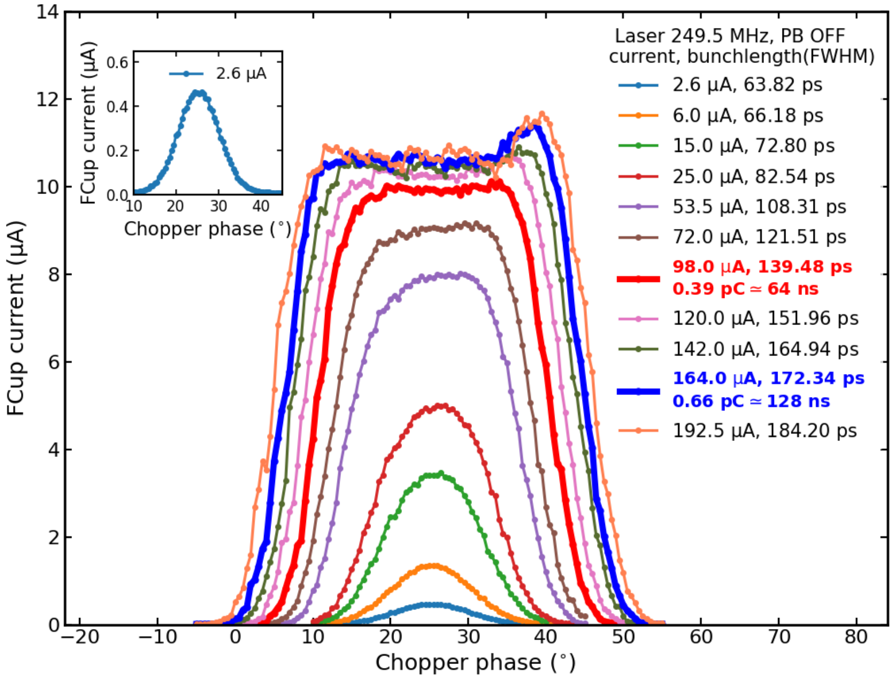

(a) Chopper phase scanning technique.

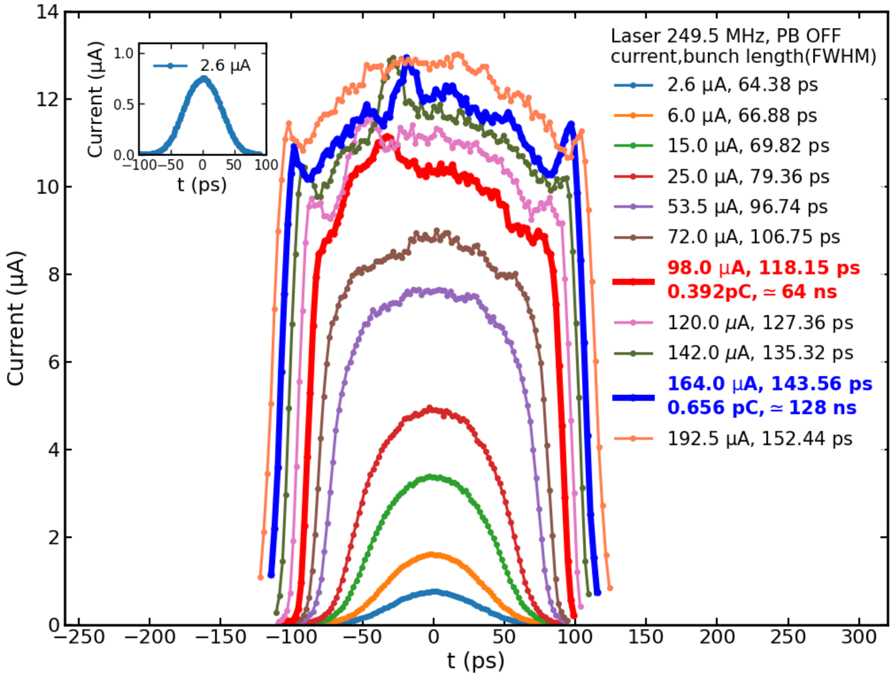

(b) GPT particle tracking.

FIG. 42. Longitudinal bunch profile comparison between chopper phase scanning and simulation at 130 kV gun voltage. (a) Chopper phase scanning technique. (b) GPT Particle tracking simulations. The x-labels for the two plots in Fig. 42(a) and Fig. 42(b) are related by $1^\circ = 5.6$ ps.

tracking simulations and is shown in Fig. 42. There is an excellent agreement between simulations and measurement.

The same measurements and simulation schemes were repeated for the 249.5 MHz and 499 MHz laser settings, with the prebuncher (PB) cavity turned ON. In the simulations, the amplitude of the prebuncher was set to 0.55 MV/m, with zero crossing of synchronous RF phase, which corresponds to the optimized settings of the prebuncher for CEBAF injector operations. The results show that the bunch length gradually increases with increasing charge per bunch. Furthermore, with the prebuncher turned on, the longitudinal profile of the bunch remains Gaussian for both low and high charge per bunch for both drive frequencies of the laser, as shown in Fig. 43.

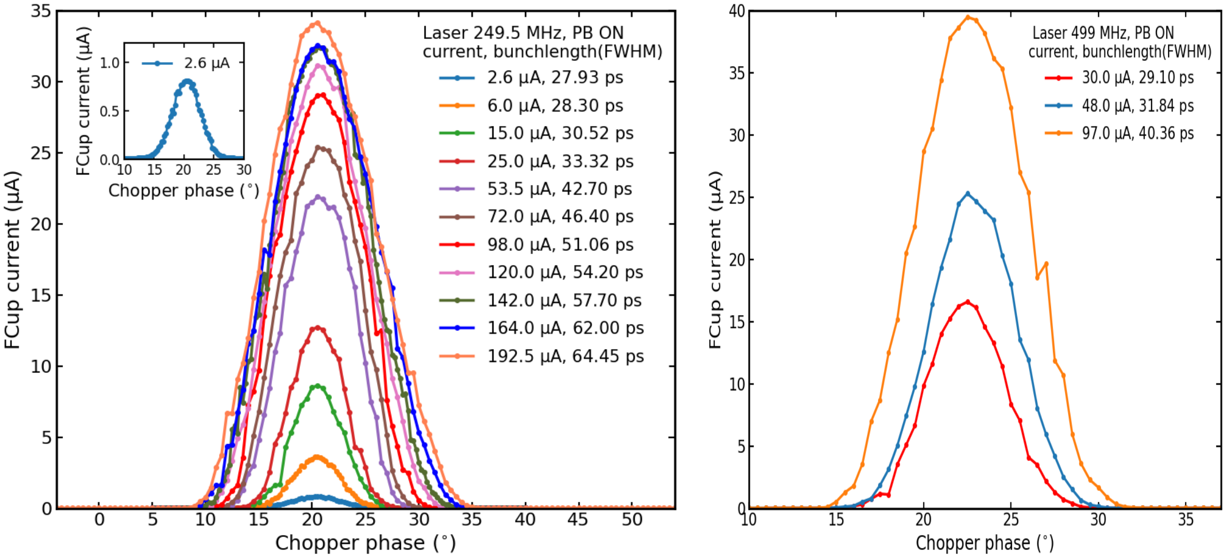

(a) Measurement at 249.5 MHz.

(b) Measurement at 499 MHz.

FIG. 43. Electron bunch length measurements using the RF chopper cavity with prebuncher ON at 130 kV gun voltage. The average beam current ranges from (a) 2 to 195 μA at 249.5 MHz laser and (b) 4 to 120 μA at 499 MHz. The insets provide more detail for the lowest current measurements which suffer the least amount of space charge-induced bunch length growth.

The bunch length values obtained from measurements and simulations for different space charge schemes are presented in Fig. 44, using both laser frequencies of 249.5 and 499 MHz. The results show that there is excellent agreement between the measurements and simulations of the compressed bunch length for the both space charge schemes.

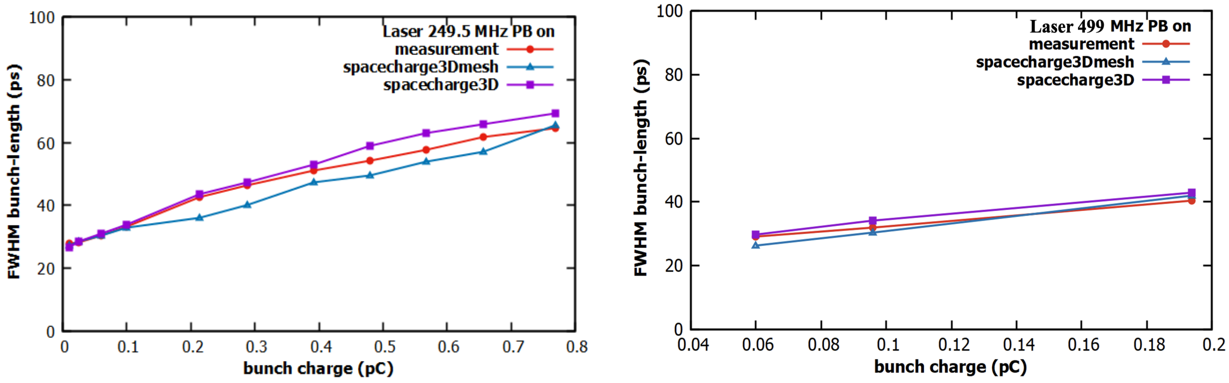

(a) Bunch length at 249.5 MHz.

(b) Bunch length at 499 MHz.

FIG. 44. Comparison of electron bunch length measurements between chopper phase scanning and GPT simulation with the prebuncher ON at a 130 kV gun voltage. Electron bunch length as a function of bunch charge, with measurements obtained using the invasive chopper phase scan technique, along with simulation results using the GPT particle tracking code for different space charge schemes at (a) 249.5 MHz laser and (b) 499 MHz laser.

5.3 CEBAF INJECTOR AT 180 kV DC GUN VOLTAGE

There are ongoing efforts to transition the gun voltages from 130 kV to 200 kV for the CEBAF injector. Following the Scheduled Accelerator Down (SAD) in 2023, the CEBAF Phase 2 injector beamline layout is present with changes in gun voltages. The Phase 2 upgrades involve various modifications in the positions of beamline elements, system upgrades, and notably, the replacement of the capture section and quarter cryomodule with a new booster module containing a 2-cell and 7-cell cavity string. The schematic of the CEBAF

Phase 2 upgraded injector layout is depicted in Fig. 45. Additionally, the details of the injector beamline elements, starting from the cathode, including magnetic elements, are provided in Table 4.

TABLE 4. Locations of the beamline elements for the Phase 2 CEBAF injector upgrade. Here, MDRs is the dipole magnet, MFs are the solenoids, MQs are the quadrupole magnets, HWien and VWien are the horizontal and vertical Wien system.

Location of Beam Line Elements			
Elements	Positions (m)	Elements	Positions (m)
MFX2I01	0.780796	MFX1dsch2	8.505764
MDR1I02	1.717802	MFX2dsch2	9.103426
MFX1I03	2.261358	FCup#1	9.462582
MQW1I03	2.636135	Buncher	9.586026
VWien	2.911598	A3	10.31653
MQW1I04	3.187061	MFX3dsch2	10.722422
MFG1I04A	3.573776	A4	11.199434
MFG1I04B	3.816954	2-cell	12.2754
MQW1I05	4.114669	7-cell	13.106
HWien	4.390132	MQS0L01	14.76567
MQW1I06	4.665595	MQJ0L01	14.9641
Prebuncher	4.823223	MQS0L01A	16.95193
MFX0I01	5.515352	MQJ0L02	18.0041
Pcup	5.801864	MQS0L02	18.33187
A1	5.938770	MQJ0L02A	18.6143
A2	6.616446	MQS0L02B	21.7726
MFA0I03	6.813235	MQJ0L03A	23.80147
MFD0I04A	7.514275	MQS0L03	24.1523
Chopper	7.60	MQJ0L03	24.43177
MFD0I04B	7.685725	MQS0L04	27.3836
MFA0I05	8.386765	MQJ0L04	27.585

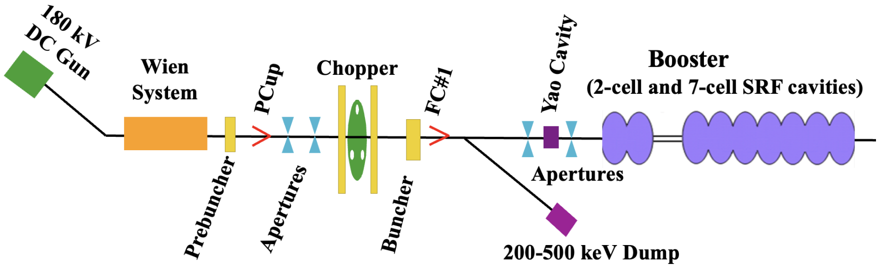

FIG. 45. CEBAF injector upgrade Phase 2 layout for 180 kV DC gun voltage. It shows the section extending from the gun to downstream of the booster. The injector layouts are not to scale, and magnet elements are not shown. PCup, and FC#1 are insertable Faraday cups.

5.3.1 180 kV GUN VOLTAGE MEASUREMENTS

During some parts of the CEBAF injector operation in Fall 2023, the DC gun voltage was 180 kV. The electron beam generated by three lasers had a frequency of either 249.5 MHz or 499 MHz. As outlined in Ref. [1], with the existing and planned gun configurations, laser development is essential to achieve the planned bunch repetition rates. Additional power amplification is required to accommodate the higher beam currents envisioned for this purpose. For the K_L experiment in Hall D, the baseline frequency for the CEBAF photoinjector drive laser is set at 15.59 MHz, with an additional desired frequency of 7.8 MHz [1]. Since Fall 2023, temporary solutions for the 15.6 MHz baseline are installed on the Hall D laser [73] to allow K_L beam studies. These solutions are expected to become permanent supporting the K_L experiment in the near future.

For the 180 keV beam from the gun, initial beam studies were conducted with horizontal Wien (HWien) filter activated and using a 249.5 MHz C laser, followed by a study using a 15.6 MHz K_L D laser. In the case of the 15.6 MHz laser, beam transmission, longitudinal bunch profile, and the corresponding expansion of bunch length from the gun to the chopper location were investigated using chopper phase scanning techniques. These experiments were carried out while gradually increasing the beam current from the gun. For the 249.5 MHz C laser, bunch length profiles and corresponding bunch lengths at the chopper location were examined as the beam current from the gun was increased. Subsequently, beam transmission measurements and chopper phase scans were performed for a 499 MHz drive laser with the

Wien system turned OFF. In all beam study measurements with a 180 kV gun, the beam was directed from the gun to the FC1, and the injector operated in high current (charge) mode.

TABLE 5. CEBAF injector beam transmission and interceptions at 180 kV DC gun voltage with 15.6 MHz D laser and with horizontal Wien filter ON.

Gun Current (µA)	Bunch Charge (pC)	A1 Interception (µA)	A2 Interception (µA)	MS Interception (µA)	Beam Transmission (%)
2.8971	0.186	0.1742	0.5242	0.0012	76.0
4.3704	0.280	0.0416	1.0437	0.0122	73.0
6.2193	0.399	0.2852	1.6462	0.1522	66.5
7.8976	0.506	0.9720	0.6986	0.2016	76.3
11.6756	0.748	3.555	0.9894	0.4536	57.2
17.3721	1.114	9.244	1.1736	0.8716	35.0

Table 5 presents the beam current from the gun, corresponding bunch charge at the 15.6 MHz laser, beam interceptions at the apertures (A1, A2, and master slits), and beam transmission in the injector. As expected, the table reveals a decrease in beam transmission with an increase in beam current. While the beam transmission is low with high charge, the transmitted beam current exceeds 5 µA, aligning with the K_L baseline beam current at 15.6 MHz. Consequently, the new Hall D K_L laser with an amplifier provides sufficient beam current (charge) from the gun for the K_L experiment. The results of the beam transmission, varying with bunch charge, alongside the regression fit and the transmission goal, are depicted in Fig. 46. The increase of the beam transmission around 0.5 pC charge per bunch may be attributed to the optimization of focusing optics. It is possible that at this specific bunch charge, the focusing optics, such as the solenoids, are finely tuned to compensate for space charge effects that would otherwise diminish transmission. However, this optimization may not apply uniformly across all bunch charges, thus resulting in the observed change. Compared to the 130 keV beam running, the transmission losses were comparable and somewhat higher, inconsistent with the reduced space charge effect expected at higher energy. As discussed later, the main reason is that activating the Wien filter decreased the transmission substantially.

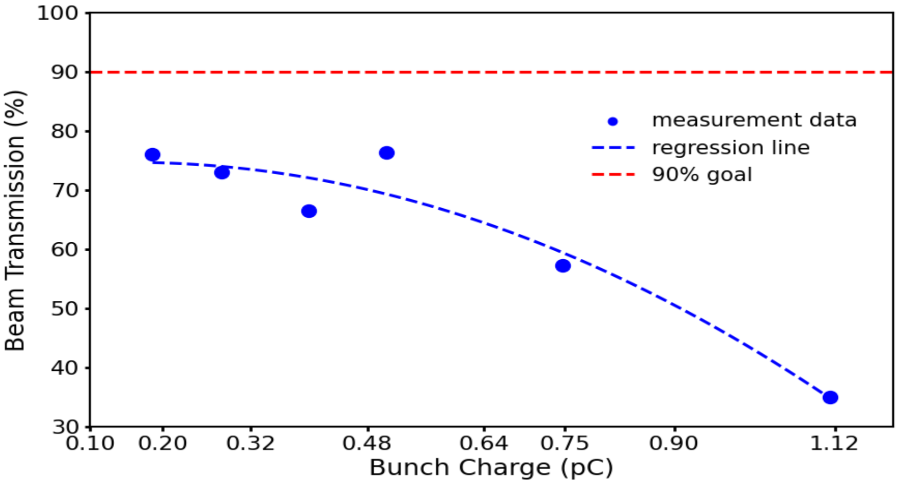

FIG. 46. Beam transmission as a function of bunch charge for K_L laser at 15.6 MHz for 180 kV gun voltage.

The longitudinal bunch profile for the 15.6 MHz laser, obtained using chopper phase scanning techniques for various beam currents (bunch charges) from the gun, is depicted in Fig. 47. By analyzing the Faraday cup current vs. chopper phase distribution, the bunch length for the electron beam at the chopper location is calculated. The bunch profile for all beam currents is Gaussian, and the bunch length increases with the beam current due to space charge expansion. The 1 µA phase plot indicates that the 15.6 MHz laser pulses have a pulse length of less than 73 ps, as the charge for the 1 µA is 0.064 pC, and there is still a bunch length expansion.

The beam transmission for the C laser at 249.5 MHz is also low with horizontal Wien filter

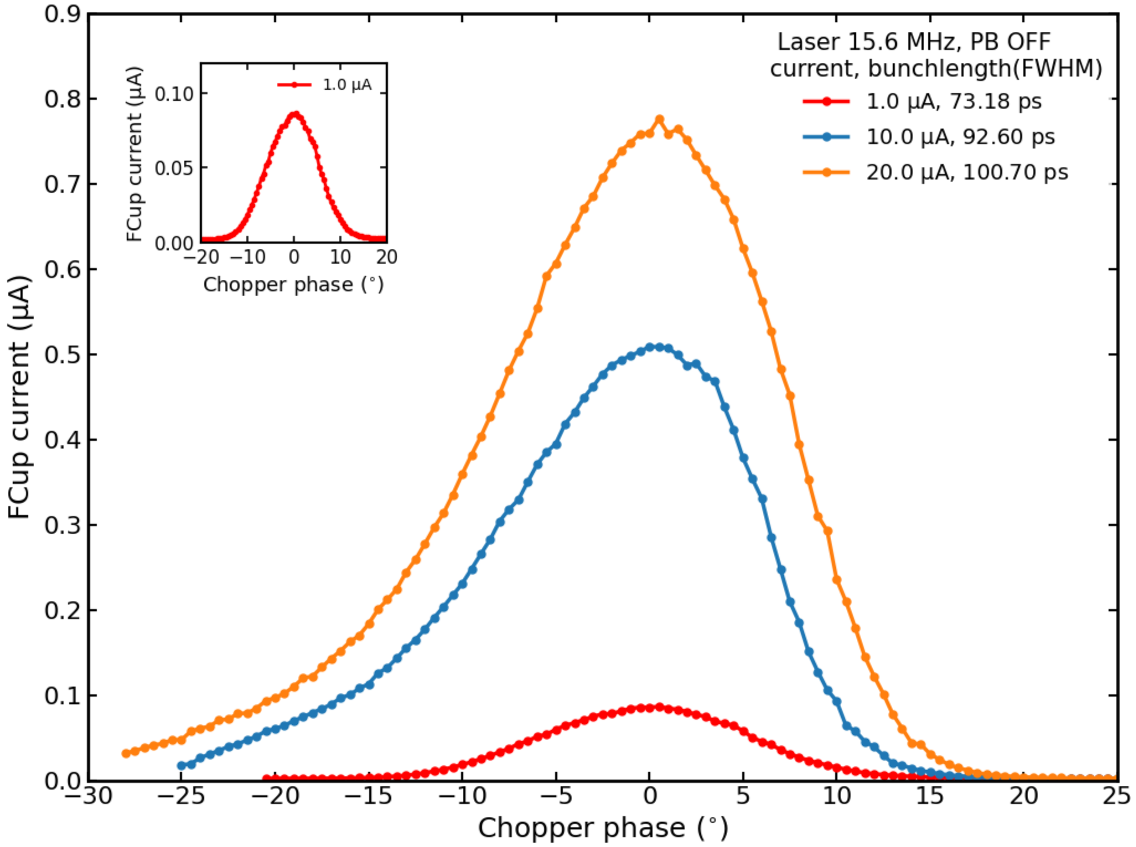

FIG. 47. Electron bunch length measurements using the RF chopper cavity for 15.6 MHz laser at 180 kV gun voltage. The insets provide more detail for the lowest current measurement.

.

turned ON. The beam transmission is 74% at 5 µA current (0.06 pC bunch charge) and 55% at 72.5 µA current (0.29 pC bunch charge). Following the beam transmission, chopper phase scanning was performed for the 249.5 MHz C laser with horizontal Wien filter turned ON to observe space charge effects with variation of beam current through the CEBAF injector from the gun to the location of the chopper. The measured longitudinal bunch profile for various beam currents from the gun for the 249.5 MHz laser is presented in Fig. 48. Despite significant beam loss in the apertures, the longitudinal bunch profile remains Gaussian, and the bunch length due to space charge is not excessively high. The bunch length expansion should decrease with an increase in gun voltage, but this is influenced not only by the rise

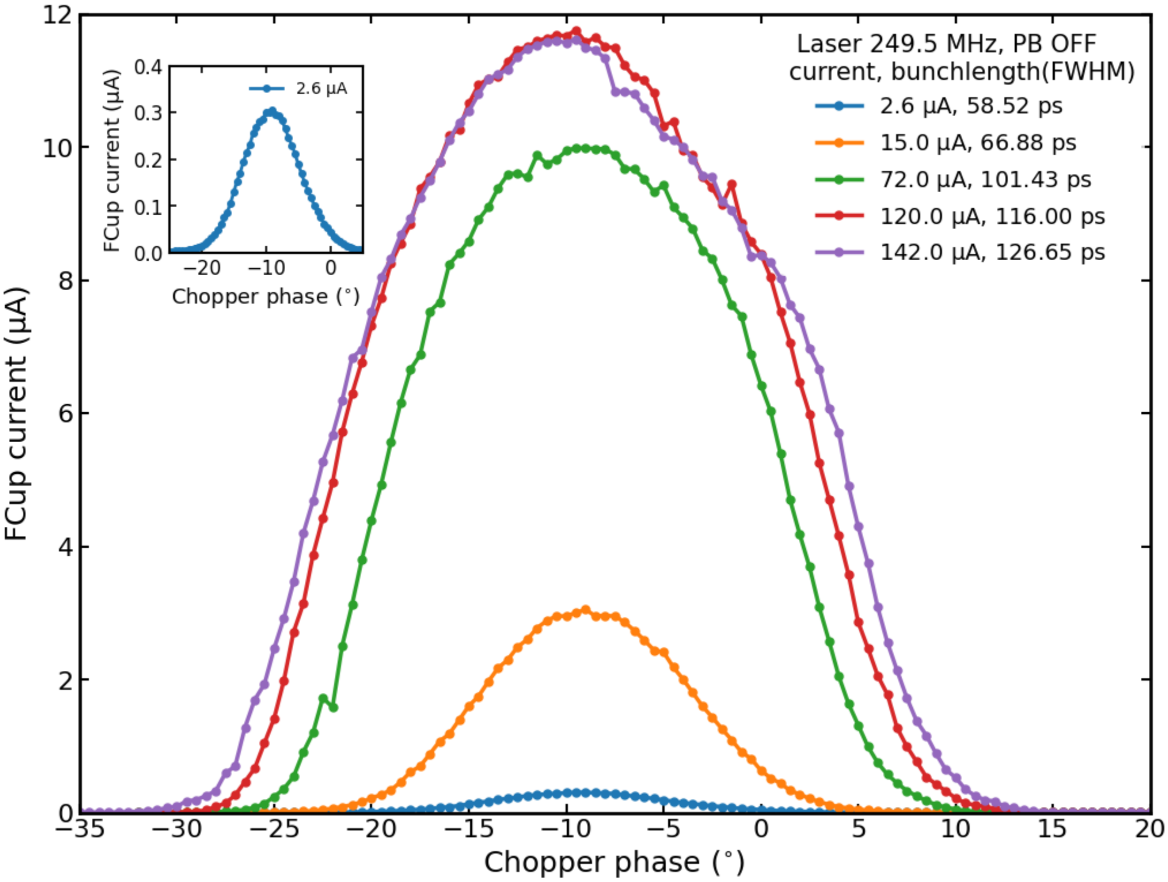

FIG. 48. Electron bunch length measurements using the RF chopper cavity for the 249.5 MHz C laser at 180 kV gun voltage. The gun current was varied from 2 μA to 142 μA. The insets provide more detail for the lowest current measurement.

in beam energy but also by the substantial loss of beam in the injector apertures.

Since the K_L experiment does not require a parity-quality beam and there were high beam losses with Wien filter ON, the experiment was repeated to measure beam transmission and longitudinal bunch profiles at 180 kV with the Wien filter OFF. The beam test plan intended to use the 15.6 MHz K_L and 499 MHz C laser. Due to technical issues during the initial beam test, the study was conducted only with the 499 MHz C laser, and the second opportunity was missed due to a gun tripping event.

Figure 49 illustrates the beam transmission as a function of bunch charge with Wien filter OFF for the C laser at 499 MHz with a 180 kV DC gun. As seen in the figure, the beam

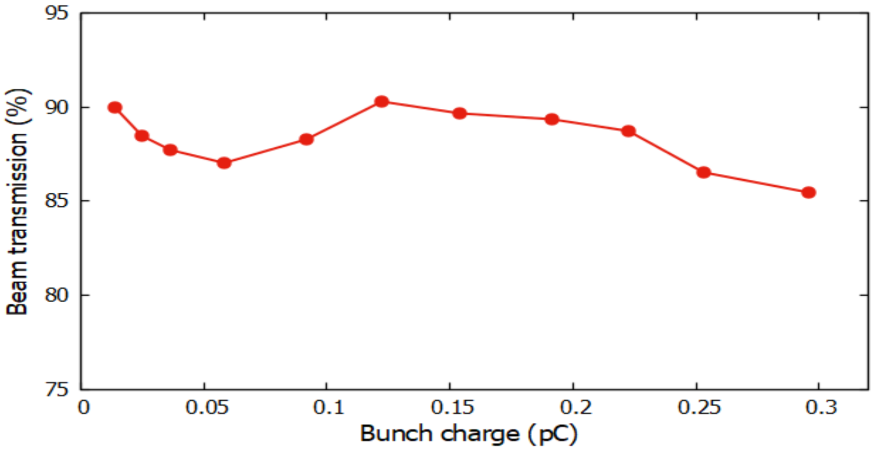

FIG. 49. Beam transmission as a function of bunch charge for 499 MHz laser at 180 kV gun voltage with Wien filter turned OFF.

transmission is higher compared to Wien filter ON, but the C laser at 499 MHz could not provide sufficient bunch charge (beam current), even reaching 0.32 pC for the K_L experiment. Compared to the 130 keV experiment, also with the Wien OFF (data in Fig. 33), the total transmission is very comparable at around 90%.

The longitudinal bunch profile and corresponding bunch length at the location of the chopper for the 499 MHz laser are shown in Fig. 50. At low charge (low current), the longitudinal profile of the bunch at the chopper location is Gaussian with a FWHM bunch length of about 40 ps, as in the 130 keV experiment. With an increase in charge per bunch, the distribution becomes Super-Gaussian, starting from 40 µA (80 fC charge). The increase in bunch length and longitudinal bunch profile distributions follows the same trend as in Section 5.2.2 for 130 kV. However, for a beam energy of 180 keV the bunch length expansion is lower due to the reduced space charge. For the same charge per bunch, the bunch length is smaller at the location of the chopper compared to 130 kV (see Fig. 35(b)).

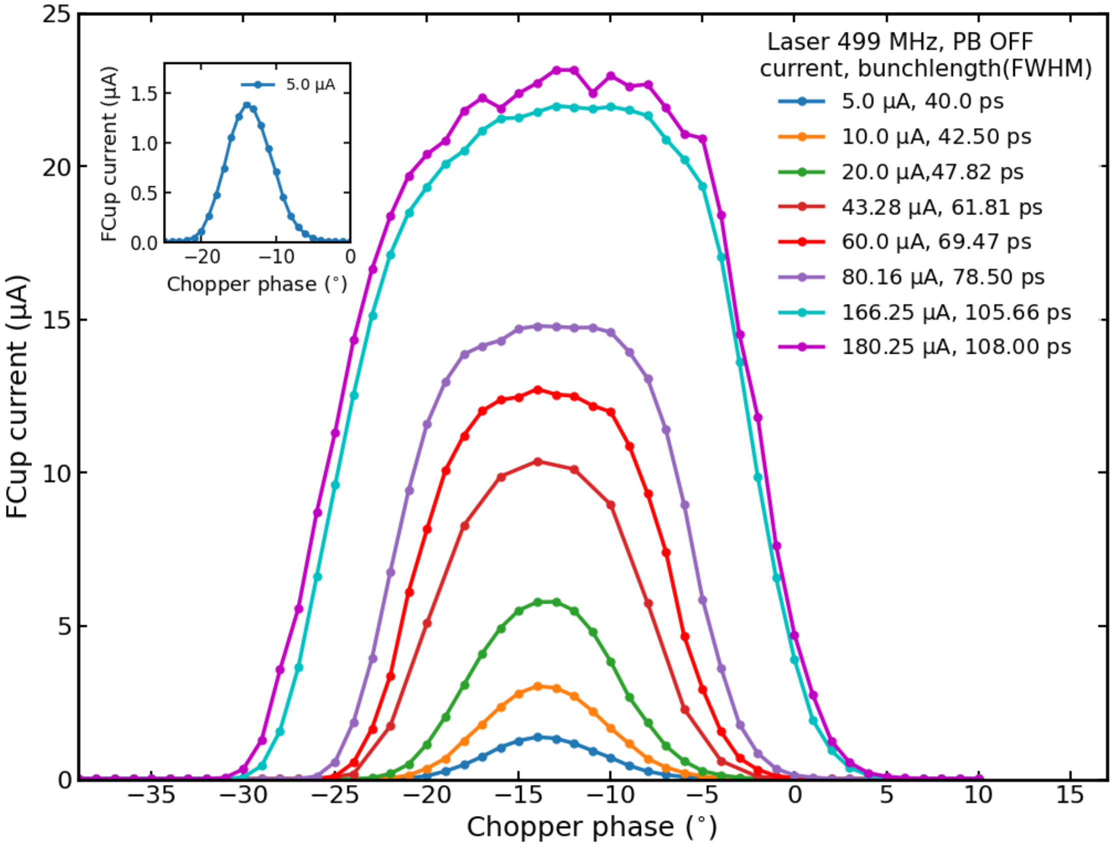

FIG. 50. Electron bunch length measurements were using the RF chopper cavity for the 499 MHz laser at 180 kV gun voltage with Wien filter turned OFF. The gun current was varied from 5 µA to 182 µA. The insets provide more detail for the lowest current measurement.

5.3.2 INJECTOR OPTIMIZATION AND SIMULATION AT 180 kV DC GUN

Based on the setting of the injector gun voltage to 180 kV for the CEBAF Phase 2 upgraded injector operations in Fall 2023, we initiated the optimization of the Continuous Electron Beam Accelerator Facility (CEBAF) injector for the Phase 2 injector configuration. Employing Multi-Objective Genetic Optimization (MGO) through General Particle Tracer (GPT), we determined the necessary magnetic elements and RF settings for the K_L bunch charge (0.64 pC) at 180 kV. The 180 kV gun voltage may also be used for future operations of the CEBAF injector.

For the injector DC gun voltage settings for the 2023 Fall operation of 180 kV, injector optimizations were performed. The GPT model of the CEBAF injector at a 180 kV DC gun employs the same field maps for the gun, most solenoids except MFXs, and prebuncher and buncher as used in the 130 kV configuration. However, some beamline positions of the elements are adjusted, some solenoids are removed, and the booster (2-7 cell SRF cavities) replaces the capture and two 5-cell cavities. The objective for different field maps for MFXs is associated with MFX solenoids repairs, as there is a problem associated with beam transmission in the solenoids. For this, we utilized the first two MFX solenoids upstream of the Wiens, employing a 2D single-wound field map, with the remaining MFX solenoids used as a counter-wound 3D field map. The solenoid field maps for optimizations and simulations related to repairs are shown in Fig. 51. These field maps represent an improvement over the earlier-used field map used for 130 kV and 200 kV optimizations and simulations.

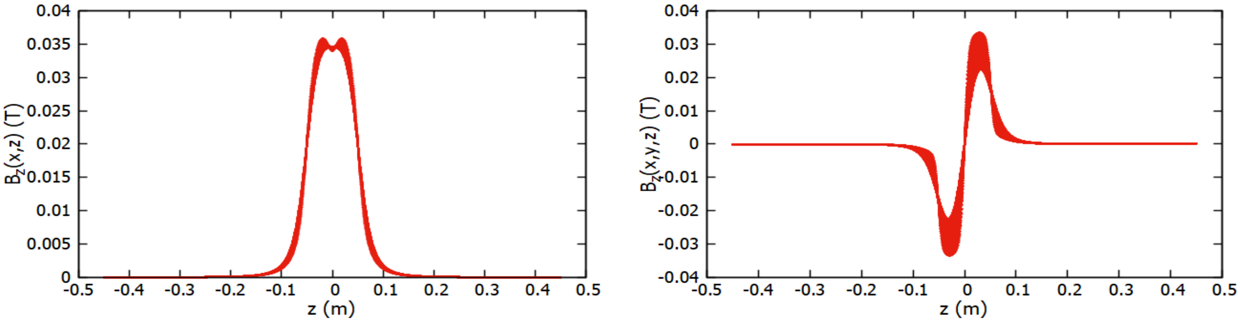

(a) Magnetic field in the single-wound MFXs. (b) Magnetic field in the counter-wound MFXs.

FIG. 51. Longitudinal electric and magnetic fields for 2D and 3D electric field maps of the solenoids at 180 kV gun voltage. (a) 2D field map of single-wound focusing solenoids (MFXs) after the DC gun, where the transverse coordinate varies from 0 to 22 mm, (b) 3D field map of three counter-wound solenoids MFXs after the chopper cavities, where the transverse coordinates vary from 0 to ±22 mm.

The *Map25D_TM_scope* was utilized for the booster (2-7 cell) SRF cavity. The longitudinal electric field of the 2.5D electric field maps used for the 2-cell and 7-cell SRF cavities is presented in Fig. 52. The optimization variables include current set points for solenoids and quadrupole settings in G-cm, RF phases (prebuncher, buncher, 2-cell, and 7-cell RF cavities), and the corresponding RF settings (GSET) that scale the respective RF field map in the CEBAF injector beamline. These variable settings are adjusted within the operational limits of the CEBAF injector.

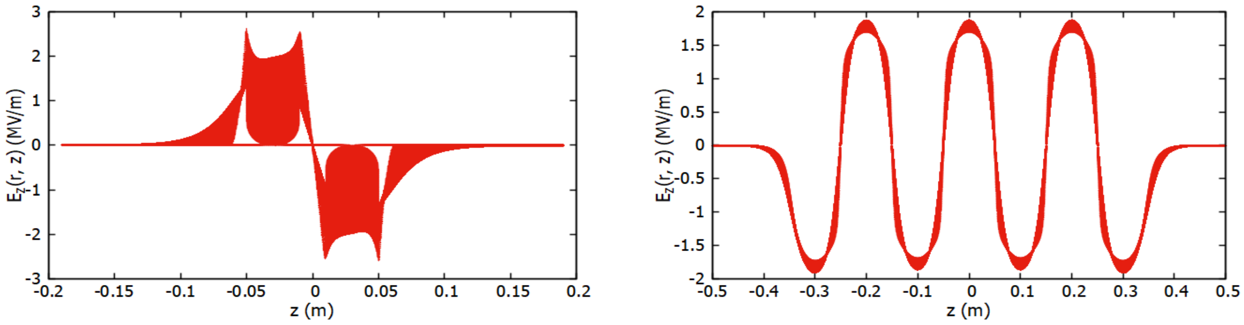

(a) Electric field in the 2-cell cavity.

(b) Electric field in the 7-cell cavity.

FIG. 52. Longitudinal electric fields for the booster at 180 kV gun voltage: (a) 2.5D electric field maps of a 2-cell SRF cavity, (b) 2.5D electric field map of a 7-cell SRF cavity. In both field maps, radial coordinates vary from 0 to 25 mm.

The injector beamline contains 12 solenoids, including spin solenoids MFGs set for 0°, and 12 quadrupoles for transverse focusing, excluding the 4 Wien quads. These elements are integrated into the injector General Particle Tracer (GPT) [64] model, while inactive elements such as correctors and beam monitor devices are represented as drift spaces. The 15-degree bend dipole is modeled as a straight drift space, and Wiens are set to OFF, with corresponding quads also set to OFF, along with the chopper cavity modeled as a straight drift. The beamline used for optimizations and simulations extends from the gun to a point just before the first full cryomodule, located 30.0 meters away from the gun.

The initial distributions for the 180 kV optimizations and simulations of the electron bunch are identical to those for the 130 kV Gaussian distribution in t, x, y, p_x, and p_y. However, the laser spot size is $\sigma_x = \sigma_y = 0.50$ mm, with a laser pulse length of 50 ps FWHM, and an energy spread of $\sigma_{\beta\gamma} = 2.45 \times 10^{-4}$. The normalized rms transverse emittance at the cathode is given by Eq. (116) and is 0.12255 mm mrad. The space charge effect is incorporated using the *spacecharge3Dmesh* [65, 66] scheme. For the injector optimizations, we employed the multi-objective global optimizer (GDFMGO) [74], which is the Non-dominated Sorting Genetic Algorithm (NSGA-II) [75] implemented in GPT. The optimization process utilized a $\mathrm{K_L}$ bunch charge of 0.64 pC, a beam current of 320 µA, and a drive laser frequency of 499 MHz at 180 kV gun for a simulation with 250 macroparticles.

TABLE 6. Optimization goals upstream of the first full cryomodule (28.35 m downstream from the gun) for the CEBAF injector. It is important to note that the specified minimum and maximum values are not rigid constraints but rather indicative parameters defining the desired objective space range.

Objectives	Minimum	Maximum	Unit	Order
transverse emittances (ϵ_{nx}, ϵ_{ny})	–	0.25	mm mrad	10^{-6}
bunch length (σ_z)	–	0.50	ps	10^{-12}
Kinetic energy (E_k)	4.5	8.0	MeV	10^{6}
Energy Spread (σ_{E_k})	–	75	keV	10^{3}
Beam Transmission	99.9	100	%	1

The optimizations included 28 variables, such as magnetic elements and RF settings, and 62 objectives and constraints related to beam transmission, bunch lengths, and normalized transverse emittance at different locations in the beamlines. The optimization goal at the end of the CEBAF injector upstreams of the first full cryomodules is summarized in Table 6.

A population size of 120 with 1000 generations was employed for 120,000 runs, resulting in 120 sets of optimal settings for magnetic elements and RF settings. It is ensured that there is a much higher kinetic energy, approximately 300 keV, going from the 2-cell cavity to the 7-cell cavity in the booster. The optimizations were performed using the Jefferson Lab ifarm high-performance computing.

TABLE 7. Convergence test at the optimized (magnet and RF) settings.

Numpar	Transmssion (%)	σ_z (ps)	ϵ_{nx}, ϵ_{ny} (mm mrad)	σ_x, σ_y (mm)	$\sigma_{\mathrm{E_k}}$ (keV)
250	98.80	0.2761	0.2264, 0.2309	0.3645, 0.3848	43.20
2500	98.32	0.2754	0.2982, 0.2747	0.4539, 0.4279	49.86
5000	98.18	0.2799	0.2952, 0.2770	0.4486, 0.4293	51.10
10000	98.40	0.2810	0.3118, 0.2868	0.4609, 0.4345	51.36
12000	98.20	0.2820	0.3014, 0.2784	0.4566, 0.4284	51.46

After completing the optimization, an effort was made to enhance the accuracy of the simulated space charge effects and capture any nuanced responses to the optimized setup. The optimal settings underwent evaluation by increasing the number of macroparticles used in the optimization process. However, this augmentation in macroparticles led to the deterioration of beam characteristics, including bunch lengths, transverse beam sizes, emittances, and beam transmission achieved during the optimization. The simulations in the optimization phase were initially conducted with 250 macroparticles, and the results were cross-validated with simulations using 2500, 5000, 10000, and 12000 macroparticles. The augmentation in macroparticles enhances the precision of calculated space charge effects and reveals subtle responses to the setups identified by optimization. However, it is observed that beam characteristics, such as bunch length and transmission achieved during optimization, typically fluctuate slightly with an increased number of macroparticles, as indicated in Table 7. Therefore, we used 10,000 macroparticles in all simulations where the beam characteristics are converged.

TABLE 8. CEBAF beam specifications/requirements for simultaneous operation of four experiment halls at Jefferson Lab.

Halls/ Experiment	Frequency Rate (MHz)	Avg. Beam Current (µA)	Bunch Charge (pC)	bunch spacing (ns)
Hall A (MOLLER)	249.5	65	0.26	4
Hall B	249.5	0.5	0.002	4
Hall C	249.5	35	0.12	4
Hall D (K_L baseline)	15.6	5	0.32	64
Hall D (K_L goal)	7.80	5	0.64	128

Table 8 provides details about concurrent experiments running alongside the K_L experiment in various experimental halls, including average beam currents, repetition rates, and charge per bunch. For seamless CEBAF operations, it is imperative to simultaneously transmit both high and low-charge beams through the injector, employing the same optics. To address the diverse beam requirements of different halls, computer modeling is employed to determine optimal settings for magnetic elements (solenoids and quads) and RF systems. These settings play a crucial role in ensuring efficient transmission of both low and high-charge beams through the injector, optimizing the overall performance of the CEBAF facility.

Simulations were conducted on the optimized settings obtained from GPT optimizations to assess beam parameters for different bunch charges required for concurrent operation in four halls at CEBAF. Out of the 120 optimal settings from the GPT optimizations of magnetic elements and RF systems, one optimal solution on the Pareto front was selected for the injector's simulation based on external constraints. The selection criteria included achieving beam transmission greater than 90%, normalized transverse emittance less than 1 mm mrad, and a bunch length less than 1.0 ps upstream of the first full cryomodules. These criteria represent acceptable beam characteristics for the CEBAF injector operation.

The beam dynamics simulation was conducted for different charge per bunch scenarios, and the analysis of the simulation results yields insights into beam characteristics. In Fig. 53, the variation of bunch length along the beamline is illustrated for different charge per bunch values corresponding to different experimental halls. The findings reveal that, irrespective of the charge per bunch, the bunch length remains below 0.5 ps upstream of the first full modules.

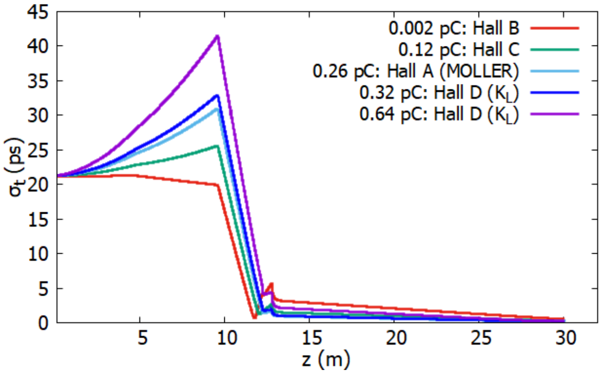

FIG. 53. Bunch length (σ_t) along the beamline at 180 kV voltage for different values of bunch charge.

The simulated average kinetic energy of the beam remains nearly constant at approximately 6.68 MeV for all charge scenarios. The energy spread for each charge case is less than 0.01. Figure 54 illustrates the average kinetic energy and energy spread for various charge per bunch values.

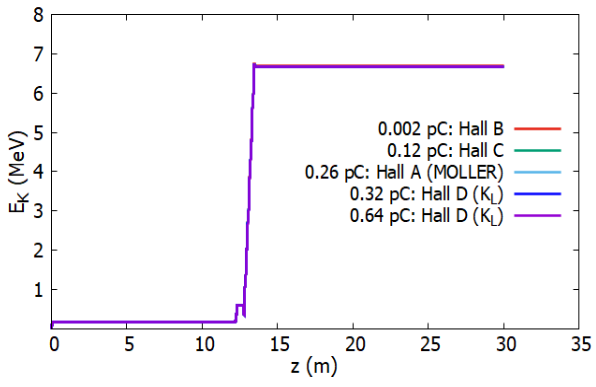

(a) Average kinetic energy.
(b) Energy spread.

FIG. 54. Average kinetic energy and energy spread for different bunch charge along the CEBAF injector beamline at 180 kV gun voltage. (a) Average kinetic energy and (b) Energy spread $\sigma_{E_\mathrm{k}}/E_\mathrm{k}$.

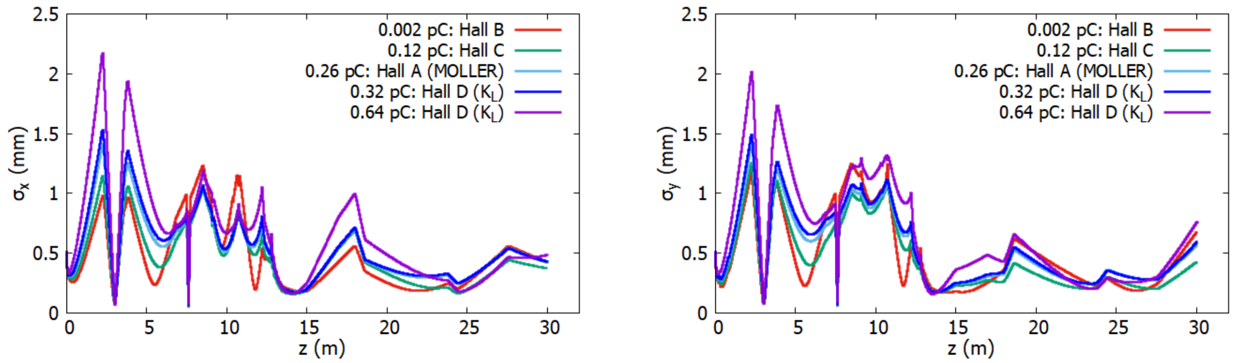

FIG. 55. Transverse beam sizes for different bunch charges at 180 kV gun voltage: horizontal (σ_x)(left) and vertical (σ_y) (right).

Figures 55 and 56 illustrate the simulation outcomes, portraying the variations in transverse beam sizes and normalized transverse emittances, respectively, along the injector beamline for different bunch charge values. The results suggest minimal fluctuations in the beam sizes and transverse emittances of the electron beam with varying charge per bunch along the injector beamline. These values remain within the operational limits of the injector. The simulation results thus indicate that the high charge K_L can run simultaneously with lower charge beam delivered to the other halls.

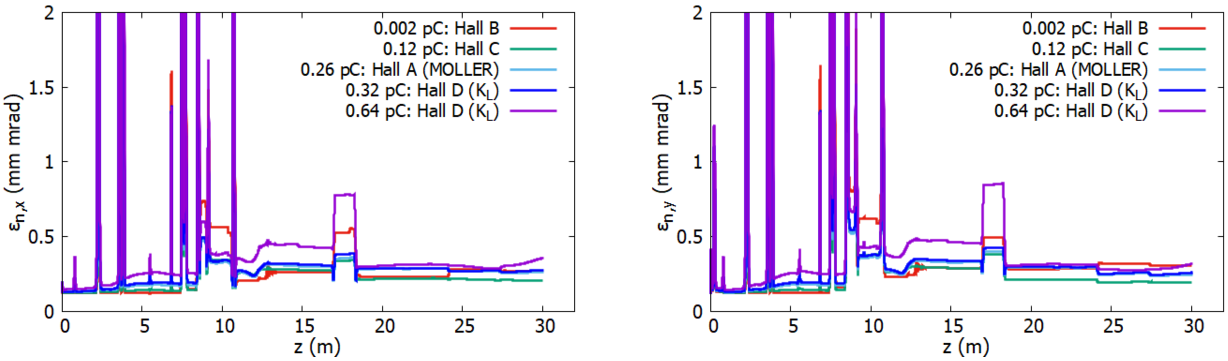

FIG. 56. Normalized transverse emittances for different bunch charges at 180 kV gun voltage: horizontal($\epsilon_{n,x}$) (left) and vertical ($\epsilon_{n,y}$)(right).

Figure 57 illustrates the simulated beam transmission along the beamline for different bunch charges, showcasing that the transmission exceeds 98% for all charge scenarios.

Before SAD 2023, the laser spot size for all lasers was approximately 0.55 mm. However, there is a variation in laser spot size after SAD 2023, and it differs for different drive lasers (A, B, C, D). Additionally, different drive laser frequencies result in different pulse lengths-lower frequencies correspond to larger pulse lengths and vice versa. Therefore, we investigated the transmission as a function of the photocathode laser spot size and pulse length, assessing the sensitivity of simulation results to these parameters. In the simulations, we adjusted the laser spot size while keeping the laser pulse length constant and vice versa. Figure 58 illustrates the beam transmission through the injector, demonstrating the variation in laser spot size and pulse length at the cathode for a 0.64 pC, 128 ns beam for the K_L bunch charge at 180 kV. The figure shows that the transmission is not significantly sensitive to changes in beam size and pulse length, with reference values of laser spot size at 0.50 mm and laser pulse length of 50 ps FWHM. With the optimized setting present in the CEBAF injector,

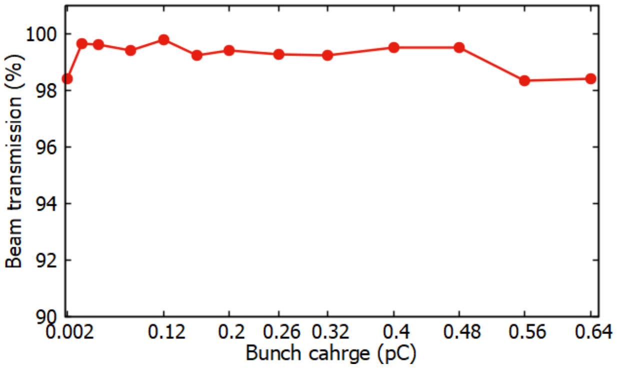

FIG. 57. Beam transmission through the apertures for various bunch charge at 180 kV gun voltage.

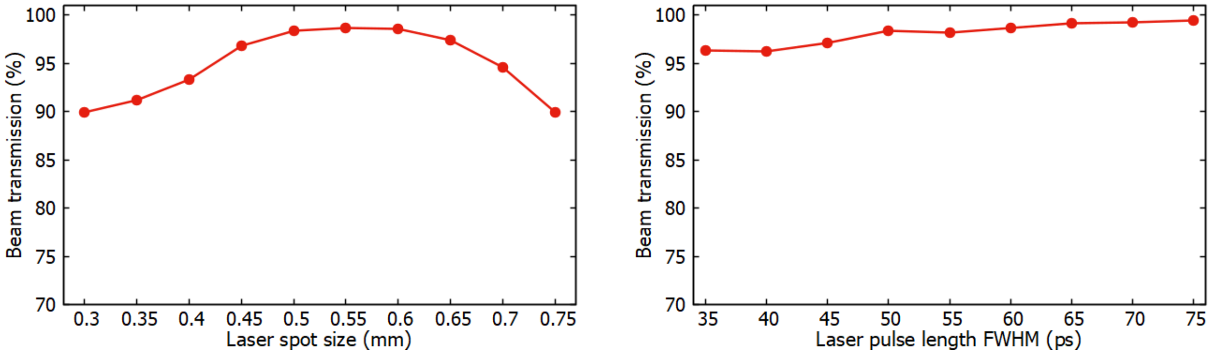

(a) Beam transmission versus laser spot size. (b) Beam transmission versus laser pulse length.

FIG. 58. Simulated beam transmission with variation of laser spot size and laser pulse length for 0.64 pC at 180 kV gun voltage. (a) Laser spot size at the cathode. (b) Laser pulse length at the cathode.

all beam conditions should transmit greater than 90% beam.

5.4 CEBAF INJECTOR AT 140 kV DC GUN VOLTAGE

For the CEBAF injector, the current DC gun voltage is set at 140 kV. At this specific gun voltage, a comprehensive series of beam transmission and bunch length expansion measurements were thoroughly conducted with Wien filters OFF. These measurements utilized the K_L laser operating at 15.6 MHz. The primary objective of this experimental endeavor was to carefully examine and evaluate the response of the K_L laser under these conditions. The focus was on assessing its capability to generate a well-suited bunch structure while simultaneously determining the optimal charge per bunch for the forthcoming K_L experiment. The 15.6 MHz laser allows one to produce and measure bunches with charges far beyond the 0.64 pC maximum requirement for the K_L experiment.

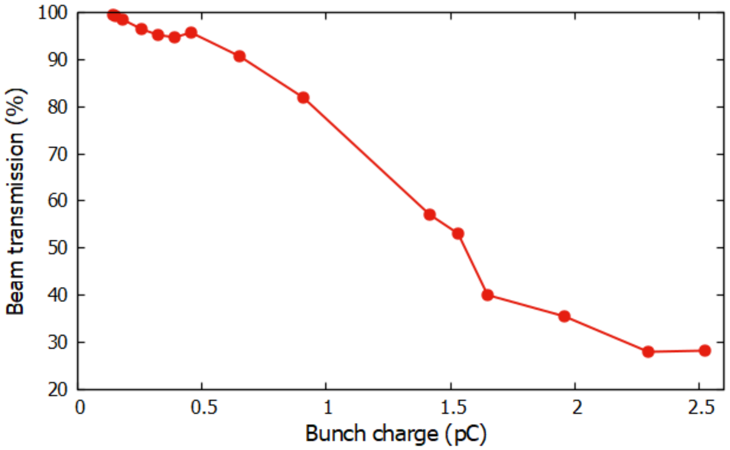

FIG. 59. The beam transmission as a function of bunch charge for K_L 15.6 MHz laser at 140 kV gun voltage.

Figure 59 illustrates the beam transmission as a function of charge per bunch from the DC gun at 140 kV for the K_L laser operating at 15.6 MHz. The graph clearly indicates that as the charge per bunch increases, there is a corresponding decrease in beam transmission. The 15.6 MHz laser effectively supplies the necessary beam current (bunch charge) required for the

$\mathrm{K_L}$ experiment. Notably, these transmission results exhibit a slight improvement compared to measurements conducted at the 130 kV DC gun. Specifically, the beam transmission for a 0.32 pC bunch charge is approximately 95%, and for a 0.64 pC bunch charge, it dips only slightly below 90%. This observation underscores the reliability of the 15.6 MHz laser in consistently delivering the necessary current for the $\mathrm{K_L}$ experiment.

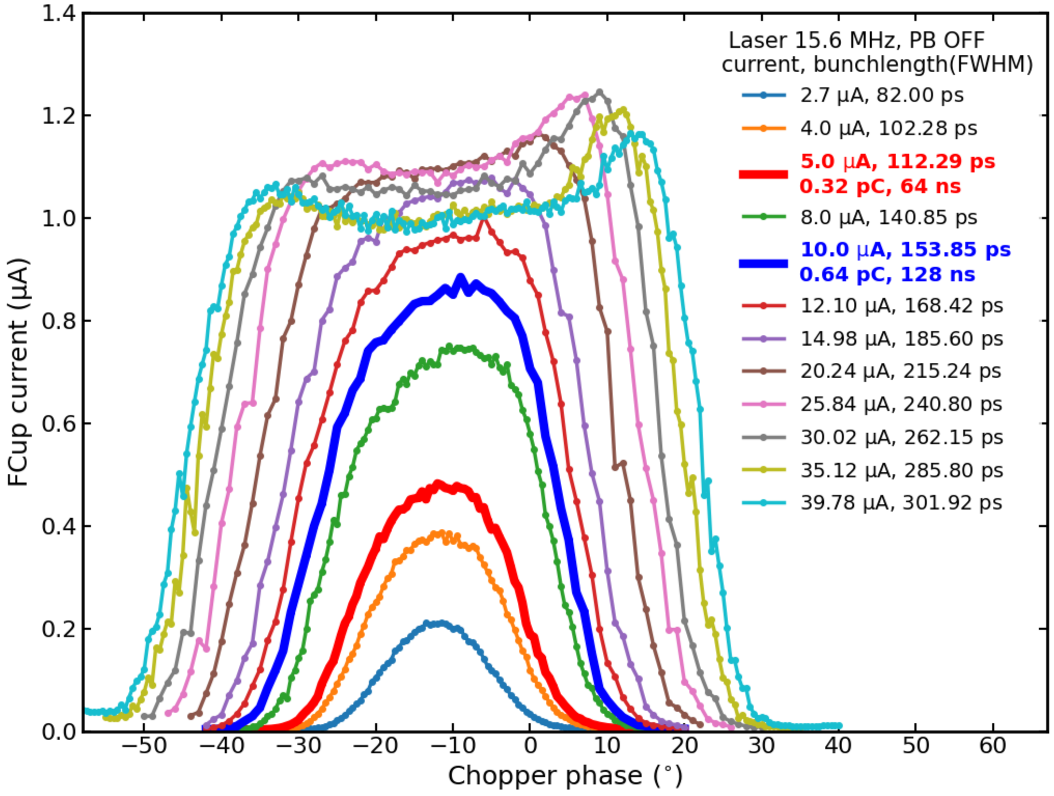

FIG. 60. Electron bunch length measurement using RF chopper cavity for 15.6 MHz laser at 140 kV. The gun current was varied from 2.0 μA to 40.0 μA.

The longitudinal bunch profile and corresponding bunch length at the location of the chopper for the 15.6 MHz laser at the 140 kV DC gun are depicted in Fig. 60. At lower charges, the longitudinal profile of the bunch at the chopper location appears Gaussian. However, as the charge per bunch increases, the distribution transforms into a Super-Gaussian shape. The trend in the increase of bunch length and variations in the longitudinal bunch profile closely mirrors the observations discussed in Section 5.2.2 for the 130 kV experiments. In comparison to the results at 130 kV, the bunch length is approximately 12% smaller at 140 kV (for a 0.64 pC bunch charge) due to reduced space charge. This observation maintains consistency with the findings at 130 kV.

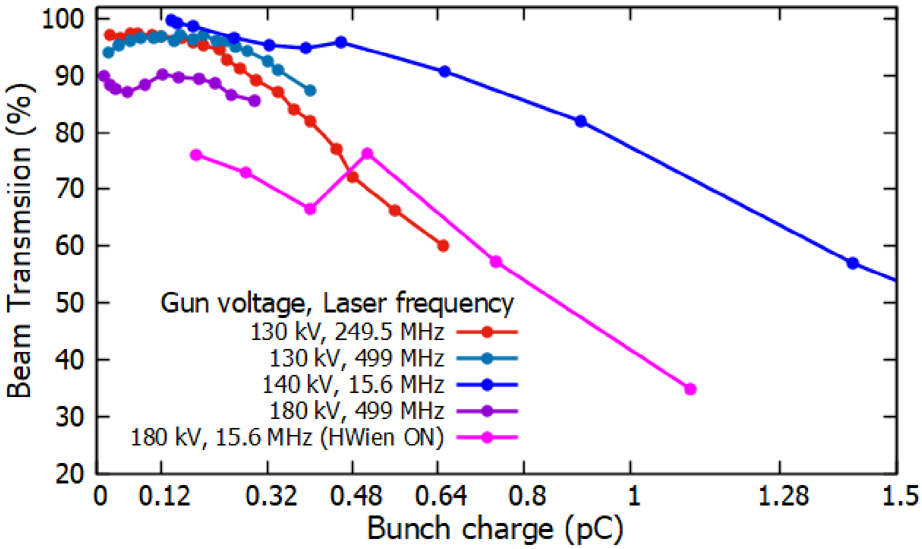

FIG. 61. Comparison of beam transmission measurements as a function of charge per bunch at 130 kV, 140 kV, and 180 kV DC gun voltages.

The beam transmission measurements, spanning from 130 kV to 180 kV, with spin flipper both OFF and ON for different laser drive frequencies (15.6 MHz K_L laser, 249.5 MHz, and 499 MHz lasers), are illustrated in Fig. 61. The figure demonstrates variations in beam transmission with different gun voltages and spin flipper states. Upon examining the beam study measurements and Fig. 61, it becomes evident that the 249.5 MHz and 499 MHz lasers were unable to provide sufficient beam current (bunch charge) required for the K_L experiment at all voltages. In contrast, the 15.6 MHz laser consistently delivered the necessary bunch charge for both the baseline (0.32 pC) and goal (0.64 pC) of the $\mathrm{K_L}$ experiment. Notably, the power amplification required for the 249.5 MHz and 499 MHz lasers at 130 kV operation is effectively provided by the new $\mathrm{K_L}$ laser operating at 15.6 MHz.

5.5 CEBAF INJECTOR AT 200 kV DC GUN VOLTAGE

There are ongoing efforts to transition the gun voltages from 130 kV to 200 kV for the CEBAF injector. And also $\mathrm{K_L}$ experiment will run at 200 kV DC gun voltage in the CEBAF Phase 2 upgrade injector beamline. The schematic of the upgraded injector layout for 200 kV optimizations and the simulation is depicted in Fig. 62. Additionally, the injector beamline elements, starting from the cathode, including magnetic elements, are detailed in Table 4.

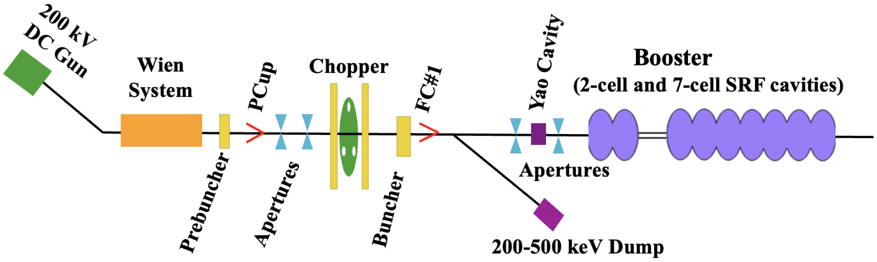

FIG. 62. CEBAF injector upgrade Phase 2 layout for 200 kV DC gun voltage. It displays the section of the injector that extends from the gun to downstream of the booster. The injector layouts are not to scale, and magnet elements are not shown. PCup, and FC#1 are insertable Faraday cups.

5.5.1 INJECTOR OPTIMIZATION AND SIMULATION AT 200 kV DC GUN

As carried out for 180 kV, Multi-Objective Genetic Optimization (MGO) was utilized to determine the necessary magnetic elements and RF settings for the $\mathrm{K_L}$ bunch charge (0.64 pC) at 200 kV. The GPT model of the CEBAF injector at a 200 kV DC gun employs the same field maps for the gun, solenoids, and prebuncher and buncher as used in the 130 kV configuration (see Fig. 28). The field map for the booster is the same as used for 180 kV (see Fig. 52). The optimization goal at the end of the CEBAF injector upstream of the first full cryomodules is summarized in Table 6.

The initial distributions for the 200 kV optimizations and simulations of the electron bunch are the same as those at 130 kV, including the same laser pulse length and laser spot size at the cathode. Initially, the optimizations and beam dynamics particle tracking simulations were performed with the Wien filter turned OFF.

The beam dynamics simulation explored various scenarios with different charge per bunch settings, providing valuable insights into beam characteristics. The simulated average beam kinetic energy remains nearly constant at approximately 6.98 MeV for all charge scenarios. Figure 63 visually represents the change in bunch length and energy spread for various charge per bunch values at different locations along the beamline corresponding to distinct experimental halls. The results consistently indicate that, regardless of the specific charge per bunch, the bunch length remains below 1.1 ps upstream of the full modules, and the energy spread for each charge case is approximately 0.02 or less.

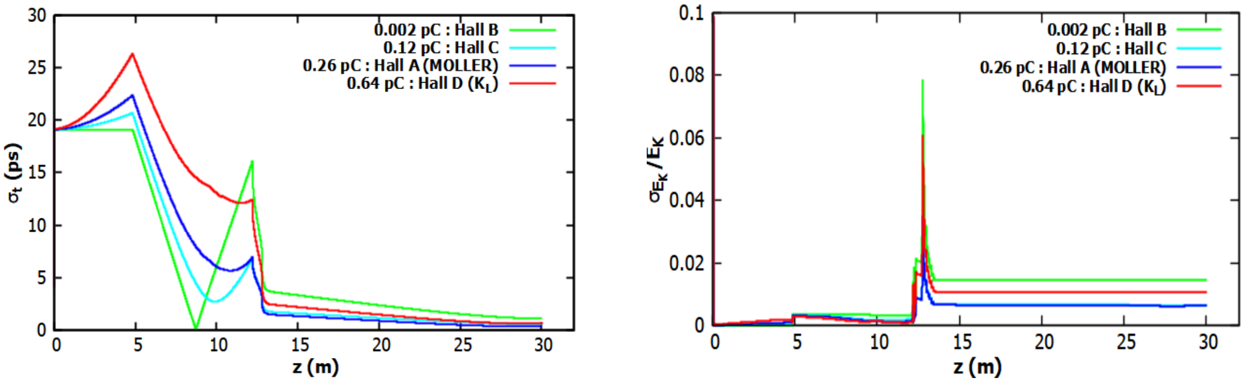

(a) Bunch length *rms*.

(b) Energy spread.

FIG. 63. Evolution of bunch length (σ_t) and energy spread ($\sigma_{\mathrm{E_k}}/\mathrm{E_k}$) along the beamline with Wiens OFF at 200 kV gun voltage for different values of bunch charge. (a) Bunch length (σ_t) and (b) Energy spread $\sigma_{\mathrm{E_k}}/\mathrm{E_k}$.

Simulated beam transmission along the beamline for different bunch charges is illustrated in Fig. 64, highlighting that the transmission exceeds 94.4% for all charge scenarios.

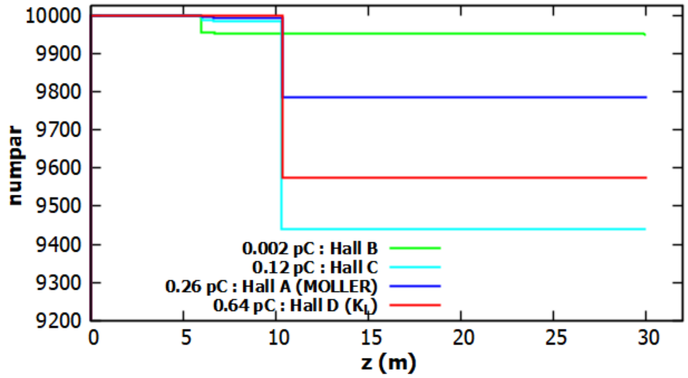

FIG. 64. Beam transmission through the apertures for various bunch charge at 200 kV gun voltage.

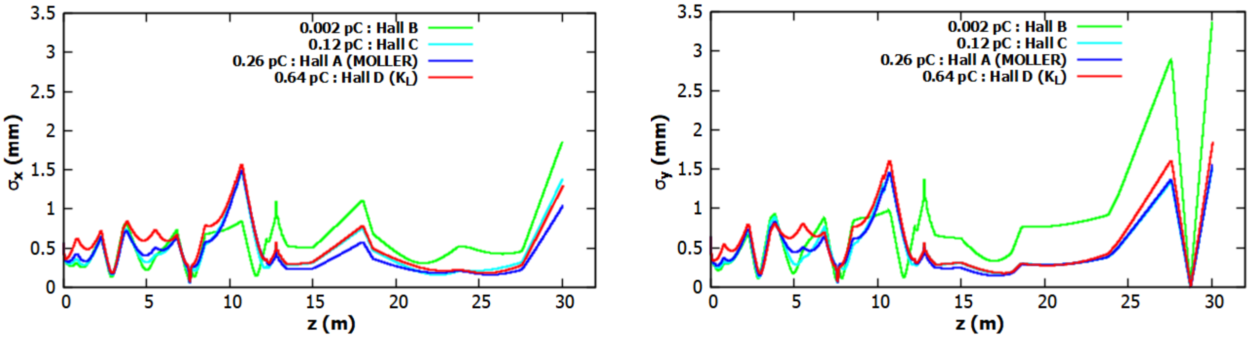

FIG. 65. Transverse beam sizes for different bunch charges at 200 kV gun voltage: horizontal (σ_x)(left) and vertical (σ_y) (right).

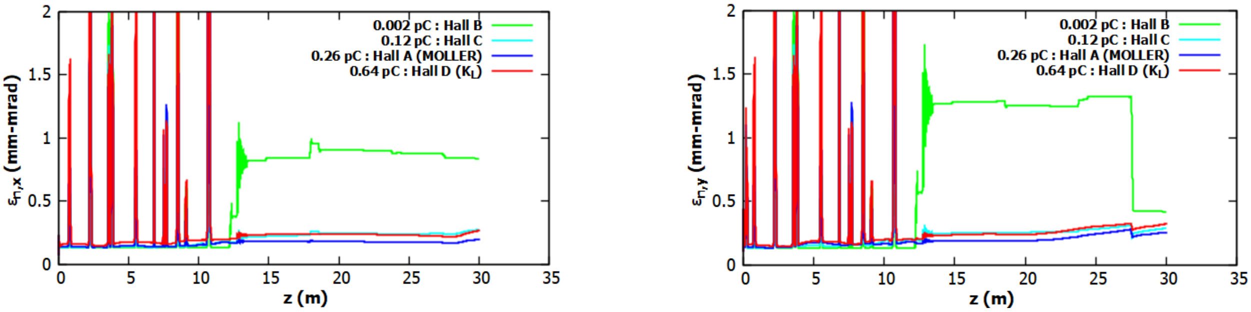

FIG. 66. Normalized transverse emittances for different charges at a 200 kV gun voltage: horizontal ($\epsilon_{n,x}$) (left) and vertical ($\epsilon_{n,y}$) (right).

Figures 65 and 66 present the simulation results, depicting changes in transverse beam sizes and normalized transverse emittances along the injector beamline for different bunch charge values. The findings indicate minimal variations in both beam sizes and transverse emittances of the electron beam as the charge per bunch varies along the injector beamline. The beam size and normalized variation are more pronounced for very low charge compared to high charge, as the optimizations are performed for high $\mathrm{K_L}$ bunch charge. However, these values consistently remain within the operational limits of the injector.

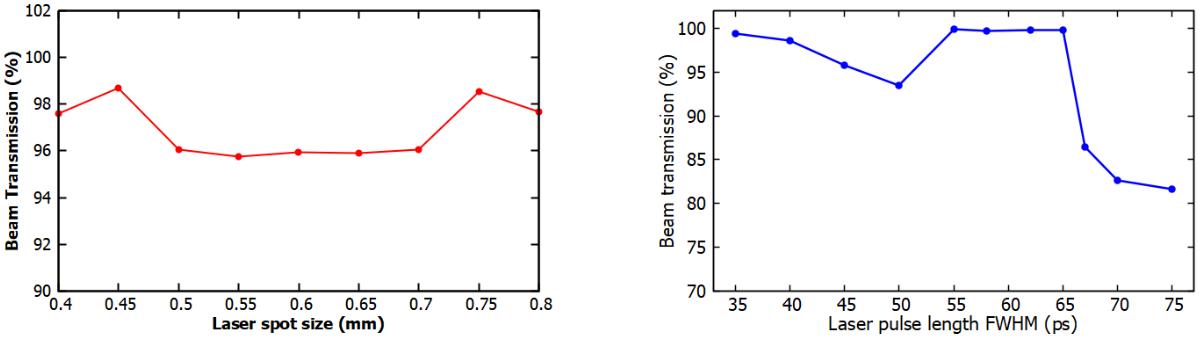

(a) Beam transmission vs. laser spot size.

(b) Beam transmission vs. laser pulse length.

FIG. 67. Simulated beam transmission with variation of laser spot size and laser pulse length for 0.64 pC at 200 kV gun voltage. (a) Laser spot size, (b) Laser pulse length at the cathode.

We also examined the transmission as a function of the photocathode laser spot size and pulse length. In the simulation, we adjusted the laser spot size while maintaining a constant laser pulse length, and vice versa. Figure 67 illustrates the beam transmission through the injector, showcasing the variation in laser spot size and laser pulse length at the cathode for a 0.64 pC, 128 ns beam for the $\mathrm{K_L}$ bunch charge at 200 kV.

As previously mentioned, the $\mathrm{K_L}$ experiment has distinctive beam requirements, characterized by a notably low bunch repetition rate and an unusually high bunch charge. Additionally, the CEBAF injector demands a high-quality beam for experiments like the Measurement of a Lepton-Lepton Electroweak Reaction (MOLLER). Following the completion of optimizations and simulations with the spin flipper turned off (Wiens OFF and spin-flipping solenoids set at zero degrees), and using the same optimized settings for magnetic elements and RF amplitude and phases, we conducted simulations encompassing a range of bunch charge beams, spanning from low to high specifications. These simulations considered concurrent operations across all four Halls at CEBAF, with the spin flipper ON at 200 kV. The results obtained with the spin flipper ON were then compared with the previous simulation results with the spin flipper OFF.

A Wien filter is a device characterized by static electric and magnetic fields arranged orthogonally to induce a net spin rotation without altering the trajectory of the beam. Within the CEBAF injector, there are two Wien filter systems [14, 76]. Each system is accompanied by two spin flipper solenoid magnets positioned in between them to achieve the required spin orientations for the experimental target, as depicted in Fig. 68. The polarization of the electron beam, originating from the photocathode, is initially longitudinal. The first Wien filter, located downstream of the DC photo-gun, is oriented vertically and facilitates the rotation of polarization from longitudinal to vertical. Subsequently, the second Wien filter, oriented horizontally, rotates the polarizations in-plane to counteract the precession induced by CEBAF transport magnets. The solenoids placed between these filters ensure additional polarization rotations.

In the laboratory frame, the Thomas-BMT equation [77, 78] describes the spin precession of a relativistic particle in an external electromagnetic field. For the CEBAF spin rotator, the expression for spin precession relative to the electron momentum is derived using the Thomas-BMT equations:

$$\frac{d\mathbf{S}}{dt} = \Delta\boldsymbol{\Omega} \times \mathbf{S}, \qquad \Delta\boldsymbol{\Omega} = \boldsymbol{\Omega}_s - \boldsymbol{\Omega}_{mom}. \tag{120}$$

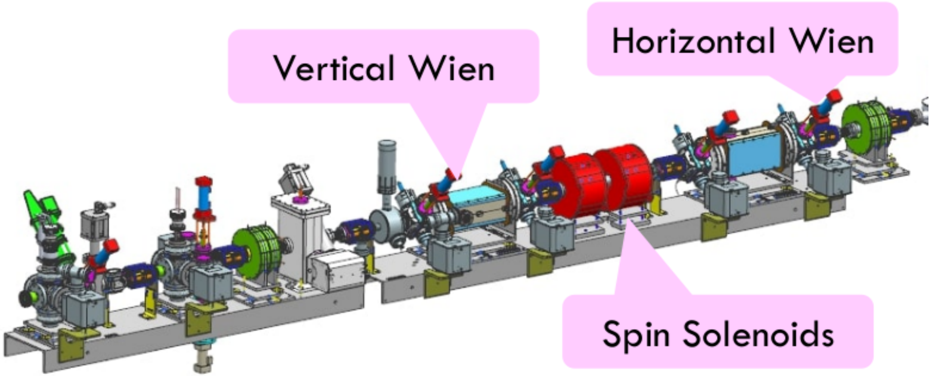

FIG. 68. A schematic of the spin flipper setup in the CEBAF injector. It comprises the Wien system and spin-flipping solenoids.

Here, $\boldsymbol{\Delta\Omega}$ represents the spin precession frequency and is defined as:

$$\boldsymbol{\Delta\Omega} = -\frac{q}{m}\left[a\mathbf{B}_{\perp} + \frac{1}{\gamma}(1+a)\mathbf{B}_{\parallel} - \left(a - \frac{1}{\gamma^2 - 1}\right)\frac{\boldsymbol{\beta}\times\mathbf{E}}{c}\right]. \tag{121}$$

In Eq. (121), $\mathbf{S}$ denotes the spin vector of the particle in the rest frame, while $\mathbf{B}_{\perp}$ and $\mathbf{B}_{\parallel}$ represent the transverse and longitudinal components of the magnetic field in the laboratory frame relative to the velocity $\boldsymbol{\beta}c$ of the particle. The Lorentz factor is denoted by $\gamma = (1-\beta^2)^{-1/2}$. The electric field is represented by $\mathbf{E}$, and $a = (g-2)/2$ designates the anomalous gyromagnetic g-factor. For an electron with $q = -e$, the spin precessions in the Wien and solenoid configurations are expressed as:

$$\text{Spin Precession in Wien: } \boldsymbol{\Delta\Omega} = \frac{e}{m}\left[a\mathbf{B}_{\perp} + \left(\frac{1}{\gamma^2 - 1} - a\right)\frac{\boldsymbol{\beta}\times\mathbf{E}}{c}\right], \tag{122}$$

$$\text{Spin Precession in Solenoid: } \boldsymbol{\Delta\Omega} = \frac{e}{m}\left[\frac{1}{\gamma}(1+a)\mathbf{B}_{\parallel}\right]. \tag{123}$$

The spin precession frequency, denoted as $\Delta\Omega$, and the corresponding spin rotation angle, represented by θ, are linked by the equation $\theta = \Delta\Omega T$, where $T = L_{\text{eff}}/(\beta c)$ and L_{eff} signifies the effective length of the spin flipper. In the Wien system, the electric field magnitude perpendicular to the particle velocity $v_z = \beta c$ is denoted by $E_{x,y}$. Longitudinal fields, as found in solenoids, are confined to the injector and part of the Wien filter system. The remaining injector solenoids are intentionally designed to be counter-wound, featuring two alternating reversed loops, providing focusing while resulting in a net zero spin precession. Figure 68 illustrates a schematic of the system employed at CEBAF.

For the Wien filter to function as a spin rotator, maintaining the trajectory of particles passing through the device is crucial. In the single-particle model, this is accomplished by ensuring that the contributions of the electric and magnetic fields to the total force are zero, thus satisfying the so-called "Wien condition":

$$E_y = -v_z B_x. \tag{124}$$

Here, E_y denotes the vertical electric field, while B_x represents the horizontal magnetic field specific to the vertical Wien filter. For the horizontal Wien filter, the roles of the electric and magnetic fields are swapped. Applying this mathematical framework facilitates the determination of electric and magnetic field magnitudes required to achieve the desired spin rotation angle, applicable for operations within the range of -100° to + 100° for a 200 keV electron. For the earlier 200 kV simulations, the spin flipper OFF conditions initially involve turning off the vertical Wien (VWien) and configuring the spin-flipper solenoids, namely MFG1I04A and MFG1I04B, with $\sum$FGs =0°. Subsequently, in simulations with the spin flipper ON, VWien is activated to $\mp$ 90° for left or right spin-flipping, and the spin flipper solenoid conditions are set with $\sum$FGs= 90°. The combined effects of the Wien system and spin-flipping solenoid result in either flipping the spin orientations of the electron beam to the left or right. Additionally, with the spin flipper ON, the VWien quads MQW1I03 and MQW1I04 are utilized for focusing the spin-rotated beam.

TABLE 9. Simulated beam characteristics upstream of the first full cryomodule with spin flipper OFF.

Beam Characteristics	**Bunch Charge Specifications**				
	2 fC	0.12 pC	0.26 pC	0.32 pC	0.64 pC
beam transmission (%)	99.52	94.40	97.84	99.28	95.75
bunch length (ps)	1.12	0.55	0.37	0.38	0.67
ϵ_{nx}, ϵ_{ny} (mm mrad)	0.84, 0.42	0.27, 0.29	0.20, 0.25	0.21, 0.29	0.26, 0.32
σ_x, σ_y (mm)	1.86, 3.36	1.39, 1.53	1.04, 1.55	1.08, 1.68	1.30, 1.85
$\frac{\sigma_{\mathrm{E_k}}}{\mathrm{E_k}}$ (%)	1.40	0.65	0.63	0.69	1.04

Table 9 presents the simulated beam characteristics of the CEBAF injector upstream of the first full cryomodules with the spin flipper OFF. The results demonstrate that the bunch length consistently remains below 1.1 ps upstream of the full modules, regardless of the charge per bunch. The energy spread for all charge cases is approximately 1.4% or less. Additionally, the beam transmission along the beamline for different bunch charges indicates that the transmission exceeds 94.4% for all charges. The normalized emittance is less than 0.85 mm mrad for all charge configurations. It is worth noting that the average beam kinetic energy remains almost constant at around 6.98 MeV for all charge cases and spin OFF and ON scenarios, although this information is not explicitly shown in the table.

TABLE 10. Simulated beam characteristics upstream of the first full cryomodule with spin flipper ON.

Beam Characteristics	**Bunch Charge Specifications**				
	2 fC	0.12 pC	0.26 pC	0.32 pC	0.64 pC
beam transmission (%)	99.95	96.61	99.93	97.96	99.89
bunch length (ps)	1.21	0.63	0.38	0.37	0.70
ϵ_{nx}, ϵ_{ny} (mm mrad)	0.78, 0.32	0.29, 0.29	0.27, 0.29	0.23, 0.27	0.35, 0.42
σ_x, σ_y (mm)	1.70, 2.53	1.29, 1.52	1.08, 1.58	0.96, 1.53	1.23, 2.07
$\frac{\sigma_{\mathrm{E_k}}}{\mathrm{E_k}}$ (%)	1.50	0.70	0.67	0.74	1.16

Table 10 illustrates the simulated beam characteristics of the CEBAF injector upstream of the first full cryomodules with the spin flipper ON. No significant differences are observed in the beam characteristics between spin flip left and right. The results reveal that the bunch length consistently remains below 1.21 ps upstream of the full modules, irrespective of the charge per bunch. The energy spread for all charge cases is approximately 1.5% or less. Furthermore, the beam transmission along the beamline for different bunch charges indicates that the transmission exceeds 96.61% for all charges. The normalized emittance is less than 0.78 mm mrad for all charge configurations.

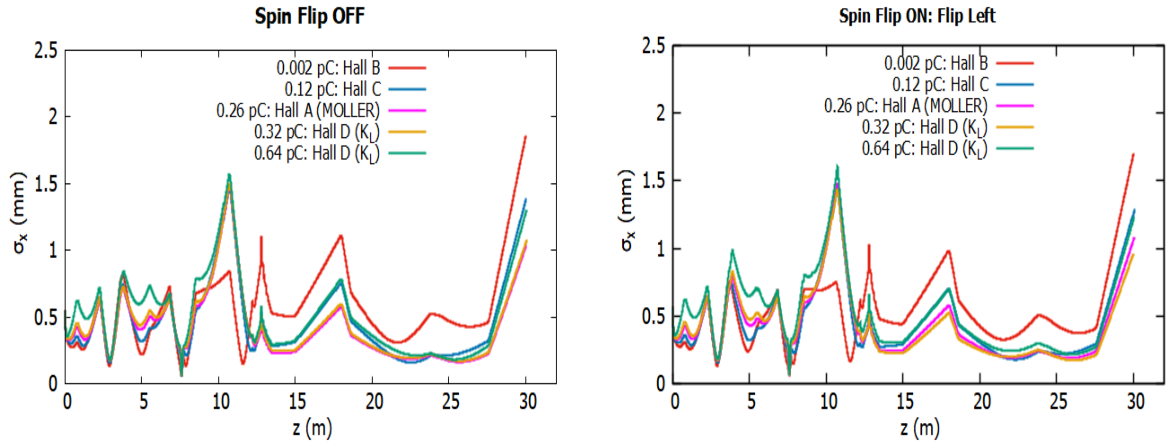

(a) Horizontal beam size (σ_x) with spin flipper OFF.

(b) Horizontal beam size (σ_x) with spin flipper ON.

FIG. 69. Horizontal beam sizes for different bunch charge specifications along the CEBAF injector beamline. (a) Spin flipper OFF. (b) Spin flipper ON.

We also conducted a comparison of the evolution of beam characteristics and transmission with the spin flipper both ON and OFF along the CEBAF injector beamline. Figure 69 illustrates the variation in horizontal beam sizes along the beamline for different charge per bunch values in various experimental halls with both spin ON and OFF. The variations in bunch length and energy spread along the beamline for different bunch charge specifications with spin flipper ON and OFF are depicted in Figs. 70 and 71, respectively. The results indicate that there is no significant difference in the beam characteristics along the beamline of the CEBAF injector with the spin flipper ON and OFF.

From the simulations, it is observed that both with spin flipper OFF and ON cases, the beam transmission and beam characteristics upstream of the first full cryomodules meet the criteria for acceptable beam performance in the context of CEBAF injector operations. At optimized settings for a high charge, simultaneous operation with Halls A, B, C, and D is

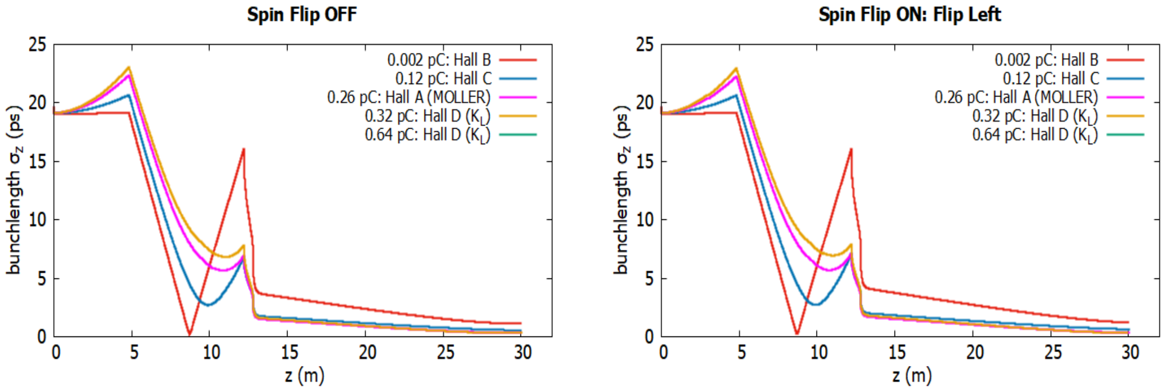

(a) Bunch length (σ_z) variation along the beamline with spin flipper OFF.

(b) Bunch length (σ_z) variation along the beamline with spin flipper ON.

FIG. 70. Bunch length variation along the beamline of the CEBAF injector for different bunch charge specifications. (a) Spin flipper OFF. (b) Spin flipper ON.

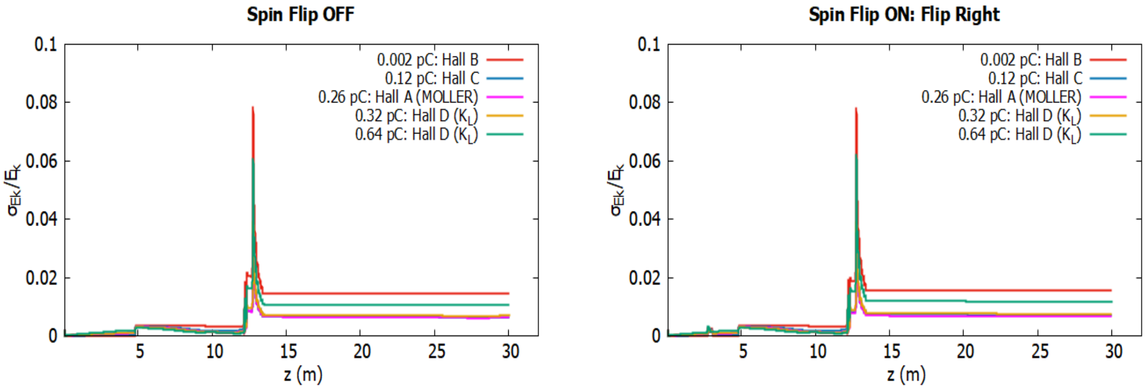

(a) Energy spread ($\sigma_{\mathrm{E_k}}/\mathrm{E_k}$) with spin flipper OFF.

(b) Energy spread ($\sigma_{\mathrm{E_k}}/\mathrm{E_k}$) with spin Flipper ON.

FIG. 71. Energy spread for different bunch charge specification along the CEBAF injector beamline. (a) Spin flipper OFF. (b) Spin flipper ON.

indicated, with minor differences in the transverse beam optics with the spin flipper OFF and ON.

5.5.2 SIMULATION RESULTS COMPARISON

After conducting a series of simulations at different gun voltages (130 kV, 180 kV, and 200 kV) for the CEBAF injector, the simulation results are compared. Figure 72 illustrates the transmission versus bunch charge at various voltages. The graph demonstrates that higher gun voltages lead to increased beam transmission; demonstrating the effectiveness of the injector to drive the K_L experiment. This is particularly advantageous due to its higher charge per bunch compared to the other experimental halls (A, B, C) at CEBAF.

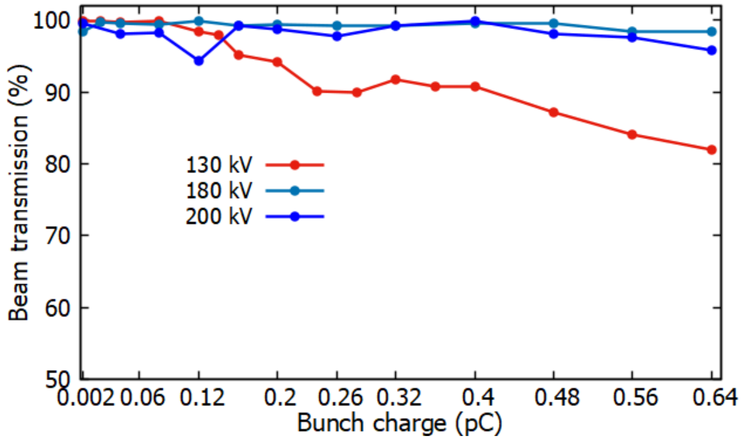

FIG. 72. Beam transmission as a function of bunch charge at different gun voltages in the CEBAF injector.

The GPT simulation results for bunch length expansion at 130 kV, 180 kV, and 200 kV are shown in Fig. 73. The corresponding longitudinal bunch profile at the location of the chopper is shown in Fig. 74. From Figs. 73 and 74, it is observed that an increase in gun voltages (and hence beam energy) decreases the space charge forces, resulting in improved

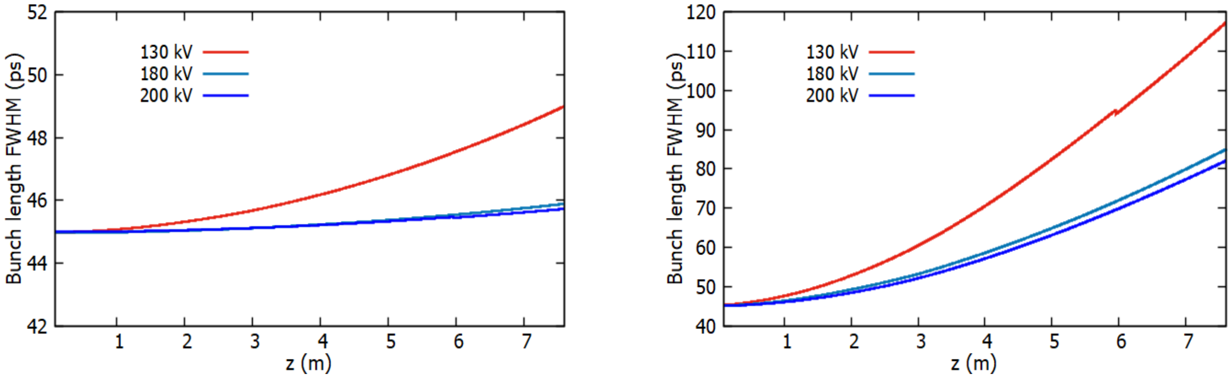

(a) Bunch length at 0.01 pC bunch charge.

(b) Bunch length at 0.64 pC bunch charge.

FIG. 73. Bunch length FWHM expansion in the CEBAF injector for low and high charge at different gun voltages (130 kV, 180 kV, and 200 kV) with the prebuncher OFF. (a) 0.01 pC bunch charge. (b) 0.64 K_L bunch charge.

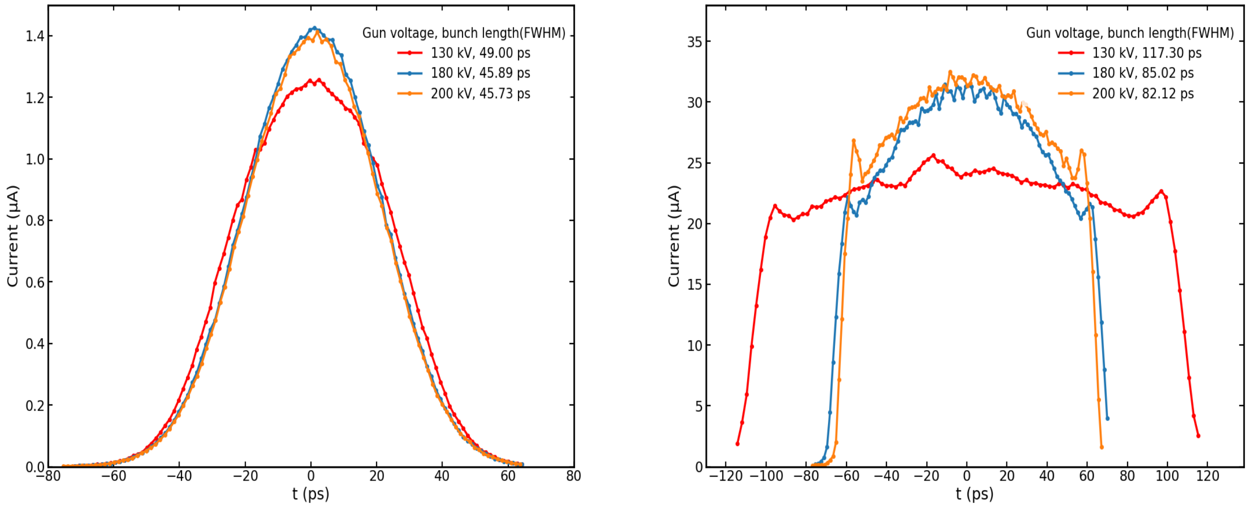

(a) Longitudinal bunch structure at 0.01 pC.

(b) Longitudinal bunch structure at 0.64 pC.

FIG. 74. Longitudinal bunch structure at the location of the chopper for low and high charge at different voltages with the prebuncher OFF. (a) For a 0.01 pC bunch charge. (b) For a 0.64 K_L bunch charge. The chopper is located 7.6 m downstream from the gun.

bunch structure and reduced bunch length for a higher charge per bunch.

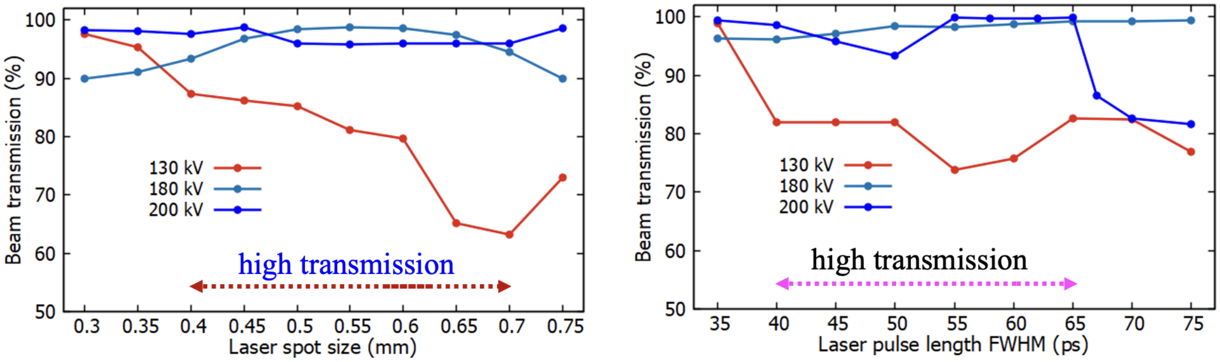

(a) Beam transmission vs. laser spot size.

(b) Beam transmission vs. laser pulse length.

FIG. 75. Simulated beam transmission with variation of laser spot size and laser pulse length at cathode for 0.64 pC at different gun voltages. (a) Laser spot size at the cathode. (b) Laser pulse length at the cathode.

The simulated beam transmission as a function of laser spot size at the cathode and the laser pulse length at the cathode for different gun voltages (130 kV, 180 kV, and 200 kV) is shown in Fig. 75. From the simulations, it is found that there is no significant change in beam transmission with variation of laser spot size and laser pulse length, particularly around the reference values of 0.50 mm laser spot size and 50 ps FWHM of the laser pulse length, for higher gun voltages of 180 kV and 200 kV.

CHAPTER 6

CONCLUSIONS AND FUTURE RESEARCH

6.1 CONCLUSIONS

In this thesis, detailed numerical and experimental studies have been conducted to investigate the dynamics of space-charge-dominated beams along with low charge per bunch beams for the CEBAF injector, utilizing the CEBAF injector beamline elements. The main objective is to develop an understanding of space-charge-dominated beams in the transport line of the CEBAF injector and to provide valuable data for the $\mathrm{K_L}$ experiment.

The primary objective of this project was to explore possibilities regarding beam transmission, transverse beam sizes, and emittances, as well as longitudinal bunch structure (bunch length and energy spread) from the CEBAF injector, specifically for conditions of the $\mathrm{K_L}$ experiment in Jefferson Lab Hall D. Additionally, simultaneous operations with other experiment halls (A, B, C) along with Hall D were considered, requiring a different bunch charge specification, lower than that of the $\mathrm{K_L}$ experiment, and potentially involving spin manipulations. We conducted a series of simulations and optimizations of beam transmission and longitudinal bunch profiles at various DC gun voltages from 130 kV to 200 kV for the CEBAF injector. In adddition corroborating measurements were taken at 130 kV, 140 kV, and 180 kV.

The initial section of the thesis presents the results of simulations, measurements, and their analysis for the 130 kV CEBAF injector Phase 1 upgrades. Beam dynamics simulations using GPT were conducted based on the measured values of the initial beam size and laser pulse length at the cathode for various charge per bunch scenarios, specifically up to for the maximum $\mathrm{K_L}$ bunch charge at 0.64 pC. Simulations considered charge per bunch conditions measured for either 249.5 or 499 MHz laser. The evolution of beam characteristics (transverse beam sizes, bunch lengths, normalized *rms* emittances, beam transmission, energy spread) in the CEBAF injector from the DC gun to the upstream of the first cryomodules was examined. The results of beam transmission and longitudinal bunch profile, including bunch length, were compared to corresponding measurements using different drive frequencies of the laser, either 249.5 MHz or 499 MHz. Beam transmission was measured by sending the beam up to Faraday Cup 1 and detecting beam interceptions in apertures A1, A2, and MS slits. Longitudinal bunch profile and the corresponding bunch length for various charge per bunch were measured using the chopper phase scanning technique at the chopper's location. The measurement determined the bunch length/pulse length of the laser at very low charge, as well as the bunch length expansion from space-charge due to an increase in charge per bunch. Despite different drive frequencies having different pulse lengths, they approximately had the same laser spot size at the cathode. The results of beam transmission and longitudinal bunch profile measurements from both simulations and experiments are in agreement. Regrettably, at 130 kV, 0.64 pC charge per bunch was not achieved, as there was insufficient drive laser power. One conclusion from the measurements is that at 130 keV beam transmission beam transmission becomes more difficult as the bunch charge approaches 0.64 pC.

When the prebuncher was turned OFF, the measurements showed that the temporal longitudinal bunch profile at the chopper location is Gaussian for low charges. However, the distribution becomes super Gaussian above 60 fC of charge for both drive frequencies of the laser. The order of super Gaussian increases with an increase in charge per bunch (current). On the other hand, with the prebuncher turned on, the distribution becomes Gaussian for both low and high charges.

To validate the measurements obtained from the chopper phase scan technique, we used the GPT modeling program to predict the bunch lengths at the chopper location using two different space charge simulation schemes: *spacecharge3Dmesh* and *spacecharge3D*. When the prebuncher was turned OFF and the charge was low, the simulation results using the *spacecharge3D* scheme showed excellent agreement with the measurements, with a deviation of no more than 15% even at high charges. The simulations using the *spacecharge3Dmesh* scheme also showed good agreement with the measurements at low charges, but the deviation between the simulation results and measurements became more significant at high charges. On the other hand, when the prebuncher was turned ON (the standard CEBAF operating condition), there was excellent agreement between the measurements and the simulation results obtained using both the *spacecharge3D* scheme and the *spacecharge3Dmesh* scheme of the GPT simulation, with deviations of no more than 5%.

For Phase 2 CEBAF injector operations after the SAD in 2023, the initially planned gun voltage of 200 kV was adjusted to 180 kV and later dropped to 140 kV due to technical problems. A laser with lower repetition rates (15.6 MHz), required for the $\mathrm{K_L}$ experiment, was installed and tested during the SAD 2023. Subsequently, we conducted the same types of measurements (beam transmission and bunch length expansion) for the CEBAF Phase

2 injector upgrade as we did for the CEBAF Phase 1 injector upgrade at 130 kV DC gun voltage, and compared results at 130 kV, 140 kV, and 180 kV DC gun voltages. These measurements were performed using the existing laser at 249.5 and 499 MHz drive frequencies, as well as with the newly implemented 15.6 MHz K_L laser. It was observed that the increase in gun voltages led to higher beam energy (and consequently higher relativistic γ and β). This increase in energy resulted in improved beam transmission and reduced bunch length expansion as expected from the reduced space charge present.

Another part of the thesis involves adopting and demonstrating the use of Multi-Objective Genetic Algorithm (MOGA) techniques for optimizing the CEBAF injector. This optimization aims to obtain the optimized settings of magnetic elements and RF systems by employing the GPT particle tracking simulation code. The optimization procedure for GPT implements the "NSGA-II" algorithm and includes 28 variables (magnetic elements and RF settings) and 62 objectives and constraints related to beam transmission, bunch lengths, and normalized transverse emittance at different locations in the beamlines. The optimizations were carried out at 180 kV and 200 kV, followed by beam dynamics simulations. Optimizations were conducted on the JLab ifarm high-performance computing system, while simulations were performed using GPTwin on Microsoft Windows machines CASSTUDENT4 at Jefferson Lab. Simulations were performed for various charge per bunch in the CEBAF injector, assuming simultaneous operation in all four halls. For 180 kV simulations, various charge per bunch scenarios were considered to evaluate beam transmission and characteristics (transverse beam sizes, bunch lengths, energy spread, normalized transverse emittances, etc.) without considering spin manipulations. However, for 200 kV, simulations were conducted to assess beam characteristics with and without spin flipper activation. The results demonstrated excellent transmission, above 90%, with minor differences in transverse and longitudinal beam characteristics between low and high charge simulations at both 180 kV and 200 kV gun voltages. The 180 kV results showed superior beam transmission, incorporating expected solenoid repairs with an inbuilt field map.

Overall, this project sheds light on the insights and challenges associated with transmitting the space-charge dominated high bunch charge beam alongside the low charge beam in the CEBAF injector. From the measurements and simulations at 130 kV gun voltages, for 0.32 pC bunch charge at 64 ns bunch spacing, we can confidently state that the K_L experiment can be performed even at 130 kV gun voltage. The dynamics simulation shows that the beam transmission is above 90%, and bunch length expansion is manageable at the CEBAF injector, facilitating the simultaneous operations of four experimental halls. Simulations explained bunch length expansion and beam transmission at 130 kV gun voltage.

From the optimizations and simulations performed at higher gun voltages of 180 kV and 200 kV, there is an increase in beam transmission greater than 95% for 0.64 pC bunch charge, and bunch length expansion decreases with the increase in gun voltages. This facilitates the operation of the CEBAF injector with high charge per bunch and enables simultaneous operations of four halls. With the Wien filter OFF, the measurements conducted at 140 kV clearly demonstrate that the new Hall D $\mathrm{K_L}$ can provide the necessary amount of bunch charge for the $\mathrm{K_L}$ experiment, with beam transmission exceeding 90% even for a bunch charge of 0.64 pC. For 180 kV measurements with the Wien filter ON, the percentage of beam transmission is low, but it transmits the 0.64 pC charge per bunch for the $\mathrm{K_L}$ experiment. Having the Wien filter ON negatively affected the beam transmission in the 180 kV experiments. If we can tolerate the beam loss, conducting the $\mathrm{K_L}$ experiment with a 0.64 pC bunch charge is feasible even at 140 kV. Additionally, a higher gun voltage is advantageous for beam transmission with a higher bunch charge, due to a decrease in space charge forces. So, keeping in mind the possibility of an increase in gun voltage of the CEBAF injector, $\mathrm{K_L}$ at 0.64 pC can be performed at Jefferson Lab in Hall D along with other experimental Halls. From the simulations and available experimental results, it confirms that the $\mathrm{K_L}$ experiment with 0.32 pC bunch charge can be performed easily, and with 0.64 pC bunch charge, it is doable with some concerns regarding spin manipulations requirements for other CEBAF experimental halls. After optimizations and simulations performed at 180 kV and 200 kV gun voltages, it is indicated that the simultaneous operation of four experimental halls is possible. However, based on the measurements at 180 kV with the Wien filter ON, running the $\mathrm{K_L}$ experiment may be challenging and inconsistent with the conclusions of the simulations.

As a result of finding optimized settings, by varying the laser pulse length and laser spot size around the optima, it is possible to specify the pulse length and spot size of the laser that leads to best transmission. The $\mathrm{K_L}$ laser should be set to have a spot size of 0.55 mm and pulse length of 60 ps for best transmission.

6.2 FUTURE WORKS

The $\mathrm{K_L}$ experiment is scheduled to operate at a 200 kV DC photo-gun. Throughout the course of this thesis, we have delved into the beam studies within the injector and conducted beam dynamics simulations. It is important to note that not all questions regarding the 200 kV injector operations have been addressed in this work. The scope of our simulations covered the front end of the injector up to the first full cryomodules, while the beam studies extended up to Faraday Cup 1 (FCup1) for a single beam, considering different drive frequencies of the laser-either at 249.5 MHz, 499 MHz, or 15.6 MHz. There is potential value in conducting beam studies with multiple beams simultaneously passing through the injector, directed towards the experimental halls. Furthermore, we can explore sending single or interleaved beams specifically to Hall D, tailoring the beam characteristics to meet the requirements of the $\mathrm{K_L}$ experiment. Additionally, we could conduct a series of bunch length measurements at the chopper location for a 200 keV beam, varying the charge per bunch, and subsequently compare the obtained results with those from a 130 keV beam.

In this thesis, the extensive utilization of the General Particle Tracer (GPT) code is evident. GPT performs time-domain tracking in 3D, featuring user-selectable accuracy and incorporating various schemes for space-charge forces, including both Particle-in-Cell (PIC) and point-to-point methods. The code facilitates the definition of arbitrary field maps and custom elements without efficiency loss, covering fields and space charge. It enables the optimization and simulation of numerous variables and constraints, producing more realistic solutions for low-energy and high-charge beams in the injector.

In contemporary physics simulations and optimization, Artificial Intelligence (AI) and Machine Learning (ML) have become increasingly popular. In the context of accelerator physics and particle tracking simulations, AI and ML play pivotal roles in enhancing understanding, optimization, and efficiency. Through simulations like those performed in GPT, substantial data can be generated. AI algorithms optimize beam dynamics parameters, including magnetic elements and RF settings, to achieve goals such as maximizing beam quality or minimizing loss.

Utilizing the GPT model of the virtual compact accelerator, similar to the UITF GPT model employed in our studies, we have commenced collaborative efforts with data scientists at Jefferson Lab to develop a software framework for an accelerator control system. In this framework, ML surrogate models expedite evaluations of specific accelerator configurations, predicting particle beam behavior based on historical simulation data. This approach allows us to anticipate and mitigate issues, as well as optimize experimental setups.

BIBLIOGRAPHY

[1] M. Amaryan *et al.* (KLF collaboration), Strange hadron spectroscopy with secondary KL beam in hall D, arXiv preprint arXiv:2008.08215v3 [nucl-ex] (2021).

[2] S. Dobbs (KLF collaboration), Strange hadron spectroscopy with the KLong facility at Jefferson lab, Rev. Mex. Fis. Suppl. **3**, 0308032 (2022).

[3] R. Kazimi, Simultaneous four-hall operation for 12 GeV CEBAF, in *Proceedings of 4th International Particle Accelerator Conference (IPAC'13), Shanghai, China* (JACoW, CERN, Geneva, Switzerland, 2013), THPFI091.

[4] A. Freyberger *et al.*, Commissioning and operation of 12 GeV CEBAF, in *Proceedings of 6th International Particle Accelerator Conference (IPAC'15), Richmond, VA, USA* (JACoW, CERN, Geneva, Switzerland, 2015), MOXGB2.

[5] M. Spata, 12 GeV CEBAF initial operational experience and challenges, in *Proceedings of 9th International Particle Accelerator Conference (IPAC'18), Vancouver, BC, Canada* (JACoW, CERN, Geneva, Switzerland, 2018), WEYGBD1.

[6] W. Diamond, The injector for the CEBAF CW superconducting linac, Conf. Proc. C **870316**, 1907 (1987).

[7] R. Kazimi, C. K. Sinclair, and G. A. Krafft, Setting and measuring the longitudinal optics in CEBAF injector, eConf **C000821**, MOB14 (2000).

[8] Y. Wang, A. Hofler, and R. Kazimi, Commissioning of the 123 MeV injector for 12 GeV CEBAF, in *Proceedings of 6th International Particle Accelerator Conference (IPAC'15), Richmond,VA, USA* (JACoW, CERN, Geneva, Switzerland, 2015), TUPMA037.

[9] R. Abbott, S. Benson, M. Crofford, D. Douglas, R. Gonzales, R. Kazimi, D. Kehne, G. Krafft, P. Liger, H. Liu, *et al.*, Design, commissioning, and operation of the upgraded CEBAF injector, in *Proceedings of International Linac Conference (1994), Tsukuba, Japan*, Vol. 777 (JACoW, CERN, Geneva, Switzerland, 1994).

[10] R. Kazimi, A. Freyberger, J. Grames, J. Hansknecht, A. Hofler, T. Plawski, M. Poelker, M. Spata, Y. Wang, *et al.*, Operational results of simultaneous four-beam delivery at Jefferson Lab, in *Proceedings of 10th International Particle Accelerator Conference (IPAC'19), Melbourne, Australia* (JACoW, CERN, Geneva, Switzerland, 2019), WEPMP053.

[11] M. Breidenbach, M. Foss, J. Hodgson, A. Kulikov, A. Odian, G. Putallaz, H. Rogers, R. Schindler, K. Skarpaas, and M. Zolotorev, An inverted geometry, high voltage polarized electron gun with UHV load lock, Nucl. Instrum. Meth. A **350**, 1 (1994).

[12] C. K. Sinclair, P. Adderley, B. M. Dunham, J. Hansknecht, P. Hartmann, M. Poelker, J. S. Price, P. M. Rutt, W. J. Schneider, and M. Steigerwald, Development of a high average current polarized electron source with long cathode operational lifetime, Phys. Rev. ST Accel. Beams **10**, 023501 (2007).

[13] P. A. Adderley, J. Clark, J. Grames, J. Hansknecht, K. Surles-Law, D. Machie, M. Poelker, M. L. Stutzman, and R. Suleiman, Load-locked dc high voltage GaAs photogun with an inverted-geometry ceramic insulator, Phys. Rev. ST Accel. Beams **13**, 010101 (2010).

[14] P. A. Adderley *et al.*, Two Wien filter spin flipper, Conf. Proc. C **110328**, 862 (2011).

[15] T. Maruyama, D.-A. Luh, A. Brachmann, J. Clendenin, E. Garwin, S. Harvey, J. Jiang, R. Kirby, C. Prescott, R. Prepost, *et al.*, A systematic study of polarized electron emission from strained GaAs/GaAsP superlattice photocathodes, Appl. Phys. Lett. **85**, 2640 (2004).

[16] J. Hansknecht and M. Poelker, Synchronous photoinjection using a frequency-doubled gain-switched fiber-coupled seed laser and ErYb-doped fiber amplifier, Phys. Rev. ST Accel. Beams **9**, 063501 (2006).

[17] J. T. Yoskowitz, Ion Production and Mitigation in DC High-Voltage Photo-Guns, PhD thesis (Department of Physics, Old Dominion University, Norfolk VA, 2022).

[18] G. Palacious-Serrano, Electrostatic Design and Characterization of a 200 keV Photogun and Wien Spin Rotator, PhD thesis (Department of Electrical and Computer Engineering, Old Dominion University, Norfolk VA, 2021).

[19] Y. Wang, Development of a 300 kV DC High Voltage Photogun and Beam Based Studies of Alkali Antimonide Photocathodes, PhD thesis (Department of Physics, Old Dominion University, Norfolk VA, 2018).

[20] G. Palacios-Serrano, F. Hannon, C. Hernandez-Garcia, M. Poelker, and H. Baumgart, Electrostatic design and conditioning of a triple point junction shield for a 200 kV DC high voltage photogun, Rev. Sci. Instrum. **89**, 104703 (2018).

[21] J. R. Pierce, Rectilinear electron flow in beams, J. Appl. Phys. **11**, 548 (1940).

[22] V. Tioukine and K. Aulenbacher, Operation of the MAMI accelerator with a Wien filter based spin rotation system, Nucl. Instrum. Meth. A **568**, 537 (2006).

[23] P. Adderley, D. Bullard, Y. Chao, C. Garcia, J. Grames, J. Hansknecht, A. Hofler, R. Kazimi, J. Musson, C. Palatchi, *et al.*, An overview of how parity-violating electron scattering experiments are performed at CEBAF, Nucl. Instrum. Meth. A **1046**, 167710 (2023).

[24] Y. Wang, Overview of JLab's Accelerator Program, in *25th Annual Hampton University Graduate Studies (HUGS) Program, Jefferson Lab,VA,USA* (2010).

[25] W. T. Diamond and R. Pico, Status of the CEBAF injector, Thomas Jefferson National Accelerator Facility (TJNAF), Newport News, VA, USA, Technical Report No. CEBAF-PR-89-027, DOE-ER-40150-102, 1989.

[26] M. Ferrario, M. Migliorati, and L. Palumbo, Space Charge Effects, arXiv preprint arXiv:1601.05214, 331 (2014).

[27] M. Crofford, C. Hovater, G. Lahti, C. Piller, and M. Poelker, The RF system for the CEBAF polarized photoinjector, in *Proceedings of 19th International Linear Accelerator Conference (LINAC'1998)* (JACoW, CERN, Geneva, Switzerland, 1998), pp. 552–554.

[28] G. A. Krafft, Correcting M_{56} and T_{566} to obtain very short bunches at CEBAF, AIP Conf. Proc. **367**, 46 (1996).

[29] S. Wang, J. Guo, R. Rimmer, and H. Wang, The new design for capture cavity of CEBAF, in *Proceedings of 5th International Particle Accelerator Conference (IPAC'14), Dresden, Germany* (JACoW, CERN, Geneva, Switzerland, 2014), THPRI080.

[30] C. W. Leemann, The CEBAF superconducting accelerator: An overview, in *Proceedings of 13th International Linac Conference (LINAC1986), Stanford, California, USA* (JACoW, CERN, Geneva, Switzerland, 1986), TU2–3.

[31] C. W. Leemann, D. R. Douglas, and G. A. Krafft, The Continuous Electron Beam Accelerator Facility: CEBAF at the Jefferson Laboratory, Ann. Rev. Nucl. Part. Sci. **51**, 413 (2001).

[32] J. Benesch, A. Bogacz, A. Freyberger, Y. Roblin, T. Satogata, R. Suleiman, and M. Tiefenback, 12 GeV CEBAF beam parameter tables, Jefferson Laboratory, Newport News, VA, USA, Technical Note No. JLAB-TN-08-022, 2018.

[33] C. Yao, Effects of field asymmetry in the coupler, Thomas Jefferson National Accelerator Facility (TJNAF), Newport News, VA, USA, Technical Report No. CEBAF-TN-89-183, 1989.

[34] G. Wu, H. Wang, C. E. Reece, and R. A. Rimmer, Waveguide coupler kick to beam bunch and current dependency on SRF cavities, in *Proceedings of 13th International Workshop on RF Superconductivity (SRF2007), Peking Univ., Beijing, China* (JACoW, CERN, Geneva, Switzerland, 2007), WEP85.

[35] F. E. Hannon, A. S. Hofler, and R. Kazimi, Optimizing the CEBAF injector for beam operation with a higher voltage electron gun, Conf. Proc. C **110328**, 2023 (2011).

[36] A. Freyberger, F. E. Hannon, A. S. Hofler, A. Hutton, and R. Kazimi, Upgrading the CEBAF injector with a new booster, higher voltage gun, and higher final energy, Conf. Proc. C **1205201**, 1945 (2012).

[37] H. Wang, G. Y. Cheng, W. Clemens, G. L. Davis, K. Macha, R. B. Overton, and D. Spell, Injector cavities fabrication, vertical test performance and primary cryomodule design, in *Proceedings of 6th International Particle Accelerator Conference (IPAC'15), Richmond, VA, USA* (JACoW, CERN, Geneva, Switzerland, 2015), WEPWI030.

[38] H. Wang, G. Cheng, F. Hannon, A. Hofler, R. Kazimi, J. Preble, and R. Rimmer, RF design optimization for new injector cryounit at CEBAF, in *Proceedings of 4th International Particle Accelerator Conference (IPAC'13), Shanghai, China* (JACoW, CERN, Geneva, Switzerland, 2013), WEPWO073.

[39] G. Cheng, J. Henry, J. D. Mammosser, R. A. Rimmer, H. Wang, M. Wiseman, and S. Yang, Mechanical design of a new injector cryomodule 2-cell cavity at CEBAF, in *Proceedings of 2013 North American Particle Accelerator Conferenceof (PAC2013), Pasadena, CA, USA* (JACoW, CERN, Geneva, Switzerland, 2013), WEPAC47.

[40] G. Cheng, M. Drury, J. Fischer, R. Kazimi, K. Macha, and H. Wang, JLab new Injector cryomodule design, fabrication and testing, in *Proceedings of 18th International Conference on RF Superconductivity (SRF2017), Lanzhou, China* (JACoW, CERN, Geneva, Switzerland, 2018), MOPB045.

[41] F. Marhauser and H. Wang, Quadrupole decomposition of the C100 cavity accelerating field, Jefferson Laboratory, Newport News, VA, USA, Technical Note No. JLAB-TN-09-016, 2016.

[42] A. Hofler, R. Kazimi, K. Surles-Law, and Y. Wang, Modeling for the phased injector upgrade for 12 GeV CEBAF, in *Proceedings of 14th International Particle Accelerator Conference (IPAC'23), Venice, Italy* (JACoW, CERN, Geneva, Switzerland, 2023), WEPL075.

[43] J. D. Jackson, *Classical Electrodynamics* (John Wiley & Sons, 1999).

[44] H. Goldstein, C. P. Poole, and J. L. Safko, *Classical Mechanics* (Addison-Wesley, 2002).

[45] M. Reiser, *Theory and Design of Charged Particle Beams* (John Wiley & Sons, 2008).

[46] K. Floettmann, Some basic features of the beam emittance, Phys. Rev. ST Accel. Beams **6**, 034202 (2003).

[47] J. D. Walecka, *Fundamentals of Statistical Mechanics: Manuscript and Notes of Felix Bloch* (World Scientific, 2000).

[48] M. Conte and W. W. MacKay, *An Introduction to the Physics of Particle Accelerators* (World Scientific, 2008).

[49] S.-Y. Lee, *Accelerator Physics* (World Scientific, 2018).

[50] S. Peggs and T. Satogata, *Introduction to Accelerator Dynamics* (Cambridge University Press, 2017).

[51] I. V. Bazarov, B. M. Dunham, Y. Li, X. Liu, D. G. Ouzounov, C. K. Sinclair, F. Hannon, and T. Miyajima, Thermal emittance and response time measurements of negative electron affinity photocathodes, J. Appl. Phys. **103**, 054901 (2008).

[52] H. Wiedemann, *Particle Accelerator Physics* (Springer Nature, 2015).

[53] K. Wille, *The Physics of Particle Accelerators: An Introduction* (Clarendon Press, 2000).

[54] K. L. Brown and R. V. Servranckx, First- and second-order charged particle optics, AIP Conf. Proc. **127**, 62 (1985).

[55] T. P. Wangler, *RF Linear Accelerators* (John Wiley & Sons, 2008).

[56] R. Wideröe, Über ein neues prinzip zur herstellung hoher spannungen, Archiv für Elektrotechnik **21**, 387 (1928).

[57] V. Veshcherevich and S. Belomestnykh, Buncher cavity for ERL, Conf. Proc. C **030512**, 1198 (2003).

[58] M. G. Minty and F. Zimmermann, *Measurement and Control of Charged Particle Beams* (Springer Nature, 2003).

[59] K. Schindl, Space charge, CERN Accelerator School Intermediate accelerator physics, 305 (2006).

[60] L. Palumbo, V. Vaccaro, and M. Zobov, Wake fields and impedance, CERN Report No. physics/0309023 ; LNF-94-041-P ; LNF-94-041-P, 331 (1995).

[61] E. Metral, G. Rumolo, W. Herr, E. Metral, E. Metral, E. Metral, E. Metral, G. Rumolo, W. Herr, and G. Rumolo, Impedance and collective effects, in *Particle Physics Reference Library: Volume 3: Accelerators and Colliders* (2020), pp. 105–181.

[62] A. W. Chao, *Physics of Collective Beam Instabilities in High Energy Accelerators (Wiley Series in Beam Physics and Accelerator Technology)* (John Wiley & Sons, 1993).

[63] M. Ferrario, V. Fusco, M. Migliorati, and L. Palumbo, Emittance degradation due to wake fields in a high brightness photoinjector, Int. J. Mod. Phys. A **22**, 4214 (2007).

[64] Pulasr Physics, General Particle Tracer Version 3.39, `http://www.pulsar.nl/gpt`.

[65] G. Poplau, U. Van Rienen, B. Van der Geer, and M. De Loos, Multigrid algorithms for the fast calculation of space-charge effects in accelerator design, IEEE Trans. Magn. **40**, 714 (2004).

[66] S. B. van der Geer, O. J. Luiten, M. J. de Loos, G. Poplau, and U. van Rienen, 3D space-charge model for GPT simulations of high-brightness electron bunches, Inst. Phys. Conf. Ser. **175**, 101 (2005).

[67] S. B. van der Geer and M. de Loos, General Particle Tracer User Manual Version 3.39, Pulsar Physics (2020).

[68] S. Pokharel, M. Bruker, J. Grames, A. Hofler, R. Kazimi, G. Krafft, and S. Zhang, CEBAF injector model for K_L beam conditions, in *Proceedings of 13th International Particle Accelerator Conference (IPAC'22), Thailand, Bangkok* (JACoW, CERN, Geneva, Switzerland, 2022), MOPOTK052.

[69] S. Pokharel, M. Bruker, J. Grames, A. Hofler, R. Kazimi, G. Krafft, and S. Zhang, CEBAF injector model for K-Long bunch charge at 200 kV, in *Proceedings of 14th International Particle Accelerator Conference (IPAC'23), Venice, Italy* (JACoW, CERN, Geneva, Switzerland, 2023), WEPL054.

[70] A.S.Hofler and R.Kazimi, *Injector Upgrade Phase1 Settings for 130 kV Gun HV*, (2021) `https://wiki.jlab.org/ciswiki/images/a/a7/UIPhase1Settings130kV_2021.pdf`.

[71] F.-J. Decker, Beam distributions beyond RMS, AIP Conf. Proc. **333**, 550 (1995).

[72] B. Roberts, F. Hannon, M. Ali, E. Forman, J. Grames, R. Kazimi, W. Moore, M. Pablo, M. Poelker, A. Sanchez, *et al.*, Harmonically resonant cavity as a bunch-length monitor, Phys. Rev. Accel. Beams **19**, 052801 (2016).

[73] S. Zhang, *Status of the CEBAF Photo-Injector Drive Laser System for KLong Beam*, PDF document, (Sept. 2023) `https://wiki.jlab.org/klproject/images/8/8b/KLong_meeting_talk_Zhang.pdf`.

[74] S. B. van der Geer and M. de Loos, Multi-objective Genetic Optimization with the General Particle Tracer (GPT) Code, in *Proceedings of 6th International Particle Accelerator Conference (IPAC'15), Richmond, VA, USA* (JACoW, CERN, Geneva, Switzerland, 2015), MOPJE076.

[75] K. Deb, A. Pratap, S. Agarwal, and T. Meyarivan, A fast and elitist multiobjective genetic algorithm: NSGA-II, IEEE Trans. Evol. Comput. **6**, 182 (2002).

[76] G. Palacios-Serrano *et al.*, High voltage design and evaluation of Wien filters for the CEBAF 200 keV injector upgrade, in *Proceedings of 12th International Particle Accelerator Conference (IPAC'21), Campinas, SP, Brazil* (JACoW, CERN, Geneva, Switzerland, 2021), MOPAB324.

[77] J. D. Jackson, *Classical Electrodynamics* (John Wiley & Sons, 1998).

[78] S.-Y. Lee, *Spin Dynamics and Snakes in Synchrotrons* (World Scientific, 1997).

[79] A. Hofler, *UITF Gun through 2-7 Quarter Optimization, UITF Ops Review (2016)*, `https://wiki.jlab.org/ciswiki/images/1/1aUITF_OpsReview_Hofler3.pptx`.

[80] A. Hofler, Relative Phases UITF 1nA Optimization (private communiction),

[81] A. Edelen, N. Neveu, Y. Huber, M. Frey, C. Mayes, and A. Adelmann, Machine learning for orders of magnitude speedup in multiobjective optimization of particle accelerator systems, Phys. Rev. Accel. Beams **23**, 044601 (2020).

[82] F. Chollet *et al.*, Keras: The Python Deep Learning library (2018), https://keras.io.

[83] Martín Abadi *et al.*, TensorFlow: Large-Scale Machine Learning on Heterogeneous Systems, https://www.tensorflow.org.

[84] D. P. Kingma and J. Ba, Adam: A method for stochastic optimization, arXiv preprint arXiv:1412.6980v9 [cs.LG] (2017).

[85] F. Pedregosa *et al.*, Scikit-learn: Machine Learning in Python, J. Mach. Learn. Res. **12**, 2825 (2011).

APPENDIX A

GPT SPACE CHARGE ALGORITHM VALIDATION

Considering a $\mathrm{K_L}$ bunch charge of $Q = 0.64$ pC and an *rms* bunch length of $\sigma_z = 19.10$ ps, the peak current for Gaussian distributions is given by $I_{\mathrm{peak}} = Q/(\sqrt{2\pi} \times \sigma_z) = 0.64/(\sqrt{2\pi} \times 19.10) = 13.37\,\mathrm{mA}$. Additionally, for an *rms* transverse beam size of $\sigma_{x,y} = 0.55$ mm and normalized thermal emittances of $\epsilon_{n,th} = 0.1348\pi$ mm mrad, Eq. (113) yields the transverse *rms* envelope equation in a drift for Gaussian distributions of the electron beam:

$$\sigma''_{x,y} = \frac{2.9191 \times 10^{-7}}{\sigma_{x,y}} + \frac{9.2636 \times 10^{-14}}{\sigma^3_{x,y}}. \tag{125}$$

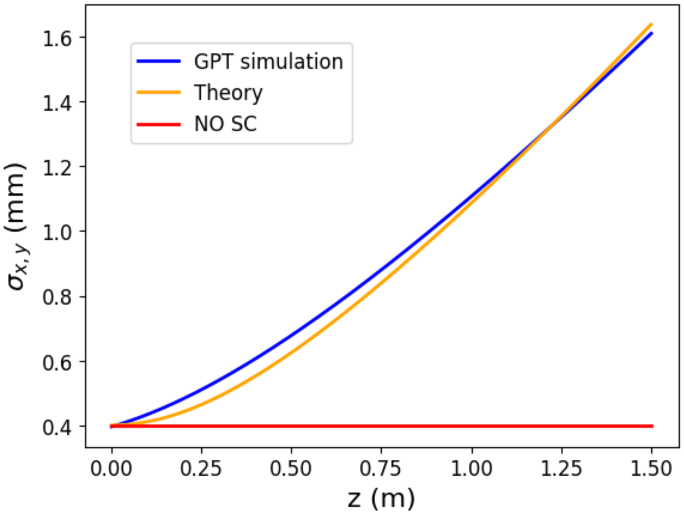

FIG. 76. Comparison of transverse beam size evolution between simulations and theory along a 1.5 m drift. The solution of Eq. (125) (orange) is compared against GPT results (blue). The red line corresponds to the case with no space charge.

Figure 76 compares the solution of Eq. (125) with the beam envelope simulated using GPT. There is a very close agreement between the space charge algorithm employed in GPT and the theoretical calculations for the Gaussian beam with a 0.64 pC bunch charge at a beam energy of 200 keV.

APPENDIX B

BUNCH LENGTH AND BUNCHER VOLTAGE CALCULATION AT UITF

ABSTRACT

In this note, we examine the evolution of the longitudinal phase space and bunch length compression in a non-relativistic electron beam, utilizing the beamline layout of the Upgraded Injector Test Facility (UITF) at Jefferson Lab. Additionally, we calculate the required buncher voltage for a 200 keV electron beam.

I. GENERAL PARTICLE TRACER (GPT) SIMULATION

The particle distribution at the cathode in the simulation is generated by GPT using the UITF GPT model and corresponding settings [79, 80]. The beam is assumed to follow a Gaussian distribution in t, x, y, p_x, and p_y based on the laser profile. The transverse beam size is 213 μm, the laser pulse length is 21.3 ps, and the transverse emittance is 0.061 mm mrad. A beam current of 1 nA is used, resulting in a bunch charge of 1.333×10^{-18} C for a 750 MHz CW (continuous wave) mode frequency. The simulation utilizes 5000 macro particles.

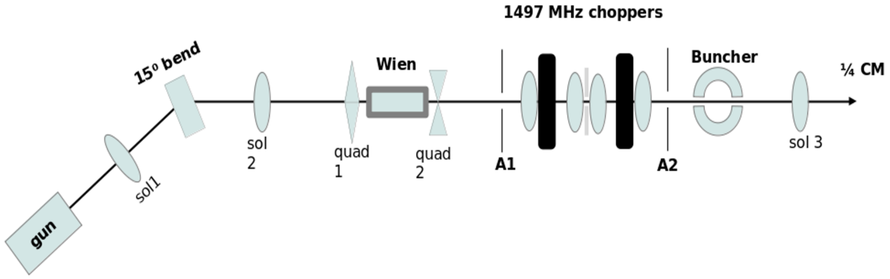

FIG. 77. Layout of the UITF up to quarter cryomodule at JLab.

TABLE 11. Locations of the beamline elements for UITF injector at 200 kV gun voltage. Here, MDS is the dipole magnet, MFs are the solenoids, MQs are the quadrupole magnets.

Location of Beam Line Elements			
Elements	Positions (m)	Elements	Positions (m)
DC Gun	0.0	MFH1K01	0.5951
MDS2K01	1.3401	MFB2K02	1.9695
MQU2K02	2.1138	MQU2K03	3.4108
MFA3K01	3.9571	Chopper 1	4.0306
MFD3K02A	4.5969	MFD3K02B	4.6866
Chopper 2	5.2529	MFA3K03	5.322595
Buncher	6.1554	MFA4K03	7.3654
2-cell	9.2989235	7-cell	9.461988

In the simulation, a straight beamline is employed, omitting components such as a 15° dipole, RF choppers, beam diagnostics, Wien apertures, etc. During GPT simulations, an electron bunch is chirped by the buncher cavity (RF cavity) at zero crossing, followed by a drift where slow electrons at the head move back with respect to the centroid, and fast electrons at the tail catch up with the centroid as shown in Fig. 78.

II. CALCULATIONS

For the electron beam, the rest mass energy is $\mathcal{E}_0 = mc^2 = 0.511$ MeV $= 511\,\text{keV}$, and for the 750 MHz UITF buncher with $f_{RF} = 750$ MHz, $\lambda_{RF} = c/f_{RF} = 3 \times 10^8/(750 \times 10^6) = 0.4$ m.

For a non-relativistic beam of 200 keV, the relativistic parameters are $\gamma = 1.391388$ and $\beta = 0.6953$. For the drift length of $L = 2.612456650$ m, using Eq. (99), the bunching voltage is

$$V_{bun} = \frac{\lambda_{RF} mc^2 \gamma^3 \beta^3}{2\pi e L} = \frac{0.4 \times 511 \times 1.391388^3 \times 0.6953^3}{2\pi \times 2.612456650} = 11.2750\,\text{kV}. \quad (126)$$

and using Eq. (101), the minimum bunch length is:

$$\sigma_{z_3} = \sqrt{\langle z_3^2 \rangle} = \frac{L}{\gamma^2 \beta^2} \sigma_{\delta \mathcal{E}_1} = \frac{2.612456650}{1.391388^2 \times 0.6953^2} 0.76278932 \times 10^{-4} = 0.212\,920\,\text{mm}, \quad (127)$$

which is very close to the GPT simulation value of 0.226148 mm. Also,

$$\mathrm{M}_{56} = \frac{L}{\gamma^2} = 1.349436\mathrm{m}. \tag{128}$$

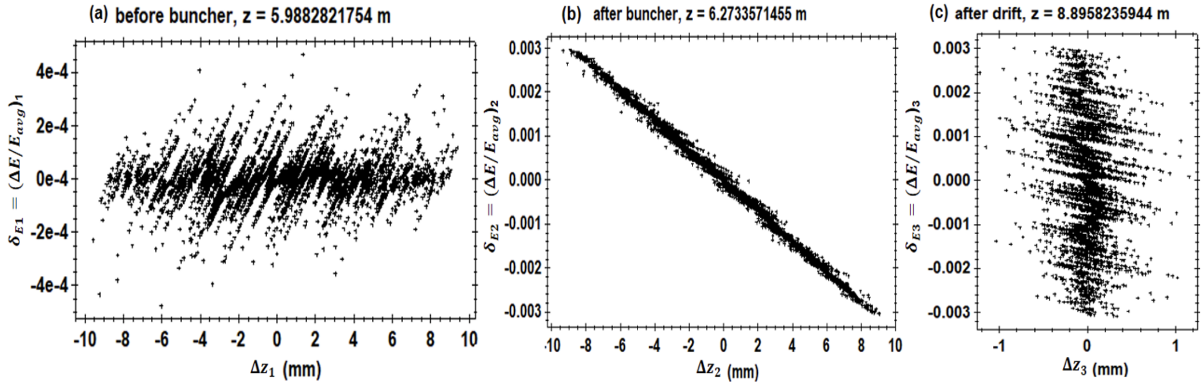

FIG. 78. Evolution of particle distribution in the longitudinal phase space (Δz, δE) along the UITF beamline. The positions (a), (b), and (c) correspond to the different locations from the buncher. (a) Before the buncher (chirper), $z_1 = 5.98828218$ m, $\sigma_{z_1} = 3.9362$ mm=18.8832 ps, $\sigma_{\delta\mathcal{E}_1} = \left(\frac{\sigma_\gamma}{\gamma}\right)_1 = 0.76278932 \times 10^{-4}$, (b) After the buncher, $z_2 = 6.27335714$ m, $\sigma_{z_2} = 3.8958$ mm $= 18.8078$ ps, $\sigma_{\delta\mathcal{E}_2} = \left(\frac{\sigma_\gamma}{\gamma}\right)_2 = 1.33196145 \times 10^{-3}$ (c) After the drift of length $L = 2.612456650$ m, $z_3 = 8.89582360$ m, $\sigma_{z_3} = 0.226148$ mm $= 1.084830$ ps, $\sigma_{\delta\mathcal{E}_3} = \left(\frac{\sigma_\gamma}{\gamma}\right)_3 = 1.33236124 \times 10^{-3}$.

The buncher voltage may be determined via the slope of the energy-time plot in Fig. 79 as:

$$V_{bun} = \frac{\Delta E}{\omega e \Delta t} = \frac{(2\mathrm{keV} \times 10^{12})\mathrm{ps}}{2\pi e \times 0.750 \times 10^{9} \times 38\mathrm{ps}} = 11.1688\,\mathrm{kV}, \tag{129}$$

which is close to the value given by Eq. (126).

Using GPT, we investigated the impact of the buncher cavity on the longitudinal phase space at UITF at Jefferson Lab. Additionally, we calculated the buncher voltage required for

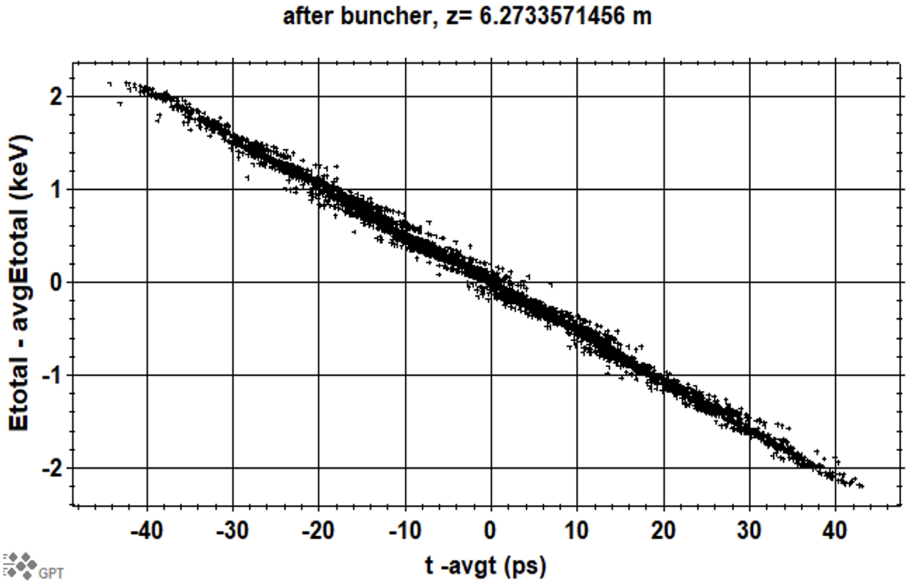

FIG. 79. Longitudinal phase space (Δt, ΔE) just after the 750 MHz buncher at UITF. The location is at $z = 6.2733571456$ m downstream from the gun.

full compression of the bunch and determined the minimum bunch length achievable under full compression.

APPENDIX C

MACHINE LEARNING SURROGATE MODEL FOR CEBAF INJECTOR

A machine learning (ML) surrogate model, often simply referred to as a ‘surrogate’, is created using machine learning techniques to approximate the behavior of a more complex, computationally expensive, or time-consuming physical or computational model. The primary purpose of a surrogate model is to act as a proxy for the original model, providing a computationally efficient means to make predictions or perform optimizations. Utilizing the machine learning surrogate model simplifies the computational process.

We utilized GDFMGO (Non-dominated Sorting Genetic Algorithm (NSGA-II)), a multi-objective global optimizer implemented in GPT, to obtain optimized injector settings (magnetic elements and RF). However, the optimization process for injectors required significant computational resources, resulting in time-consuming procedures. Furthermore, when different injector configurations were necessary, despite maintaining consistent variables, we developed a ML surrogate model customized to the specific configurations of the CEBAF injector.

Data were generated through GPT simulations, encompassing diverse accelerator settings, including magnetic and RF elements, within the operational limits of the CEBAF injector. The general procedure for constructing the machine learning (ML) surrogate models is illustrated in Fig. 80. An ML model was trained using a sparse, random sample of accelerator input variables and the resulting beam parameters. This ML model serves as a rapid and efficient representation of the physics simulation.

Based on the data acquired from GPT simulations, we employed artificial neural networks (NNs) to construct the ML surrogate model. The NNs were implemented using KERAS [82]] and TensorFlow [83]. The architecture featured a fully connected, feed-forward NN with four hidden layers, each consisting of 40 nodes and hyperbolic tangent activation functions. No regularization penalties, such as L1 or L2 norm, were applied to the weights. The NNs underwent training for 2000 epochs with a batch size of 500 points. The Adam optimization algorithm [84] was employed for training, initialized with a learning rate of $\alpha = 0.001$, and hyper parameters $\beta_1 = 0.9$ and $\beta_2 = 0.999$. In this context, the loss function or error metric

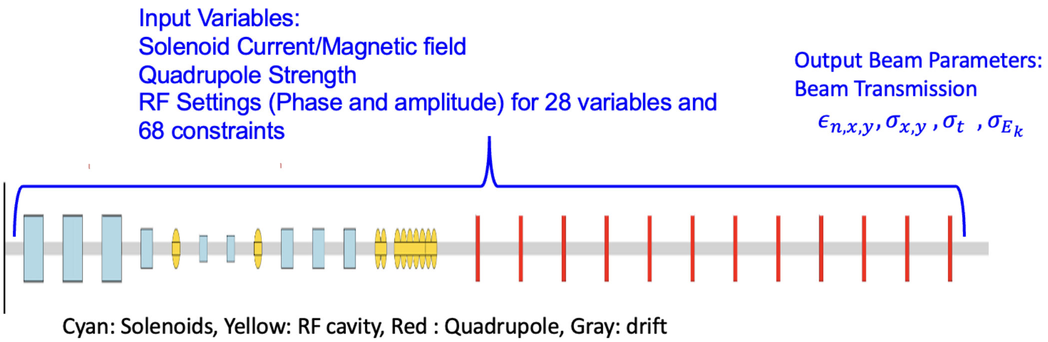

FIG. 80. Schematic of input variables and output beam parameters for the ML surrogate model of the CEBAF injector. The input variables include magnetic and RF element settings, while the output beam parameters consist of transverse beam sizes, normalized transverse emittances, bunch length, energy spread, and beam transmission.

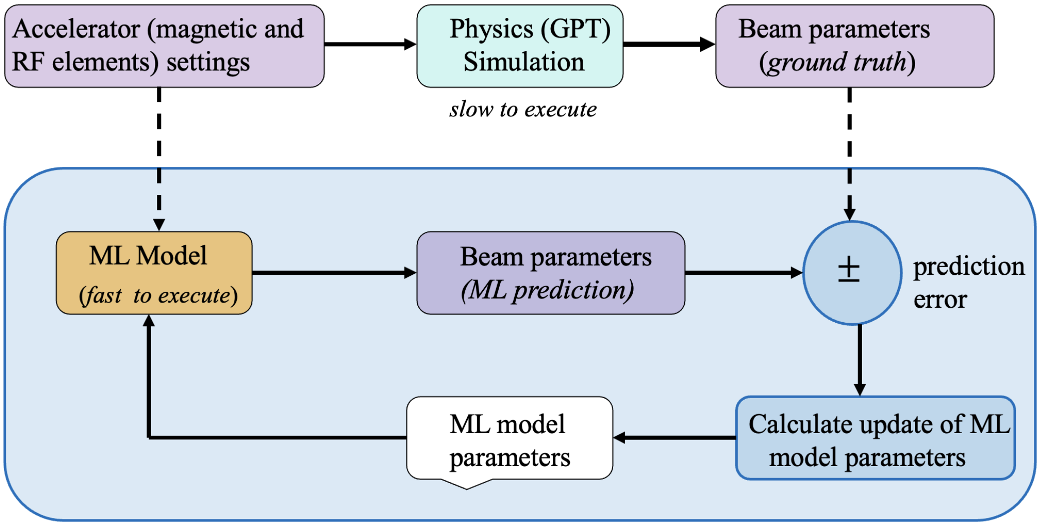

FIG. 81. The flow chart of the ML surrogate models. The figure is derived from [81].

is the Mean Squared Error (MSE), defined as:

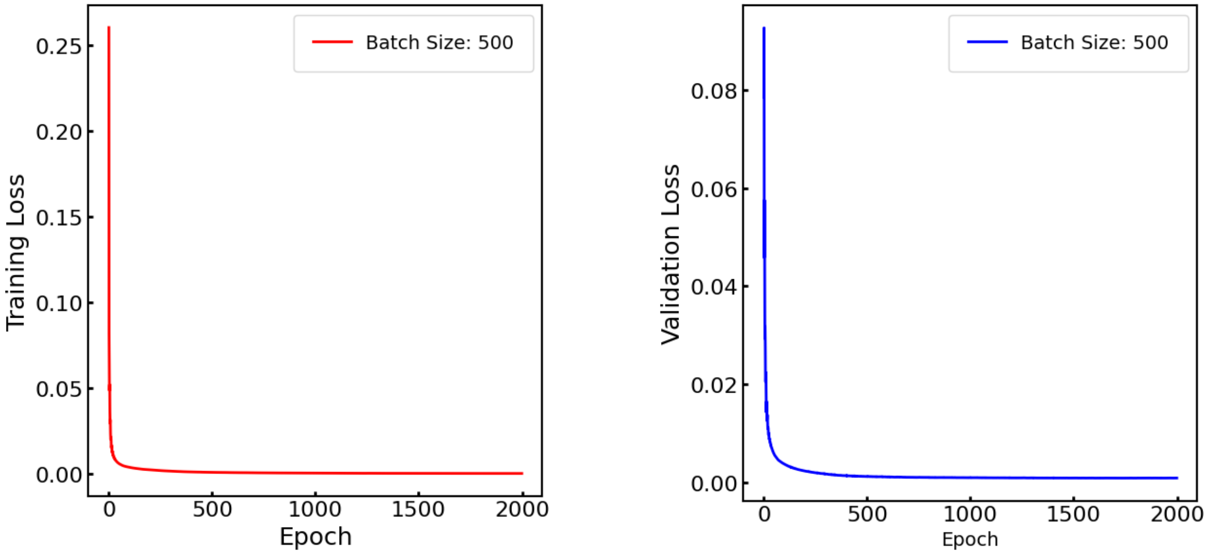

(a) The training loss vs. epoch.

(b) The validation loss vs. epoch.

FIG. 82. The training loss and validation loss vs. epoch for NN surrogate model for CEBAF injector.

$$\mathrm{MSE} = \frac{1}{N}\sum_{i=1}^{N}(y_i - \hat{y}_i)^2. \tag{130}$$

Here, N represents the number of samples, where y_i denotes the actual value (GPT simulations) of the sample data point i, also known as the true value, and $\hat{y}_i$ signifies the predicted value of the sample data point i.

For training and testing, the random sample data was randomly split into training (75%), validation (25%). The data was divided into training and testing sets using SCIKIT-LEARN [85]. The data, obtained from GPT simulations, underwent scaling to fit within an appropriate range. In our case, the data was scaled to fall within the range of [-1, 1].

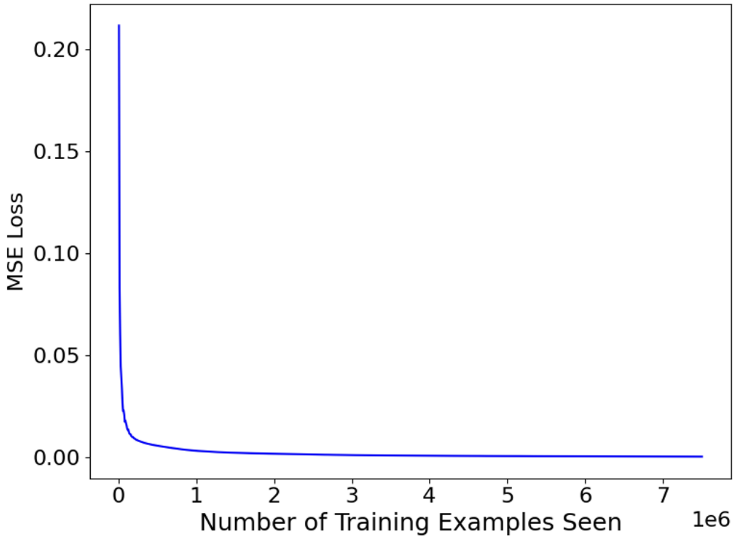

FIG. 83. MSE for the CEBAF injector surrogate model across different training set sizes. Beyond a few thousand points, we observe a decrease in error.

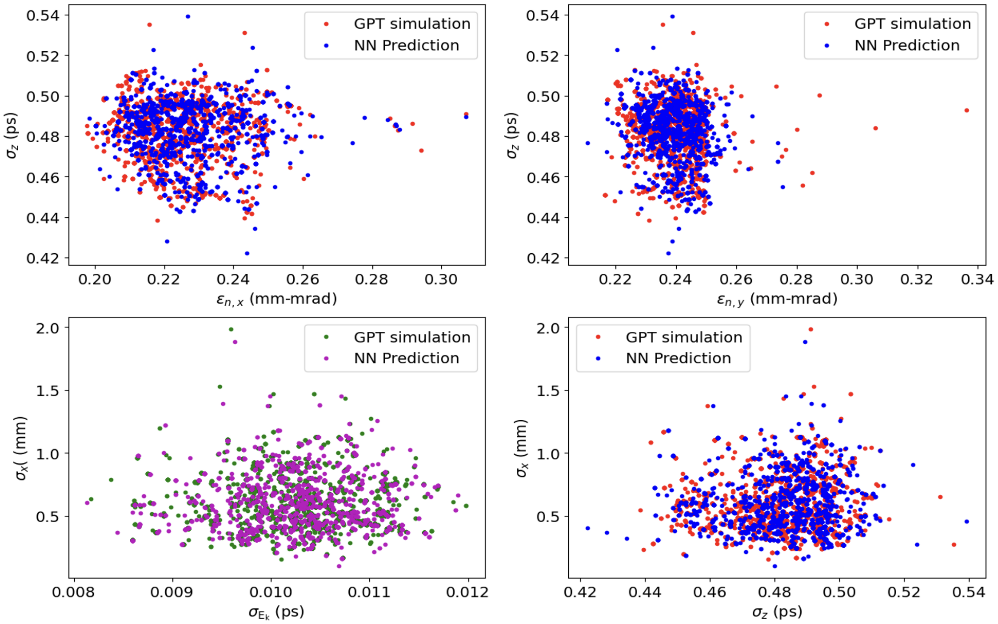

FIG. 84. GPT simulation results and corresponding predictions from the NN surrogate model for the output beam parameters of the CEBAF injector. It demonstrates the excellent agreement between the GPT simulation results and the NN surrogate model.

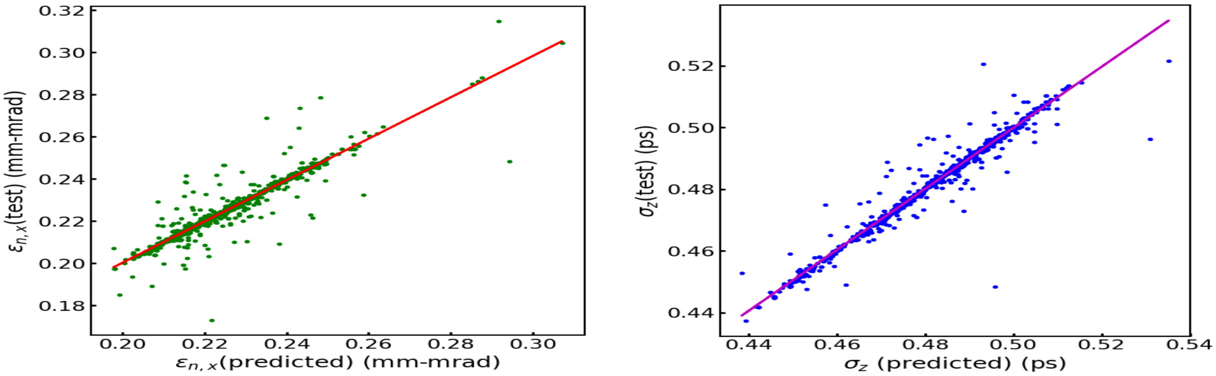

(a) Normalized horizontal emittance.

(b) Bunch length.

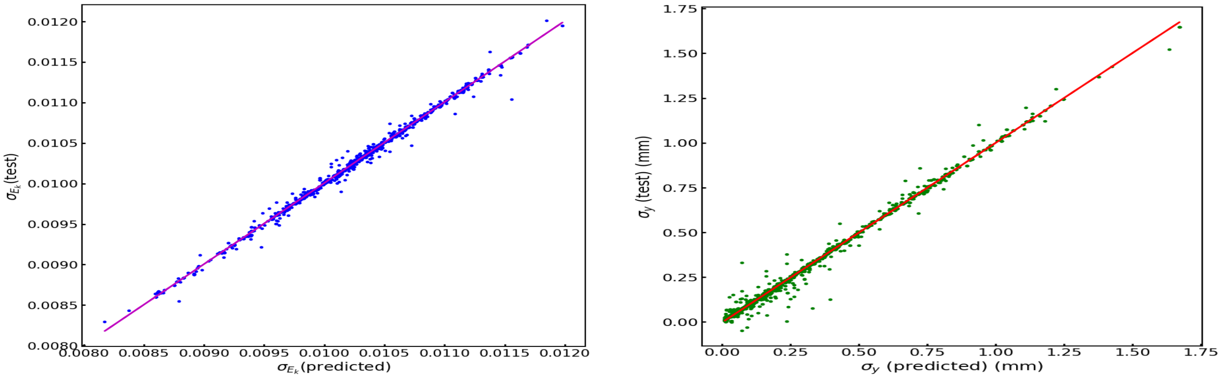

(c) Energy spread.

(d) Vertical beam size.

FIG. 85. GPT simulations vs. NN surrogate model prediction for the output beam parameters of the CEBAF injector (a) Normalized horizontal emittance, (b) Bunch length, (c) Energy spread, and (d) Vertical beam size. Perfect prediction aligns with a straight diagonal line.

APPENDIX D

TRANSFER MATRIX FOR SUPERCONDUCTING LINAC (SCL) ELEMENTS

I. DRIFT

For a drift of length L, the transfer matrix is

$$\mathbf{M}_{\text{drift}} = \begin{pmatrix} 1 & L & 0 & 0 & 0 & 0 \\ 0 & 1 & 0 & 0 & 0 & 0 \\ 0 & 0 & 1 & L & 0 & 0 \\ 0 & 0 & 0 & 1 & 0 & 0 \\ 0 & 0 & 0 & 0 & 1 & \frac{L}{\gamma^2} \\ 0 & 0 & 0 & 0 & 0 & 1 \end{pmatrix}. \tag{131}$$

II. QUADRUPOLE

For a quadrupole of length L, the transfer matrix is

$$\mathbf{M}_{\text{Quad}} = \begin{pmatrix} \cos kl & \frac{1}{k}\sin kl & 0 & 0 & 0 & 0 \\ -k\sin kl & \cos kl & 0 & 0 & 0 & 0 \\ 0 & 0 & \cosh kl & \frac{1}{k}\sinh kl & 0 & 0 \\ 0 & 0 & k\sinh kl & \cosh kl & 0 & 0 \\ 0 & 0 & 0 & 0 & 1 & \frac{L}{\gamma^2} \\ 0 & 0 & 0 & 0 & 0 & 1 \end{pmatrix}. \tag{132}$$

III. SOLENOID

For a solenoid of length L, the transfer matrix is

$$\mathbf{M}_{\text{Solenoid}} = \begin{pmatrix} c^2 & \frac{1}{k}sc & sc & \frac{1}{k}s^2 & 0 & 0 \\ -ksc & c^2 & -ks^2 & sc & 0 & 0 \\ -sc & -\frac{1}{k}s^2 & c^2 & \frac{1}{k}sc & 0 & 0 \\ ks^2 & -sc & -ksc & c^2 & 0 & 0 \\ 0 & 0 & k\sinh kl & \cosh kl & 0 & 0 \\ 0 & 0 & 0 & 0 & 1 & \frac{L}{\gamma^2} \\ 0 & 0 & 0 & 0 & 0 & 1 \end{pmatrix}. \tag{133}$$

IV. RF CAVITY

For a RF cavity of length L, the transfer matrix is

$$\mathbf{M}_{\text{cavity}} = \begin{pmatrix} 1 & 0 & 0 & 0 & 0 & 0 \\ k/(\beta\gamma)_f & (\beta\gamma)_i/(\beta\gamma)_f & 0 & 0 & 0 & 0 \\ 0 & 0 & 1 & 0 & 0 & 0 \\ 0 & 0 & k/(\beta\gamma)_f & (\beta\gamma)_i/(\beta\gamma)_f & 0 & 0 \\ 0 & 0 & 0 & 0 & 1 & 0 \\ 0 & 0 & 0 & 0 & -2\gamma^2 k/(\beta\gamma)_f & (\beta\gamma)_i/(\beta\gamma)_f \end{pmatrix}. \tag{134}$$

APPENDIX E

INJECTOR QUICK REFERENCE DRAWING
Rev 17 BETA

Spring/Summer 2021
AIPINJ Phase I
Gun -> Chopper

DRAFT 6 (6/7):	MBH0L02H/V -> MHB0L02H/V after walkthru with DC Power and Mag Meas. Added VCG0L02A. Updated Laser Box outline. Updated Rapid Access CARM positions. Left to do -- add DecaRads. Other suggestions?... moser @ jlab
DRAFT 5 (4/19):	IYG0I01 -> ITV0I01, ITV0I02 -> IYG0I02 (had YAG screened viewer position wrong). Updated A2 aperture to hole-size to 6mm.
DRAFT 4 (3/29):	Changed ITV0I01->IYG0I01, ISL0I04->ISL0I04D to match CED. Updated 5D spur. Added Songsheet and AIPINJ Phase II clickable hyperlinks.
DRAFT 3 (3/5):	Re-arranged VIP2I00,A,B,C to infer that only VIP2I00 is on the main beamline. Added E-field PVs for Wien filters. Added VIP4D00E marker.
DRAFT 2 (2/19):	Removed VRVs -- not in the beam path. Corrected names for second Wien cross, prebuncher, and A3/A4 apertures.
DRAFT 1 (2/12):	Updated Gun -> Choppers, AIPINJ Phase I, from 1/28 preliminary songsheet ACC0002845-0001. Added EPICS PVs and Songsheet names for RF elements Added chopper slit and central plug PVs

D. Moser
Revision 17 BETA: DRAFT-6
File: 12GeV_injector_quick_reference_Dwg_rev17_6.ai

PAGE 1

INJECTOR QUICK REFERENCE DRAWING

Bldg 53, Injector Service Building, Above-Ground Phones:
x6165 -- (3x+base) Cordless Phones
x5167 -- Outside PSS D1, in between D1
and D2, outside D2 (3 phones)

x6207 -- by tunnel entrance/
1st R/S Box

Gun HV (kV)	***Electron*** Momentum (MeV/c)	Relativistic Factor (γ)	Fraction of Speed of Light
100	0.335	1.196	0.548
130	0.387	1.254	0.604
200	0.494	1.391	0.695
300	0.630	1.587	0.777

* 2021 Physics Setting *

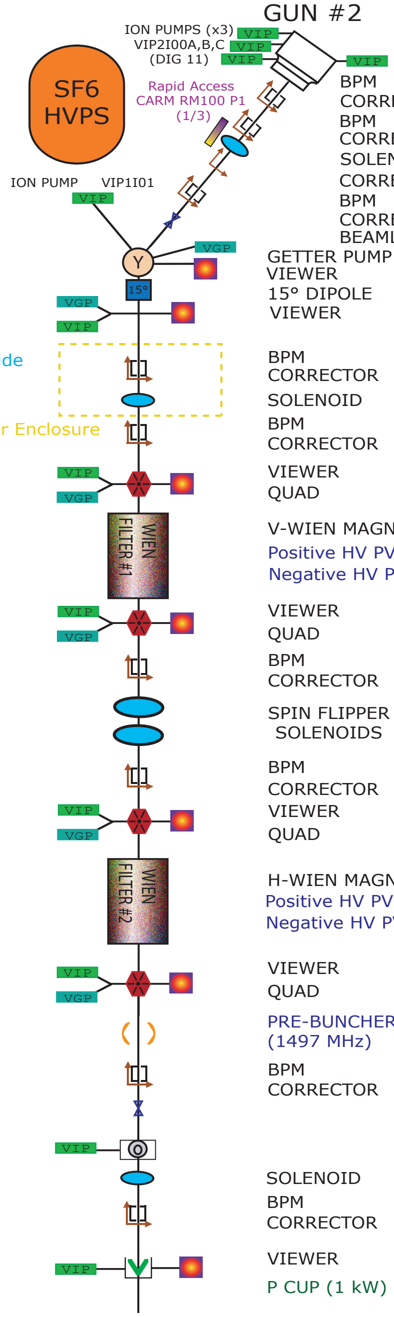

GETTER PUMP	VGP1I02
ION PUMP	VIP1I02

x6208 -- both outside by camera and inside
laser room (and by R/S box 2)

ION PUMP	VIP1I03
GETTER PUMP	VGP1I03
VERTICAL WIEN FILTER	MWF1I04
ION PUMP	VIP1I04
GETTER PUMP	VGP1I04
ION PUMP	VIP1I05
GETTER PUMP	VGP1I05
HORIZONTAL WIEN FILTER	MWF1I06
ION PUMP	VIP1I06
GETTER PUMP	VGP1I06
BEAMLINE VALVE	VBV1I07
DP CAN	VDP0I00
ION PUMP	VIP0I00
ION PUMP	VIP0I01

ION PUMP	VIP2I00
BPM	IPM2I00
CORRECTOR	MBH2I00H&V
BPM	IPM2I00A
CORRECTOR	MBH2I00AH&V
SOLENOID	MFX2I01
CORRECTOR	MBH2I01H&V
BPM	IPM2I01A
CORRECTOR	MBH2I01AH&V
BEAMLINE VALVE	VBV2I01A
GETTER PUMP	VGP1I01
VIEWER	ITV2I01
15° DIPOLE	MDR1I02
VIEWER	ITV1I02
BPM	IPM1I02
CORRECTOR	MBH1I02H&V
SOLENOID	MFX1I03
BPM	IPM1I03
CORRECTOR	MBH1I03H&V
VIEWER	ITV1I03
QUAD	MQW1I03
V-WIEN MAGNET	MWF1I04
Positive HV PVs	PWF1I04P
Negative HV PVs	PWF1I04N
VIEWER	ITV1I04
QUAD	MQW1I04
BPM	IPM1I04
CORRECTOR	MBH1I04H&V
SPIN FLIPPER SOLENOIDS	MFG1I04A MFG1I04B
BPM	IPM1I05
CORRECTOR	MBH1I05H&V
VIEWER	ITV1I05
QUAD	MQW1I05
H-WIEN MAGNET	MWF1I06
Positive HV PVs	PWF1I06P
Negative HV PVs	PWF1I06N
VIEWER	ITV1I06
QUAD	MQW1I06
PRE-BUNCHER (1497 MHz)	RIN1I06 PVs R0OP
BPM	IPM1I07
CORRECTOR	MBH1I07H&V
SOLENOID	MFX0I01
BPM	IPM0I01
CORRECTOR	MBH0I01H&V
VIEWER	ITV0I01
P CUP (1 kW)	IFY0I01

D. Moser
Revision 17 BETA: DRAFT-6
File: 12GeV_injector_quick_reference_Dwg_rev17_6.ai

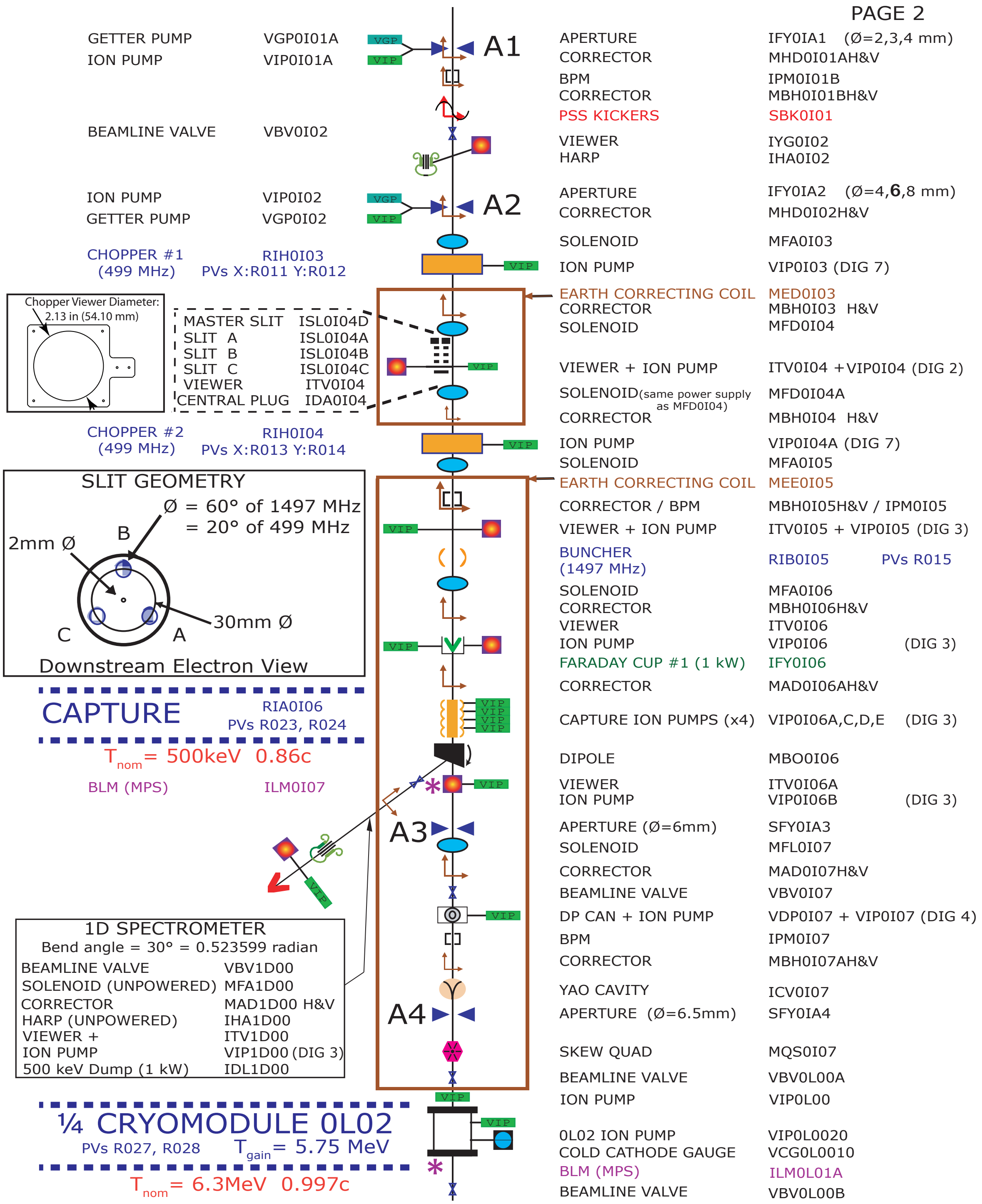

D. Moser
Revision 17 BETA: DRAFT-6
File: 12GeV_injector_quick_reference_Dwg_rev17_6.ai

PAGE 3

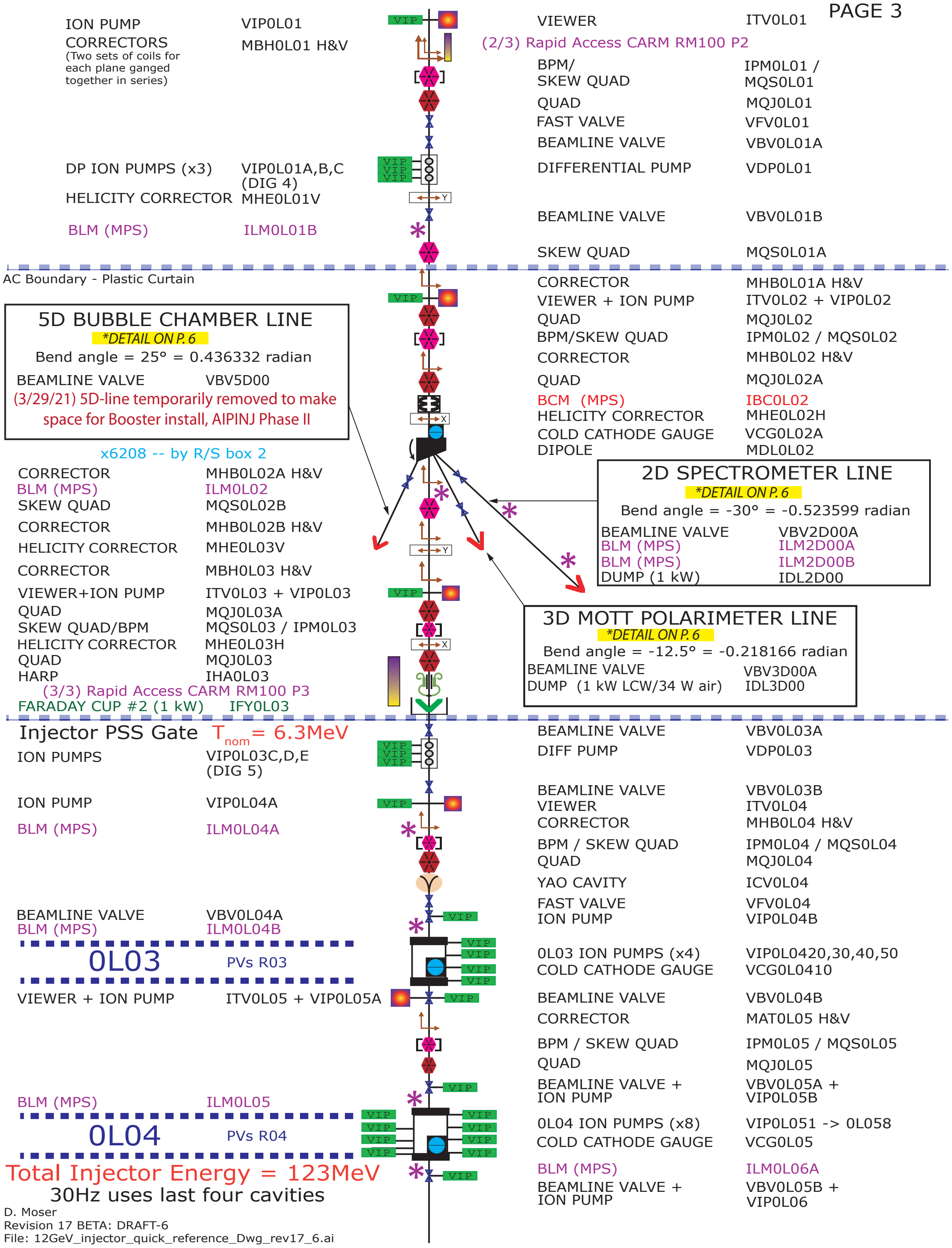

ION PUMP	VIP0L01
CORRECTORS (Two sets of coils for each plane ganged together in series)	MBH0L01 H&V
DP ION PUMPS (x3)	VIP0L01A,B,C (DIG 4)
HELICITY CORRECTOR	MHE0L01V
BLM (MPS)	ILM0L01B

VIEWER	ITV0L01

(2/3) Rapid Access CARM RM100 P2

BPM/ SKEW QUAD	IPM0L01 / MQS0L01
QUAD	MQJ0L01
FAST VALVE	VFV0L01
BEAMLINE VALVE	VBV0L01A
DIFFERENTIAL PUMP	VDP0L01
BEAMLINE VALVE	VBV0L01B
SKEW QUAD	MQS0L01A

AC Boundary - Plastic Curtain

CORRECTOR	MHB0L01A H&V
VIEWER + ION PUMP	ITV0L02 + VIP0L02
QUAD	MQJ0L02
BPM/SKEW QUAD	IPM0L02 / MQS0L02
CORRECTOR	MHB0L02 H&V
QUAD	MQJ0L02A
BCM (MPS)	IBC0L02
HELICITY CORRECTOR	MHE0L02H
COLD CATHODE GAUGE	VCG0L02A
DIPOLE	MDL0L02

5D BUBBLE CHAMBER LINE

**DETAIL ON P. 6*

Bend angle = 25° = 0.436332 radian

BEAMLINE VALVE	VBV5D00

(3/29/21) 5D-line temporarily removed to make space for Booster install, AIPINJ Phase II

2D SPECTROMETER LINE

**DETAIL ON P. 6*

Bend angle = -30° = -0.523599 radian

BEAMLINE VALVE	VBV2D00A
BLM (MPS)	ILM2D00A
BLM (MPS)	ILM2D00B
DUMP (1 kW)	IDL2D00

x6208 -- by R/S box 2

CORRECTOR	MHB0L02A H&V
BLM (MPS)	ILM0L02
SKEW QUAD	MQS0L02B
CORRECTOR	MHB0L02B H&V
HELICITY CORRECTOR	MHE0L03V
CORRECTOR	MBH0L03 H&V
VIEWER+ION PUMP	ITV0L03 + VIP0L03
QUAD	MQJ0L03A
SKEW QUAD/BPM	MQS0L03 / IPM0L03
HELICITY CORRECTOR	MHE0L03H
QUAD	MQJ0L03
HARP	IHA0L03

(3/3) Rapid Access CARM RM100 P3

FARADAY CUP #2 (1 kW)	IFY0L03

3D MOTT POLARIMETER LINE

**DETAIL ON P. 6*

Bend angle = -12.5° = -0.218166 radian

BEAMLINE VALVE	VBV3D00A
DUMP (1 kW LCW/34 W air)	IDL3D00

Injector PSS Gate $T_{nom} = 6.3\text{MeV}$

ION PUMPS	VIP0L03C,D,E (DIG 5)
ION PUMP	VIP0L04A
BLM (MPS)	ILM0L04A
BEAMLINE VALVE	VBV0L04A
BLM (MPS)	ILM0L04B

0L03 PVs R03

VIEWER + ION PUMP	ITV0L05 + VIP0L05A
BLM (MPS)	ILM0L05

0L04 PVs R04

BEAMLINE VALVE	VBV0L03A
DIFF PUMP	VDP0L03
BEAMLINE VALVE	VBV0L03B
VIEWER	ITV0L04
CORRECTOR	MHB0L04 H&V
BPM / SKEW QUAD	IPM0L04 / MQS0L04
QUAD	MQJ0L04
YAO CAVITY	ICV0L04
FAST VALVE	VFV0L04
ION PUMP	VIP0L04B
0L03 ION PUMPS (x4)	VIP0L0420,30,40,50
COLD CATHODE GAUGE	VCG0L0410
BEAMLINE VALVE	VBV0L04B
CORRECTOR	MAT0L05 H&V
BPM / SKEW QUAD	IPM0L05 / MQS0L05
QUAD	MQJ0L05
BEAMLINE VALVE + ION PUMP	VBV0L05A + VIP0L05B
0L04 ION PUMPS (x8)	VIP0L051 -> 0L058
COLD CATHODE GAUGE	VCG0L05
BLM (MPS)	ILM0L06A
BEAMLINE VALVE + ION PUMP	VBV0L05B + VIP0L06

Total Injector Energy = 123MeV

30Hz uses last four cavities

D. Moser
Revision 17 BETA: DRAFT-6
File: 12GeV_injector_quick_reference_Dwg_rev17_6.ai

PAGE 4

ARC 10
*Incomplete on this diagram

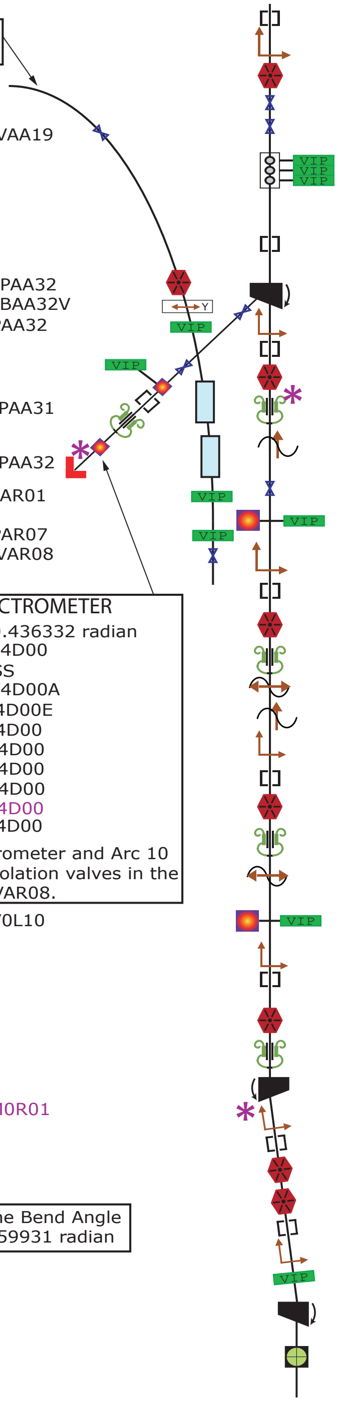

BEAMLINE VALVE	VBVAA19
QUAD	MQPAA32
CORRECTOR	MDBAA32V
ION PUMP	VIPAA32
DIPOLE	MXPAA31
DIPOLE	MXPAA32
ION PUMP	VIPAR01
ION PUMP	VIPAR07
BEAMLINE VALVE	VBVAR08
VIEWER	ITV0L10
BLM (MPS)	ILM0R01

4D (123 MeV) SPECTROMETER

Bend angle = 25° = 0.436332 radian

BEAMLINE VALVE	VBV4D00
ARC 10 CROSS	
BEAMLINE VALVE	VBV4D00A
ION PUMP	VIP4D00E
VIEWER	ITV4D00
BPM	IPM4D00
HARP	IHA4D00
VIEWER	IOR4D00
BLM	ILM4D00
DUMP (17 kW)	IDL4D00

* Note that the 4D Spectrometer and Arc 10 share vacuum. Closest isolation valves in the arc are VBVAA19 and VBVAR08.

BPM	IPM0L06
CORRECTORS	MDB0L06H & MDJ0L06V
QUAD	MQD0L06
FAST VALVE	VFV0L06
BEAMLINE VALVE	VBV0L06A
DIFF PUMP + ION PUMPS (x3)	VDP0L06 + VIP0L06B,C,D
BPM	IPM0L06A
DIPOLE	MBF0L06 “SPECTROMETER”
CORRECTORS	MDB0L07H & MDJ0L07V
BPM	IPM0L07
QUAD	MQB0L07
BLM (MPS)	ILM0L08
HARP	IHA0L07
30Hz CORRECTOR	MAT0L07V (MHF)
BEAMLINE VALVE	VBV0L08
VIEWER + ION PUMP	ITV0L08 + VIP0L08
CORRECTORS	MDB0L08H & MDJ0L08V
BPM	IPM0L08
QUAD	MQB0L08
HARP	IHA0L08
30Hz CORRECTOR	MAT0L08H (MHF)
30Hz CORRECTOR	MAT0L08V (MHF)
CORRECTORS	MDB0L09H & MDJ0L09V
BPM	IPM0L09
QUAD	MQB0L09
HARP	IHA0L09B
30Hz CORRECTOR	MAT0L09H (MHF)
ION PUMP	VIP0L10
CORRECTORS	MDB0L10H & MDJ0L10V
BPM	IPM0L10
QUAD	MQB0L10
HARP	IHA0L10
CHICANE DIPOLE	MBL0R01
CORRECTOR	MAT0R01 H&V
BPM	IPM0R01
QUAD	MQD0R01
QUAD	MQD0R02
BPM	IPM0R02
CORRECTOR	MAT0R02 H&V
ION PUMP	VIP0R02
CHICANE DIPOLE	MBL0R02
SLM	ISR0R02

Injector Chicane Bend Angle
-5.5° = -0.0959931 radian

D. Moser
Revision 17 BETA: DRAFT-6
File: 12GeV_injector_quick_reference_Dwg_rev17_6.ai

PAGE 5

WEST RECOMBINER / NORTH LINAC
*Incomplete on this diagram

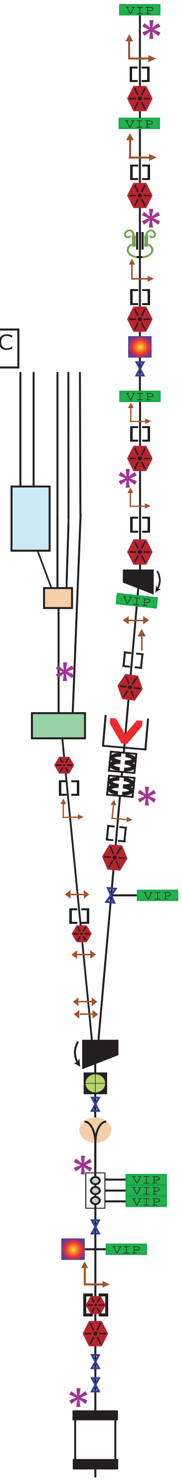

ION PUMP	VIP0R02A
BLM (MPS)	ILM0R03
CORRECTOR	MAT0R03 H&V
BPM	IPM0R03
QUAD	MQD0R03
ION PUMP	VIP0R04
CORRECTOR	MAT0R04 H&V
BPM	IPM0R04
QUAD	MQD0R04
BLM (MPS)	ILM0R04
HARP	IHA0R05
CORRECTOR	MAT0R05 H&V
BPM	IPM0R05
QUAD	MQD0R05
VIEWER	ITV0R05
ROUGHING VALVE	VRV0R05
ION PUMP	VIP0R06
CORRECTOR	MAT0R06 H&V
BPM	IPM0R06
QUAD	MQD0R06
BLM (MPS, lead shielded)	ILM0R06
CORRECTOR	MAT0R07 H&V
BPM	IPM0R07
QUAD	MQD0R07
CHICANE DIPOLE	MBL0R03
ION PUMP	VIP0R08
CORRECTOR	MAT0R08H
CORRECTOR	MBT0R08V
BPM	IPM0R08
QUAD	MQD0R08
INSERTABLE DUMP (17 kW)	IDL0R08
BCM (PSS)	SBC0R08
BCM (MPS)	IBC0R08
BLM (MPS)	ILM0R09
CORRECTOR	MAT0R09 H&V
BPM	IPM0R09
QUAD	MQD0R09
BEAMLINE VALVE + ION PUMP	VBV0R09 + VIP0R09
CHICANE DIPOLE	MBL0R04
SLM (UNPOWERED)	ISR0R09
BEAMLINE VALVE	VBV1L00A
YAO CAVITY	ICV1L01
BLM (Diagnostic)	ILM1L01
ION PUMPS	VIP1L01A,B,C
BEAMLINE VALVE	VBV1L01
ION PUMP	VIP1L02
CORRECTOR	MAT1L02 H&V
BPM / SKEW QUAD	IPM1L02 / MQS1L02
QUAD	MQD1L02
FAST VALVE	VFV1L02
BEAMLINE VALVE	VBV1L02A

DIPOLE	MZAAR03
DIPOLE	MXT4R05
BLM (MPS)	ILM0R08
DIPOLE	MXR2R06
QUAD	MQN1L00
BPM	IPM1L00
CORRECTOR	MBT1L00 H&V
CORRECTOR	MBT1L01H
BPM	IPM1L01
QUAD	MQN1L01
CORRECTOR	MCB1L01H
CORRECTOR	MCB1L01AH
CORRECTOR	MCA1L01H
DIFF. PUMPING STATION	VDP1L01
VIEWER	ITV1L02
BLM (MPS)	ILM1L02

1L02 PVs R12

D. Moser
Revision 17 BETA: DRAFT-6
File: 12GeV_injector_quick_reference_Dwg_rev17_6.ai

0L02 Injector Diagnostic and Experimental Spurs Detail

$T_{nom} = 6.3\text{MeV}$

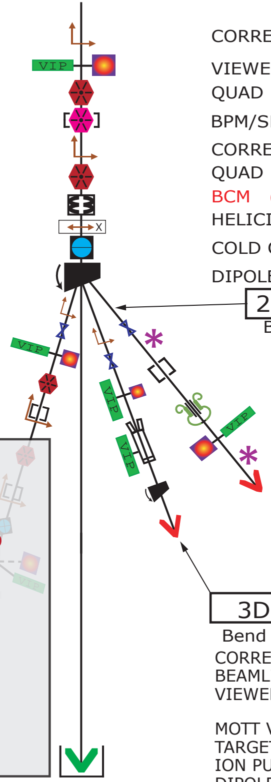

CORRECTOR	MHB0L01A H&V
VIEWER + ION PUMP	ITV0L02 + VIP0L02
QUAD	MQJ0L02
BPM/SKEW QUAD	IPM0L02 / MQS0L02
CORRECTOR	MHB0L02 H&V
QUAD	MQJ0L02A
BCM (MPS)	IBC0L02M
HELICITY CORRECTOR	MHE0L02H
COLD CATHODE GAUGE	VCG0L02A
DIPOLE	MDL0L02

x6208 -- by R/S box 2

5D BUBBLE CHAMBER LINE

Bend angle = 25° = 0.436332 radian

CORRECTOR	MBH5D00 H&V
BEAMLINE VALVE	VBV5D00
ION PUMP + VIEWER	VIP5D00 (DIG 8) + ITV5D00
QUAD	MQD5D00
CORRECTOR / BPM	MBH5D00A H&V / IPM5D00
QUAD	MQD5D01
CORRECTOR / BPM	MBH5D01 H&V / IPM5D01
VACUUM COLD GAUGE	VCG5D01
FARADAY CUP + VIEWER + ION PUMP	IFY5D01 + ITV5D01 + VIP5D01 (DIG 8)
ELECTRON DUMP (1 kW LCW)	IDL5D01
PHOTON COLLIMATOR	IPC5D01
BUBBLE CHAMBER	ITG5D01
PHOTON DUMP	IDL5D01A

5D-line temporarily removed to make space for Booster install, AIPINJ Phase II (3/29/21)

2D 5 MeV SPECTROMETER LINE

Bend angle = -30° = -0.523599 radian

BEAMLINE VALVE	VBV2D00A
BLM (MPS)	ILM2D00A
BPM	IPM2D00
HARP	IHA2D00
ION PUMP	VIP2D00A
VIEWER	ITV2D00
BLM (MPS)	ILM2D00B
DUMP (1 kW)	IDL2D00

3D MOTT POLARIMETER LINE

Bend angle = -12.5° = -0.218166 radian

CORRECTOR	MAD3D00 H&V
BEAMLINE VALVE	VBV3D00A
VIEWER+ION PUMP	ITV3D00 + VIP3D00A (DIG 12)
MOTT VIEWER	IFL3D00
TARGET LADDER	ITG3D00
ION PUMP	VIP3D00B (DIG 12)
DIPOLE	MDT3D01
DUMP (1 kW LCW/34 W air)	IDL3D00

IFY0L03
FARADAY CUP 2 (1 kW)

D. Moser
Revision 17 BETA: DRAFT-6
File: 12GeV_injector_quickreference_Dwg_rev17_6.ai

VITA

Sunil Pokharel
Department of Physics
Old Dominion University
Norfolk, VA 23529

Education

- Ph.D. (Physics), Old Dominion University, Norfolk, Virginia. Defended on March 29, 2024.
- M.S. (Physics), Old Dominion University, Norfolk, Virginia, May 2020.
- M.S. (Physics), Tribhuvan University, Kathmandu, Nepal, September 2007.

Conference and Workshop

- International Spin Symposium (SPIN 2023), Duke University, NC, USA.
- NAPAC 2022, Albuquerque, NM, USA.
- IPAC 2022, Bangkok, Thailand.

Recent Publications

- **S. Pokharel** *et al.,* CEBAF injector model for K-Long bunch charge at 200 kV, in *Proceedings of 14th International Particle Accelerator Conference (IPAC'23), Venice, Italy* (JACoW, CERN, Geneva, Switzerland, 2023), WEPL054.
- **S. Pokharel**, A. S. Hofler, and G. A. Krafft, Modeling a Nb_3Sn cryounit in GPT at UITF, J. Phys.: Conf. Ser. **2420**, 012054, (2023).
- **S. Pokharel** *et al.,* Bunch Length Measurement at the CEBAF Injector at 130 kV, in *Proceedings of North American Particle Accelerator Conference (NAPAC'22), Albuquerque, NM, USA* (JACoW, CERN, Geneva, Switzerland, 2022), FRXD6.
- **S. Pokharel** *et al.,* CEBAF injector model for K_L beam conditions, in *Proceedings of 13th International Particle Accelerator Conference (IPAC'22), Thailand, Bangkok* (JACoW, CERN, Geneva, Switzerland, 2022), MOPOTK052.

Typeset using LaTeX.